



January 2016

A Study Of Single-Phase Flow Through Irregular Miniature Channel Cross-Sectional Geometry And Porous Media

Daniel Berg

Follow this and additional works at: <https://commons.und.edu/theses>

Recommended Citation

Berg, Daniel, "A Study Of Single-Phase Flow Through Irregular Miniature Channel Cross-Sectional Geometry And Porous Media" (2016). *Theses and Dissertations*. 1874.
<https://commons.und.edu/theses/1874>

This Thesis is brought to you for free and open access by the Theses, Dissertations, and Senior Projects at UND Scholarly Commons. It has been accepted for inclusion in Theses and Dissertations by an authorized administrator of UND Scholarly Commons. For more information, please contact zeinebyousif@library.und.edu.

A STUDY OF SINGLE-PHASE FLOW THROUGH IRREGULAR MINIATURE
CHANNEL CROSS-SECTIONAL GEOMETRY AND POROUS MEDIA

by

Daniel Joseph Berg

Bachelor of Science in Mechanical Engineering, University of North Dakota, 2015

A Thesis

Submitted to the Graduate Faculty

of the

University of North Dakota

in partial fulfillment of the requirements

for the degree of

Master of Science

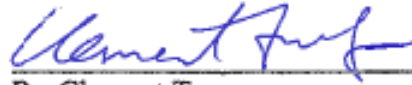
Grand Forks, North Dakota

May

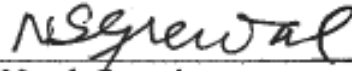
2016

Copyright 2016 Daniel Berg

This thesis, submitted by Daniel Berg in partial fulfillment of the requirements for the Degree of Master of Science from the University of North Dakota, has been read by the Faculty Advisory Committee under whom the work has been done and is hereby approved.



Dr. Clement Tang

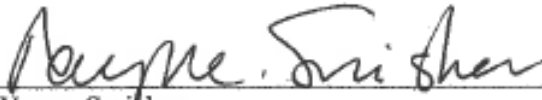


Dr. Nanak Grewal



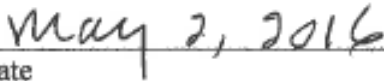
Dr. Surojit Gupta

This thesis is being submitted by the appointed advisory committee as having met all of the requirements of the School of Graduate Studies at the University of North Dakota and is hereby approved.



Wayne Swisher

Dean of the School of Graduate Studies



Date

PERMISSION

Title A Study of Single-Phase Flow Through Irregular Miniature Channel Cross-
Sectional Geometry and Porous Media

Department Mechanical Engineering

Degree Master of Science

In presenting this thesis in partial fulfillment of the requirements for a graduate degree from the University of North Dakota, I agree that the library of this University shall make it freely available for inspection. I further agree that permission for extensive copying for scholarly purposes may be granted by the professor who supervised my thesis work or, in her absence, by the Chairperson of the department or the dean of the School of Graduate Studies. It is understood that any copying or publication or other use of this thesis or part thereof for financial gain shall not be allowed without my written permission. It is also understood that due recognition shall be given to me and to the University of North Dakota in any scholarly use which may be made of any material in my thesis.

Daniel Berg
December 17, 2015

TABLE OF CONTENTS

TABLE OF CONTENTS.....	v
LIST OF FIGURES.....	ix
LIST OF TABLES.....	xiv
ACKNOWLEDGMENTS.....	xv
ABSTRACT.....	xvi
NOMENCLATURE.....	xvii
CHAPTER	
1 INTRODUCTION.....	1
1.1 Intro.....	1
1.2 Objectives.....	2
1.3 Scope of Study.....	3
2 LITERATURE REVIEW.....	4
2.1 Flow in a Horizontal Rectangular Channel.....	4
2.2 Two-Phase Flow Patterns.....	7
2.3 Choi, Yu and Kim Main Results.....	13
2.4 Void Fraction Measurement.....	13
2.5 Fuel Cell Application.....	17

2.6	Two-Phase Flow with T-Junction.....	22
2.7	Branch Angles.....	25
2.8	Branch Angle Main Points.....	30
2.9	Flow Through Porous Media.....	31
2.10	Turbulent Flow Through Porous Media.....	33
2.11	Using Porous Media Approximation to Model Microchannel Heat Sinks.....	35
2.12	Nanofluid Technology Overview.....	36
2.13	Nanofluid Properties.....	36
2.14	Shear-Thickening Nanofluid Applications.....	37
2.15	Nanofluid Heat Transfer.....	43
2.16	Nanofluid Societal Impacts.....	46
3	EXPERIMENTAL SETUP AND METHODOLOGY.....	48
3.1	Overview.....	48
3.2	Syringe Pump.....	49
3.3	Flow Test Sections.....	51
3.4	Porous Media.....	58
3.5	Uniqueness of Porous Media Experiment.....	59
3.6	Microscope.....	60
3.7	Pressure Transducers.....	61
3.8	Pressure Transducer Calibration.....	63
3.9	Data Acquisition.....	64
4	RESULTS AND DISCUSSION.....	67

4.1	Overview.....	67
4.2	Porous Media Testing.....	67
4.3	Porous Media Differential Pressure by Location.....	70
4.4	Form and Viscous Drag.....	72
4.5	Reynolds Number Calculations.....	75
4.6	Determining Dominant Drag.....	78
4.7	Energy and Power Usage.....	81
4.8	Square Non-Porous Channel Expansion and Contraction Flow.....	84
4.9	Expansion Theoretical Differential Pressure.....	84
4.10	Expansion Flow Required Power.....	85
4.11	Total Fluid Moved with 1000 Joules.....	87
4.12	Square Channel Diameter.....	88
4.13	Determining Laminar and Turbulent Flow.....	88
4.14	Contraction Theoretical Differential Pressure.....	90
4.15	Selecting Kc.....	91
4.16	Contraction Theoretical Differential Pressure Modeling.....	93
4.17	Contraction Theoretical Power Modeling.....	98
4.18	Modeling Conclusions.....	101
4.19	Total Volume Moved with 1000 Joules.....	102
4.20	Summary of Expansion and Contraction Testing.....	103
4.21	Hydrodynamic Development.....	103
5	CONCLUSION AND RECOMMENDATIONS.....	106
5.1	Conclusion.....	106

5.2	Recommendations.....	110
	REFERENCES.....	113

LIST OF FIGURES

Figure	Page
1. Experimental setup shown:	5
2. Pressure drop.....	5
3. Shear stresses calculated at the interface	6
4. Experimental setup for the two-phase microchannel flow experiment.	8
5. Rectangular microchannel flow classifications.....	9
6. Gas superficial velocity effect on development of two-phase flow pattern for $AR = 0.92$ at $j_L = 0.20$ m/s.....	10
7. Typical trend of pressure drop in a rectangular microchannel.....	11
8. Void fraction versus volumetric quality	12
9. Effect of void fraction in water on effective relative permittivity for various models	15
10. Capacitance sensor.....	16
11. Phase shift and relative frequency deviation vs.....	17
12. Channel assembly.	19
13. Representative images of two-phase flow structures	20
14. Schematic of the researchers' experimental setup.	20
15. Components of T-junction microchannel for gas-liquid two-phase system at elevated pressure.	23
16. Schematic of the experimental setup for gas-liquid two-phase system at elevated pressure.	23

17. Schematic diagram of the experimental setup	26
18. Time trace of liquid phase before and after the junction for each sub-flow pattern, fraction of gas taken off=0.5.	28
19. Probability of appearance of different sub-flow patterns of slug–annular flow for Cases...29	
20. Captured images of film stop at junctions with different branch angles and the corresponding sketches of secondary flow.	29
21. Plot of sum of B + E should equal 1.	34
22. Dimensionless number E vs Reynolds number.	34
23. Schematic diagram of the microchannel heat sink.	35
24. Temperature distribution of porous media microchannel.	36
25. Shear rate vs. shear stress for shear thickening, Newtonian, and Shear thinning fluids, and Bingham plastic.....	39
26. Logarithmic scale of viscosity vs shear rate for multiple percentage weights of nanosilica.40	
27. Relative absorbed energy vs. shear-thickening fluid concentration.	41
28. Thermal conductivity vs. Temperature of common liquids.....	42
29. Thermal conductivity vs. Temperature of common solids	44
30. Conductivity ratio vs Particle volume fraction of a few selected nanofluids.	46
31. Nexus 3000 syringe pump with optional continuous flow rack and four 140 mL Monojet syringes installed.....	49
32. Claimed vs calculated syringe pump flowrate of +- 1.703828 ml/min and average error of +- 1.17% with an R ² value of 0.9999.	51
33. Image of test expansion and contraction test section.	52
34. Creo Parametric 3D model top view of the expansion and contraction test section.....	52
35. 3D model created with Creo Parametric software	54

36. Base section with porous media inserted into testing slot	55
37. Image of middle test section used in the porous medium testing.	56
38. Image of middle piece created with Creo Parametric software	56
39. Top view of the top piece created with Creo Parametric Software	57
40. Inlet and outlet hole connecting the reservoir to the system tubing.	58
41. SEM micrographs of.....	59
42. Amscope microscope with boom and optional digital camera.	61
43. Honeywell 100 PSIA	62
44. Fluke pressure calibrator used to calibrate the Honeywell PX2 pressure transducers.	64
45. Keysight data acquisition system used in testing.....	65
46. Process flow diagram of the experimental setup.	66
47. Differential pressure vs volumetric flow rate for independent porous test run #1	68
48. Differential pressure vs volumetric flow rate for independent porous test run #2.	68
49. Reservoir differential pressure vs volumetric flow rate using ΔP from runs one and two averaged and plotted with best-fit line.....	69
50. Test run #1 of local differential pressure vs position from the inlet reservoir showing repeatability and non-linear DP growth.....	71
51. Test run #2 of local differential pressure vs position from the inlet reservoir showing repeatability and non-linear DP growth.....	71
52. Chart showing usage of HDD model to determine K and C coefficients using: $\Delta P/L = (\mu/K)*U + C*\rho*U^2$	73
53. First independent data set showing differential pressure/length vs velocity to determine permeability and form coefficients using $\Delta P/L = (\mu/K)*U + C*\rho*U^2$	74
54. Second independent data set showing differential pressure/length vs velocity to determine permeability and form coefficients using $\Delta P/L = (\mu/K)*U + C*\rho*U^2$	74

55. Best-fit line created using two independent sets of data for finding permeability and form coefficients using $\Delta P/L = (\mu/K)*U + C*\rho*U^2$	75
56. Reynolds number based on permeability vs volumetric flow rate using $Re_k = U \rho K^{0.5}/\mu$... 77	77
57. λ vs velocity with averaged trend line from all data points of first and second runs using $\lambda = (\rho*C_0*K_0/\mu_0)*U$	79
58. Viscous and form drag contributions vs lambda.....	80
59. Power required vs volumetric flow rate through titanium dioxide porous media using Power	82
60. Volume of water in ml pumped with 1000 Joules vs flow rate	83
61. 4/1 area ratio rapid expansion theoretical trend line using $\Delta P_e = (A_1/A_2)*(1 - (A_1/A_2))*\rho*V^2$ and experimental data for differential pressure vs volumetric flow rate.	85
62. Expansion power required.	86
63. Total Liters of water moved with 1000 Joules of energy through a 4/1 area ratio rapid expansion using Energy = (P)*(t) vs volumetric flow rate.	87
64. Reynolds number using $Re = \rho*V*D/\mu$ vs volumetric flow rate for the large area of the expansion channel.	89
65. Reynolds number using $Re = \rho*V*D/\mu$ Volumetric flow rate for the smaller square cross sectional area expansion channel	90
66. Chart showing correction coefficients.	91
67. 1/4 area ratio contraction Reynolds number using $Re = \rho*V*D/\mu$ vs volumetric flow rate for the small area of the channel.	92
68. 1/4 area ratio contraction Reynolds number using $Re = \rho*V*D/\mu$ vs volumetric flow rate for the large area of the channel.	93
69. Contraction theoretical differential pressure using large area velocity, turbulent $K_c=0.4$ assumption, and $\Delta P_c = (0.5\rho V^2/g_c)[(1-\sigma^2)+K_c]$ vs volumetric flow rate plotted with experimental data	94

70. Contraction theoretical differential pressure using large area velocity, laminar $K_c=0.78$ assumption, and $\Delta P_c = (0.5\rho V^2/g_c)[(1-\sigma^2)+K_c]$ vs volumetric flow rate plotted with experimental data.....	95
71. Contraction theoretical differential pressure using small area velocity, turbulent $K_c=0.4$ assumption, and $\Delta P_c = (0.5\rho V^2/g_c)[(1-\sigma^2)+K_c]$ vs volumetric flow rate plotted with experimental data.....	96
72. Contraction theoretical differential pressure using small area velocity, laminar $K_c=0.78$ assumption, and $\Delta P_c = (0.5\rho V^2/g_c)[(1-\sigma^2)+K_c]$ vs volumetric flow rate plotted with experimental data.....	97
73. Contraction theoretical power required 1.....	98
74. Contraction theoretical power required 2.....	99
75. Contraction theoretical power required 3.....	100
76. Contraction theoretical power required 4.....	101
77. Liters pumped with 1000 Joules through the contraction channel using: Energy = $P*t$, $\Delta P_c = (0.5\rho V^2/g_c)[(1-\sigma^2)+K_c]$, and $\delta E/\delta t = \text{Volumetric flow rate}*\Delta P$ vs volumetric flow rate (ml/min).	102
78. Hydrodynamic development of flow through a channel.....	104

LIST OF TABLES

Table		Page
1	Gas and liquid superficial velocities and the corresponding flow patterns.....	27
2	Performance Specifications for the Honeywell PX2 pressure transducer.....	63

ACKNOWLEDGMENTS

I wish to express my sincere appreciation to Dr. Clement Tang, my advisor, for his guidance and support throughout the Master's program. I would also like to express my gratitude to Dr. Nanak Grewal and Dr. Surojit Gupta, my advisory committee members, for helping me through the graduate process. I would be remiss not to mention the tremendous financial support from NASA ND Space Grant Consortium, NASA ND EPSCoR, Edson and Margaret Larson Foundation, and The University of North Dakota Mechanical Engineering Department. Without their generous financial contributions, this project would not have been a success. I am also grateful for the help of Jay Evenstad, Gary Dubuque, and Che-Hao Yang for their support at various stages of the research. Finally, I would like to thank my family and fiancé for the encouragement and support. Go Fighting Sioux!

ABSTRACT

The following thesis discusses the in-depth research pertaining to flow through square and rectangular miniature channels with abrupt expansions, contractions, and flow through porous media. Fifty five previously published sources pertaining to the research were closely examined. A closed flow testing loop was designed, constructed, and calibrated to provide the ability to test a wide variety of single and multi-phase Newtonian and non-Newtonian fluids in miniature channels. Over 250,000 data points were collected during the study. Single-phase water flow through 1.59 mm aluminum square channels with abrupt 4 to 1 area ratio expansion and contraction were tested for differential pressure at volumetric flow rates ranging from 1-300 ml/min. Single-phase water flow through 1.59 x 3.18 mm porous media test sections were also tested for differential pressure at volumetric flow rates ranging from 1-300 ml/min. The flow was driven by a highly accurate and precise syringe pump with 10 individual 0-690 kPa Honeywell pressure transducers reading local pressure at key locations along the channels allowing differential pressure to be calculated for multiple locations. Detailed analysis yielded results for a wide variety of parameters including: required power, required energy, form drag, viscous drag, correction factor selection by determining the onset of turbulence using modified Reynolds numbers, and many other critical details for accurately predicting theoretical differential pressure and overall flow behavior through a variety of miniature channels with abrupt changes in channel cross-sectional area.

NOMENCLATURE

A	void fraction
C	form coefficient
c_p	specific heat capacity at constant pressure [J/kg-K]
D_h	hydraulic diameter
E	Energy (J)
f	friction factor
h	heat transfer coefficient [W/m ² -K]
I	current
ID	inner diameter
j_g	gas velocity
j_L	liquid velocity
k	thermal conductivity [W/m-K]
K	permeability coefficient
K_c	contraction correction coefficient
K_e	expansion correction coefficient
\dot{m}	mass flow rate [kg/s] [g/s] xx
mm	millimeters
nf	nanofluid
Nu	Nusselt number
OD	outer diameter
$\delta E/\delta t$	power [W]

P	pressure [N/m ²]
PP	pumping power
q	amount of heat per unit time per unit area [W/m ²]
Q	amount of heat that flows through a body in unit time [W]
r	radius [m]
r ²	correlation strength of data to best-fit line
Re	Reynolds number
Re _k	modified Reynolds number using permeability coefficient
Re _n	Reynolds number for non-Newtonian fluid
R _e	Effective Resistance
T	temperature [K] or [°C]
t	time [s] [min] [hr]
u	velocity of the fluid [m/s]
U _{SG}	superficial gas velocity
U _{SL}	superficial liquid velocity
V	average velocity of fluid
X _{fd,h}	fully developed hydraulic diameter
\dot{V}	volume rate [m ³ /s]
We	Weber number

Greek letter symbols

Δ	designates a difference when used as a prefix
μ	viscosity [kg/m-s] [N-s/m ²]
α	thermal diffusivity [m ² /s]
ϵ_e	effective permittivity

β	volumetric quality
λ	modified porous material Reynolds number
$\dot{\gamma}$	rate of shear strain [1/s]
ρ	density [kg/m ³]
σ	area ratio of expansion or contraction
τ	shear stress [N/m ²]
ν	kinematic viscosity [m ² /s]
\emptyset	particle volume fraction
Φ	Percentage of overall drag caused by viscous effects using: viscous drag / (viscous + form drag) in porous material
Λ	Volume of fluid (m ³)

Subscripts

in	inlet
iw	inside wall
ow	outside wall
nf	nanofluid
out	outlet

CHAPTER 1

1.1 INTRODUCTION

Fluid flow has been studied for centuries, but still has not been completely solved with modern computing and modeling technology. Studying flow in miniature channels with irregular cross-sectional geometry allows further understanding of the complex flow behavior and allows optimization of current and future applications. Flow through porous materials has a number of practical applications including: porous media heat exchangers, pathological blood flow when accumulations of fatty plaques of cholesterol and blood clots increase in the cavity of the coronary artery, fuel cell design and optimization, optimizing space-related miniature flow utilization, and many other applications. Utilizing flow through small passages increases the surface area to volume ratio and increases heat transfer efficiency. Using an experimental setup including: a highly accurate and precise syringe pump, test sections, pressure transducers, thermocouples, data acquisition hardware, and a titanium dioxide porous media sample produced by Dr. Gupta, many conclusions can be made about the flow behavior. Differential pressure and power required to flow the fluid through the test sample are essential to proper design and can be predicted by measuring the permeability and form coefficient of the porous media. Similar predictions can be made modeling rapid contractions and expansions using theoretical predictions derived from Navier-Stokes momentum equations and correction factors from empirical evidence.

1.2 Objectives

This thesis was created to look into several main objectives in areas of interest that have not been sufficiently studied. The first goal was to study the power, differential pressure, and total energy needed to flow single-phase, Newtonian, distilled water through rectangular 4 to 1 area ratio expansions and contractions. Since the flow rates studied range from fully laminar from 0-2300 Reynolds numbers to the onset of turbulence, but not fully turbulent at 2300-3500 Reynolds numbers, a determination should be made if the flow at Reynolds numbers ranging from 2300-3500 should be modeled as laminar or turbulent. Then, the results should be compared to the power and energy needed to flow through channels with titanium dioxide porous material inserted mid-channel. The study also looked to review the effect of volumetric flow rate through porous, expansion, and contraction channels on required power and energy consumption. The study also is intended to discover a way to accurately characterize the flow through the titanium dioxide porous material. To characterize the flow properly, an accurate method of predicting differential pressure is needed. An alternative method of producing Reynolds numbers for porous media is also essential to characterizing flow. The thesis will discuss the best way to produce these values. Since Reynolds numbers depend on the velocity in the channel and a rapid expansion and contraction channel have two different velocities, a determination will be made as to which velocity will provide the most accurate results for calculations involving velocity. Finally, the amount of power produced by the pump will be compared with the amount required to move the water through just the porous material.

1.3 Scope of Study

Due to time and money constraints, the study had to be limited to studying single-phase, Newtonian, distilled water flow through miniature expansion, contraction, and porous media channels at volumetric flow rates ranging from 0-300 ml/min and Reynolds numbers from 0-3500. The channels are part of a circulating flow loop that is assumed to be isothermal due to no heat flux being applied and the differential temperature being monitored at the channel inlet and outlet being negligible. Due to pumping limitations, fully turbulent conditions could not be achieved. Although, from 200-300 ml/min, Reynolds numbers range from 2300-3500 in the smaller channel cross-sectional area, and there is an onset of turbulence in the channel. The study can predict if the flowrates from 200-300 ml/min should be modeled as laminar or turbulent, but cannot make an accurate prediction above 300 ml/min or Reynolds numbers above 3500.

CHAPTER 2

LITERATURE REVIEW

2.1 Flow in a Horizontal Rectangular Channel

Valinčius et al. (2011) conducted a study that centered on understanding how condensation can affect two-phase flow stability by experimentally investigating and modeling two-phase flow. They also considered rapid condensation conditions as a centerpiece of the study. In addition, they looked at previous work on correlations for two-phase flow completed in the twentieth century (Taitel and Dukler, 1976; Kang and Kim, 1993; Brauner and Maron, 1993). They also go into detail discussing uniform void fraction measurements with differential pressure measurements and wall shear stresses (Valincius, et al., 2008). According to Valinčius et al. (2011), “The current task is to identify parameters of interfacial instabilities, which can cause condensation to reinforce itself. Positive feedback mechanism can take place when steam flow starts generating waves at the interface and thus increases the direct contact condensation area.” Valinčius et al. (2011) used an experimental setup with a length of 0.843 meters, height of 0.075 meters for gas phase and 0.025 meters for liquid phase, a width of 0.02 meters and a cross-sectional area of 0.002 meters squared with equivalent hydraulic diameter of 0.033 meters. An illustration can be seen in Figure 1 below explaining the setup

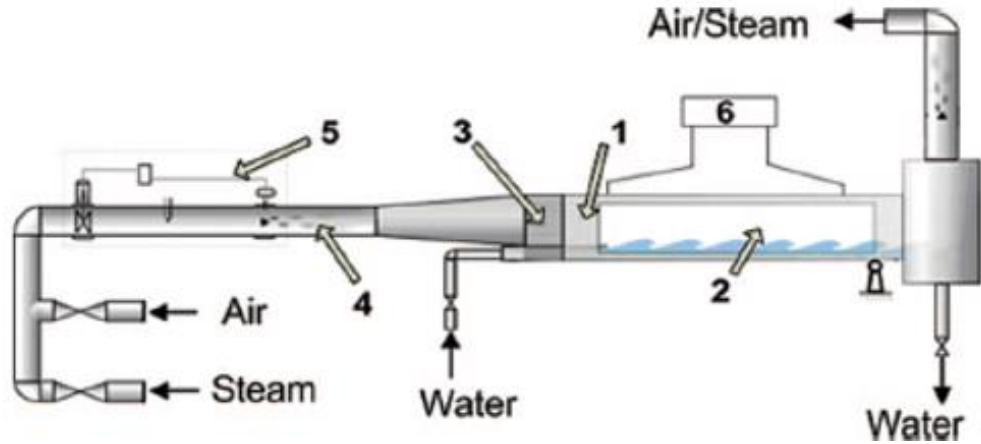


Figure 1: Experimental setup shown: 1—rectangular channel; 2—windows, 3—flow equalizer; 4—inlet pipe; 5—flow control measurement; 6—differential pressure measurement; (Valinčius et al, 2011)

Another interesting parameter measured by Gasiunas and Seporaitis (2008) is pressure drop.

Pressure drop is critical for many measurements in fluid flow and has an impact on power required to flow the fluid through the channel.

The pressure drop measurements based on gas velocity can be seen below in Figure 2.

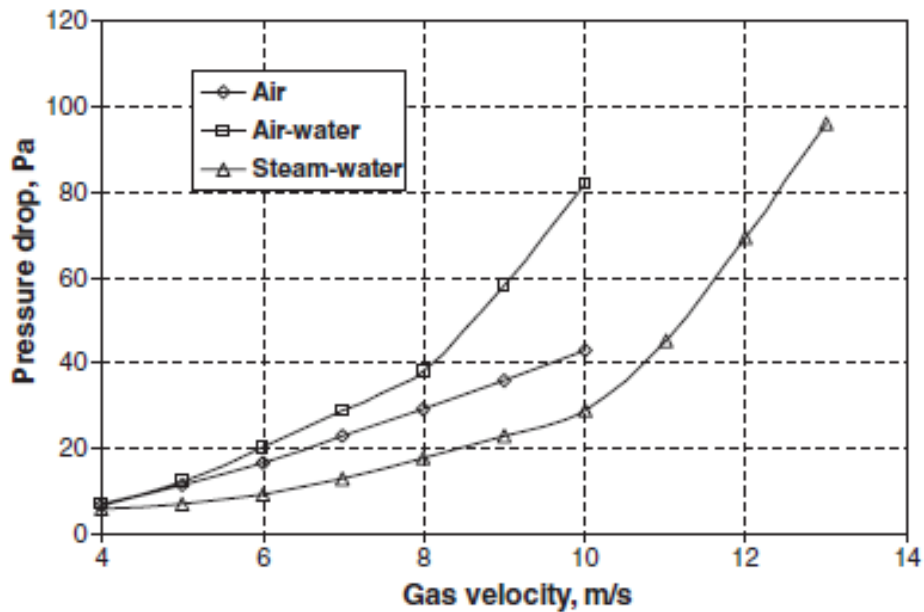


Figure 2: Pressure drop (Pa) vs gas velocity (m/s) (Valinčius et al., 2011)

Valinčius et al. (2011) also found the pressure drop when no condensation occurs is due to the friction at the interface and the wall friction. Below in Figure 3, the shear stresses due to the interface are shown.

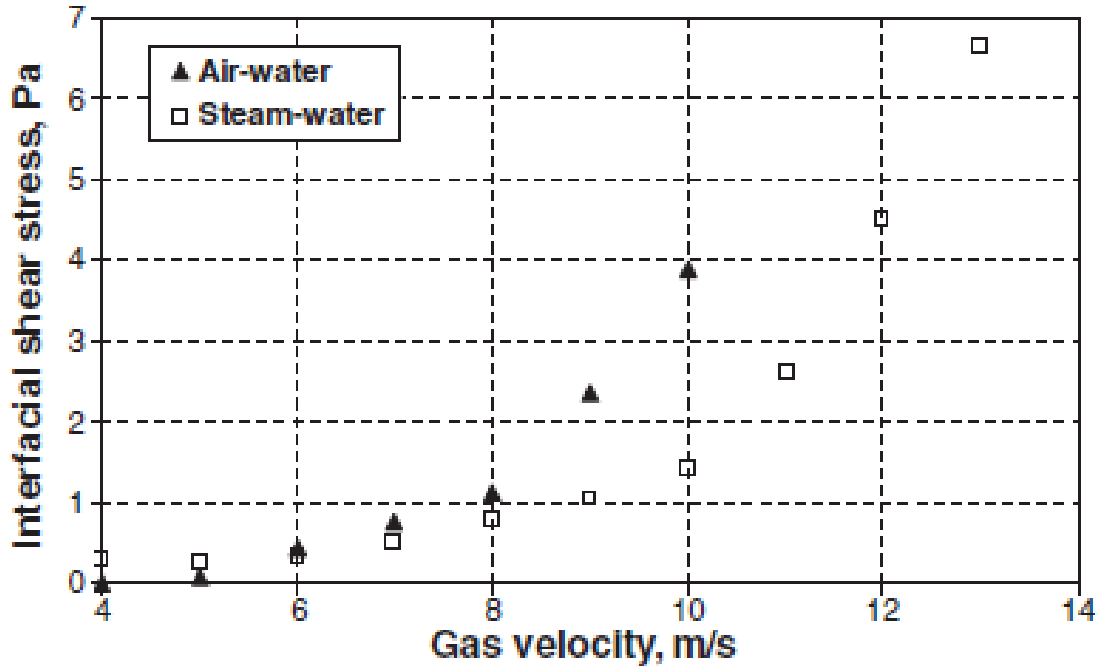


Figure 3: Shear stresses calculated at the interface (Valinčius et al., 2011)

The results from the experiment were very reasonable and seemed accurate for single and multi-phase flow. The authors did run into a bit of trouble trying to model the two-phase flow because they could not maintain a water depth at high velocities. Valinčius et al. (2011) believe “Further work will consider evaluation of interfacial friction in condensable two-phase flow and influence of condensation to interface stability.”

2.2 Two-Phase Flow Patterns

Choi et al. (2011) conducted an interesting research experiment pertaining to two-phase flow that was published in the International Journal of Heat and Mass Flow. A main purpose of the experiment was to study how a parameter known as an aspect ratio affects flow pattern, void fraction, and pressure drop of an experiment (Choi et al., 2011). They used the widths and heights of rectangular microchannels that were $510\ \mu\text{m} \times 470\ \mu\text{m}$, $608\ \mu\text{m} \times 410\ \mu\text{m}$, $501\ \mu\text{m} \times 237\ \mu\text{m}$, and $503\ \mu\text{m} \times 85\ \mu\text{m}$. Therefore, the aspect ratios of the rectangular microchannels were 0.92, 0.67, 0.47 and 0.16; and the hydraulic diameters of the rectangular microchannels were 490, 490, 322 and 143 μm , respectively. Channel size selection can have a large effect on flow characteristics (Chung and Kawaji, 2004; Kawahara et al., 2009). The experimental ranges conducted by Choi et al. (2011) were liquid superficial velocities of 0.06–1.0 m/s and gas superficial velocities of 0.06–71 m/s. They also assert an important parameter of the experiment is the flow type. There can be many different forms of bubbles in two-phase flow (Squires and Quake, 2005; Serizawa et al., 2002). Using a camera to determine what flow is happening in each situation is critical to predicting performance. They found bubble flow was dominant when the aspect ratio was increased. This was due the thickness of the film in the corner was reduced and the confinement was increased due to the reduced volume to surface area ratio (Moriyama and Inoue, 1992). They also found when the aspect ratio is reduced along with liquid film thickness the flow becomes more homogeneous. They also found the pressure drop due to friction in rectangular channels was highly correlated to the flow pattern (Choi et al., 2011). Kandlikar (2002) has many correlations for flow boiling including relating nucleate boiling to heat transfer values. Using the research done by Kandlikar (2002) on miniature and microchannel flow boiling, Choi et al. (2011) were able to add to the scientific knowledge of two

phase flow even though the research was not completely similar to the work done by Kandlikar (2002). Choi et al. (2011) found in microchannel applications, a bubble has a tendency to elongate because the channel is not wide enough for the bubble to take a spherical form and keep the needed volume. They also included some useful diagrams explaining the procedure and equipment used. The experimental equipment and process can be seen in Figure 4 below.

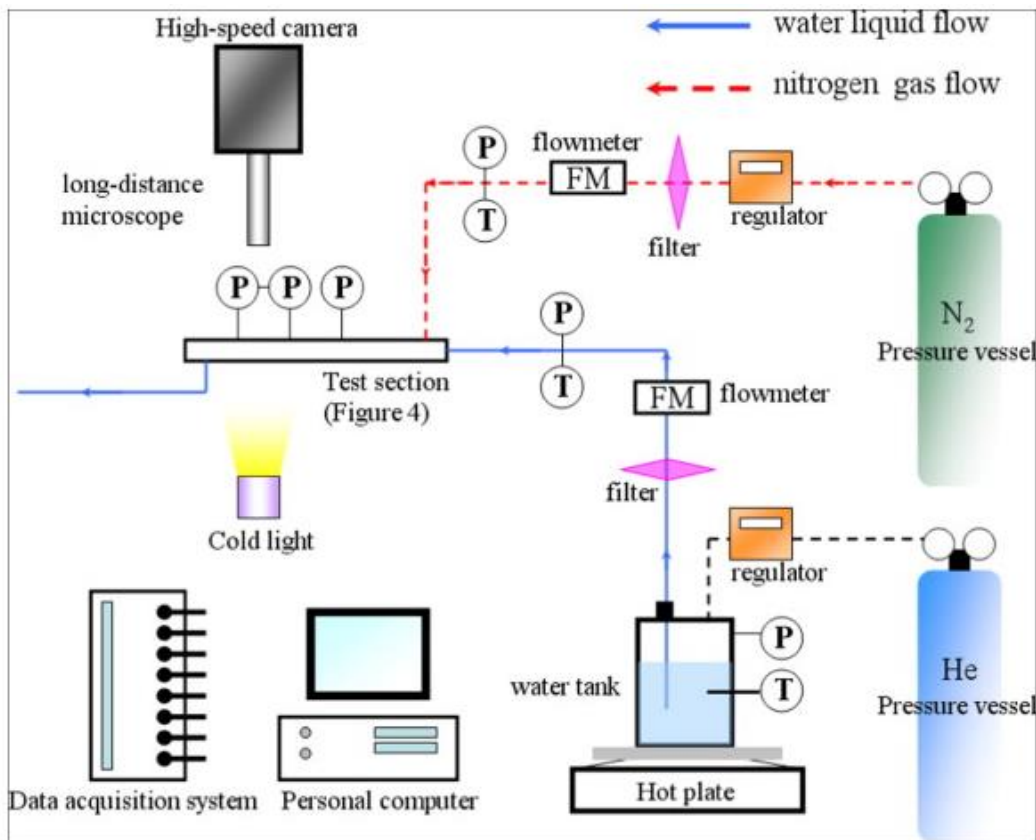


Figure 4: Experimental setup for the two-phase microchannel flow experiment (Choi et al., 2011).

Flow patterns were a key aspect of this experiment (Wong et al., 1995). The flow classifications determined by Choi et al. (2011) can be seen below in Figure 5.

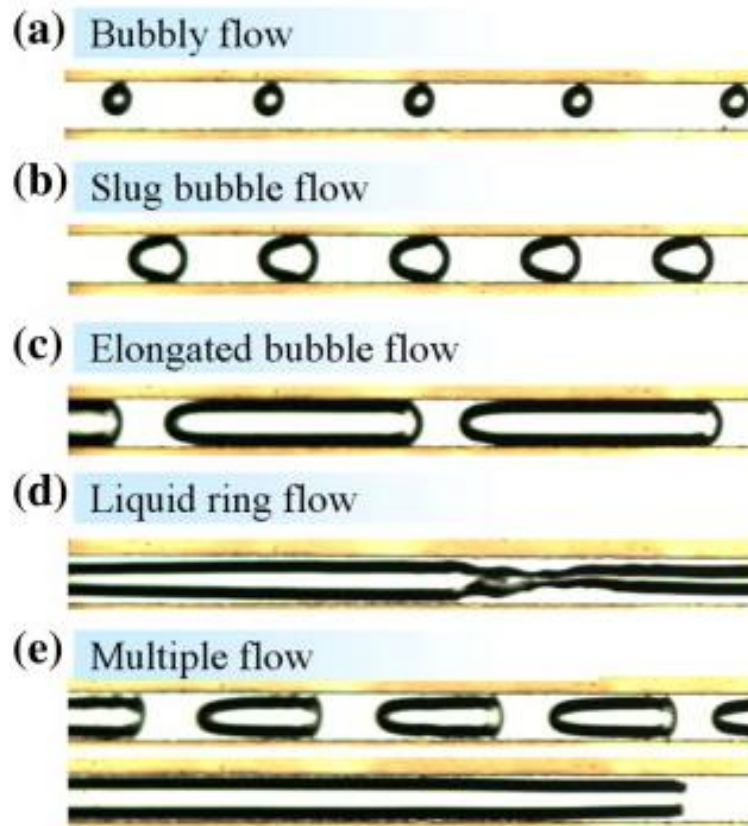


Figure 5: Rectangular microchannel flow classifications (Choi et al., 2011).

Choi et al. (2011) looked at increasing the gas velocity while maintaining the liquid velocity and determining the effects on the flow pattern. In Figure 6, J_G is the gas superficial velocity and J_L is the liquid superficial velocity. They found when the J_G reached 1 m/s, there was a transition from elongated bubble toward liquid ring (Choi et al., 2011). It was not a full transition, just a midpoint between the two classifications.

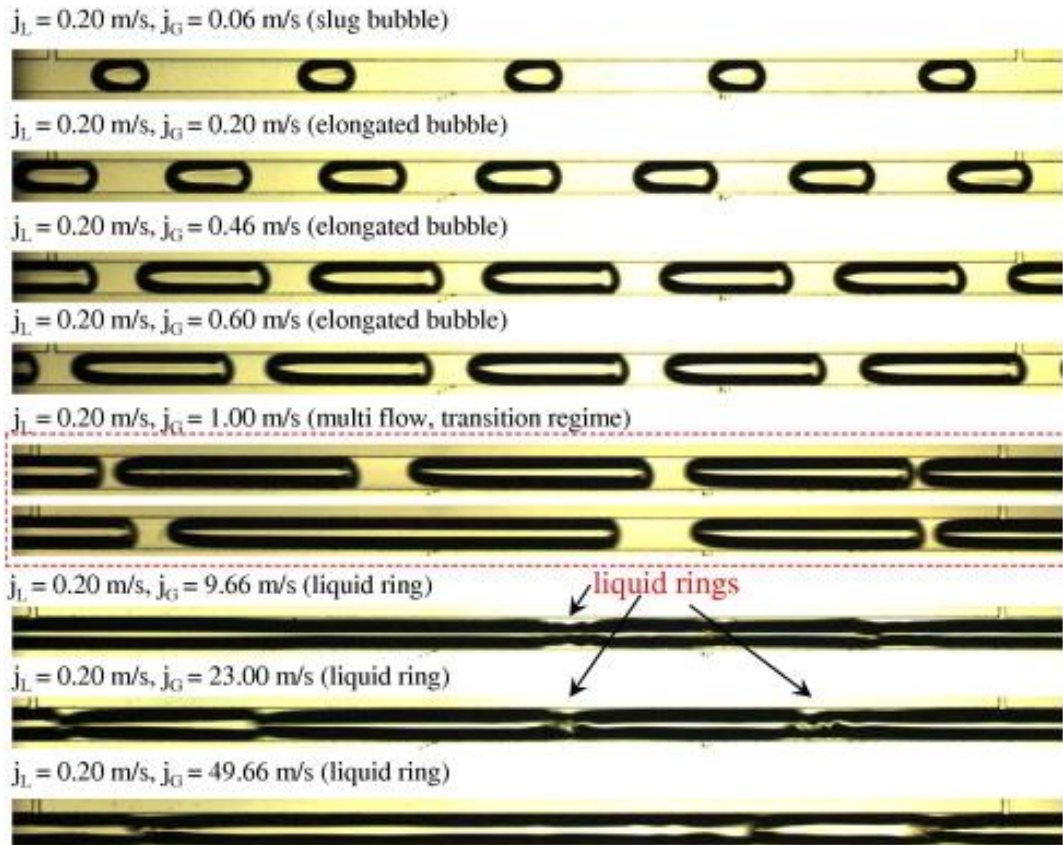


Figure 6: Gas superficial velocity effect on development of two-phase flow pattern for $AR = 0.92$ at $j_L = 0.20$ m/s (0.06 m/s $< j_G < 49.66$ m/s) (Choi et al., 2011).

The researchers also found similar results as Valinčius et al. (2011) when determining the liquid film thickness. The results showed the liquid film thickness decreased when the aspect ratio was increased (Choi et al., 2011). Pressure drop was also considered in the experiment and is an essential part of understanding multiphase flow. Important aspects from this experiment were discovered because of research done by predecessors over six decades ago as well as a few years ago. This exemplifies the fact that research is an ongoing process and can prove to be valuable for many decades in the future (Lockhart and Martinelli, 1949; Agostini et al., 2008). The bubbly, elongated bubble, and liquid slug areas were considered in the experiment and the results can be seen in Figure 7.

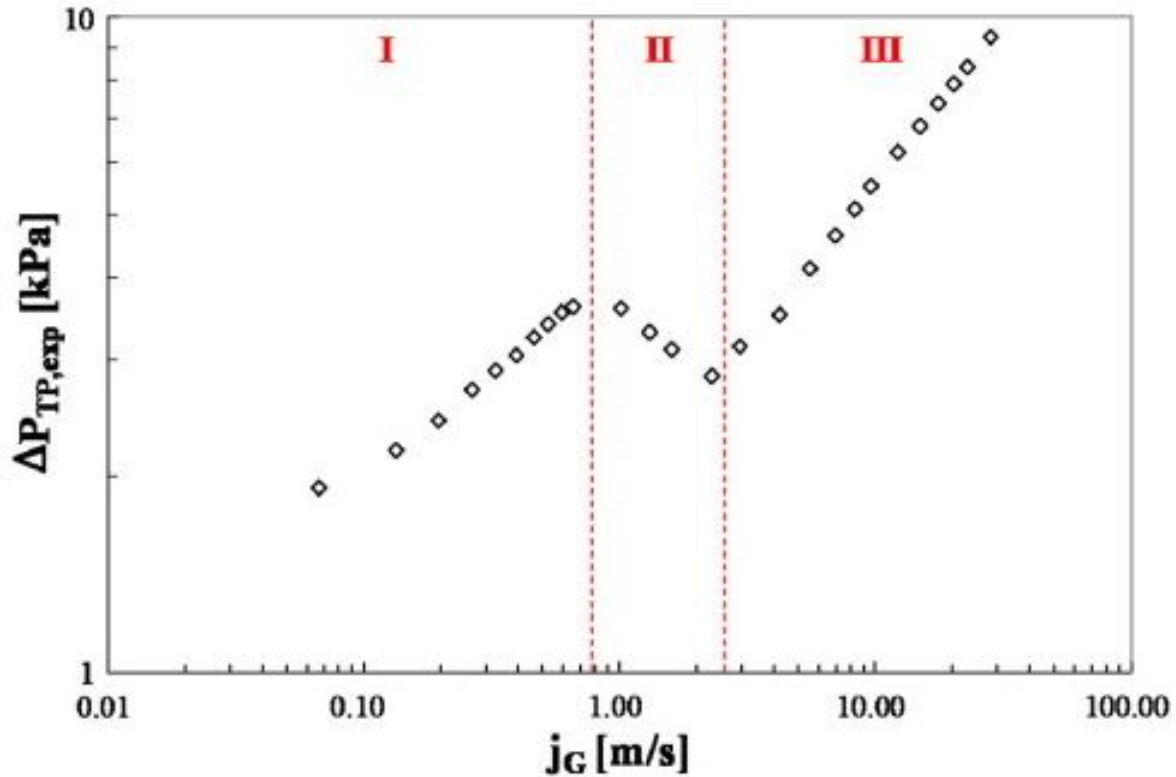


Figure 7: Typical trend of pressure drop in a rectangular microchannel: (I) bubbly, liquid slug and elongated bubble flow regimes, (II) multiple flow regime (transition regime) and (III) liquid ring flow regime (Choi et al, 2011)

This experiment also covered void fraction calculations for rectangular microchannel flow which has been shown to be of high importance (Triplett et al., 1999). They used a simple equation stating void fraction is equal to gas superficial velocity divided by bubble velocity (Choi et al., 2011).

$$A = j_G / u_B \quad (2.2.1)$$

Figure 8 below shows a correlation between void fraction and volumetric quality (β). Also included in the image are previous researchers work and how closely the previous data correlates to (Choi et al., 2011).

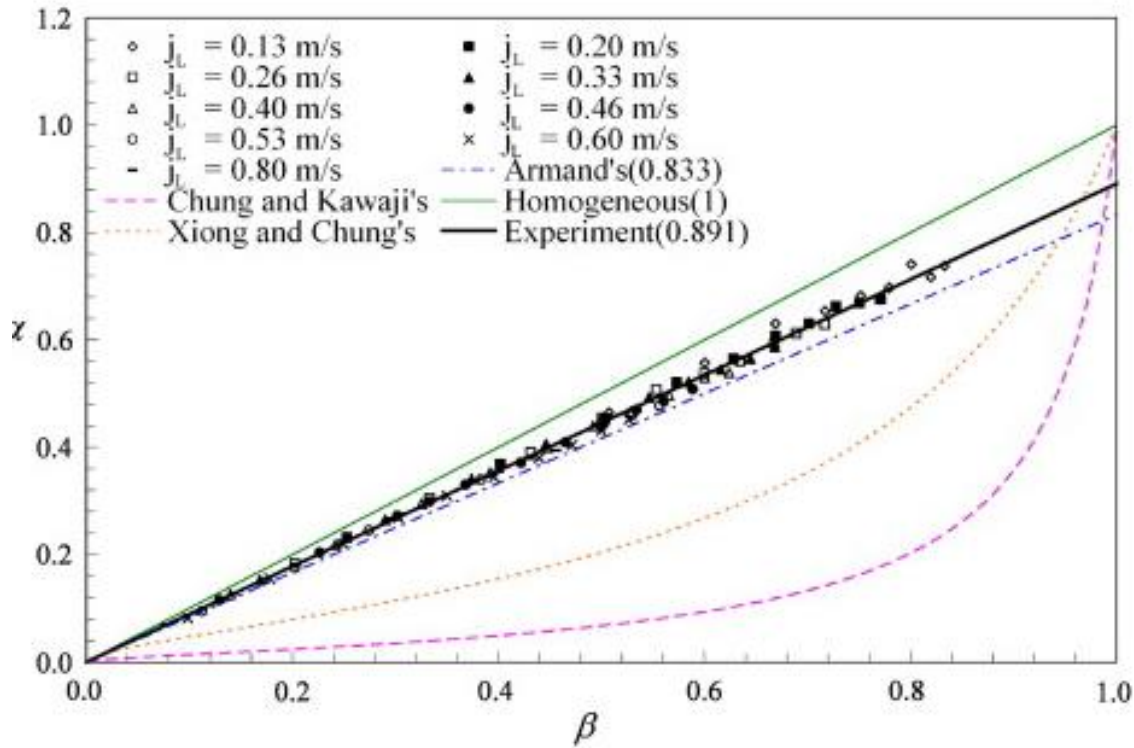


Figure 8: Void fraction versus volumetric quality (Choi et al., 2011)

The researchers also noted the work of Kawaji (2008) who did research into unique properties of two phase flow in adiabatic microchannels. This work was used a valuable resource in providing relatively recent discoveries in the field that were published in a peer-reviewed journal.

Adiabatic flow was also looked at in the early 1990's by Ali et al. (1993) using flow between two parallel plates. This brings a unique perspective because the flow is then between two flat plates instead of a traditional round pipe or channel (Ali et al., 1993). Using the information from these discoveries made over two decades ago assisted Choi et al. (2011) in making experimentation in the 21st century. Mishima et al. (1993) also looked at flow in rectangular ducts, but chose a narrow passage cross-sectional area. This provided unique properties and a

higher contact surface area to passage area ratio. This increased the shear stress per unit volume and allowed a different perspective on fluid flow to be considered.

2.3 Choi, Yu and Kim Main Results

Choi et al. (2011) found a few main results from their research with high speed cameras on transparent rectangular microchannel two-phase flow testing. They found as the aspect ratio decreased, the bubble area was increased and the liquid area was reduced. As the hydraulic diameter decreased, the two-phase interaction also decreased. The dominant parameter in the void fraction calculation is the aspect ratio, not the hydraulic diameter. As the aspect ratio decreases, the flow becomes more homogeneous. Aspect ratio and hydraulic diameter both have an impact on microchannel two-phase flow so independent experiments must be conducted to fully understand the flow (Choi et al., 2011).

2.4 Void Fraction Measurement

Jaworek and Krupa (2010) have looked into the different ways of measuring a void fraction in two-phase flow. Void fraction calculation is a key component of many calculations critical to understanding two-phase flow (Harvel et al., 1996; Wang et al., 2008; Abouelwafa and Kendall, 1980). There have been numerous strategies in past publications on how to determine the void fraction. Jaworek and Krupa (2010) studied the ability of different sensors to measure void fractions in two-phase flow. The capacitance sensor uses two electrodes that essentially are put on the outside of a dielectric pipeline where the two-phase flow to be measured is flowing (Jaworek and Krupa, 2010). As the flow passes through the pipe, the capacitance will change based upon how much gas and liquid is present at that time. It is based solely on a percentage. Studying two-phase flow using capacitance seems to be a common theme among researchers in

the mid 1980's studied the outside versus inside sensors to calculate void fraction (Stott et al., 1985). There was also experimentation a short time later by Huang et al. (1988a) looking into using capacitance measurements using a charge transfer method. Also, Huang et al. (1988b) looked into using a transducer for industrial applications that at the time was new while the same research group wrote a similar paper on studying low capacitance values using transducers (Huang et al., 1988a). Various researchers looked into different ways to utilize capacitance in measuring void fraction from 1998 to 1999 (Tollefsen and Hammer, 1998; Jaworski et al., 1999; Keska and Williams, 1999). This paved the way for the following researchers to investigate further in the 2000's. Many investigators continue research in 2010 to find new ways to measure void fraction and they utilized a phase shift between sinusoidal signal passing the capacitance sensor and reference signal instead of old methods (Jaworek and Krupa, 2004; Jaworek et al., 2004; Caniere et al., 2007; Caniere et al., 2008; Ahmed and Ismail, 2008). The phase shift allowed Jaworek and Krupa (2004) to measure void fraction instead of measuring capacitance. They also wanted to understand how void fraction is correlated with effective permittivity of a medium.

To better understand the correlation between void fraction and effective permittivity, Jaworek and Krupa (2004) included a graph that can be seen in Figure 9. This data clearly shows the best method is parallel capacitances for providing the most accurate void fraction determination.

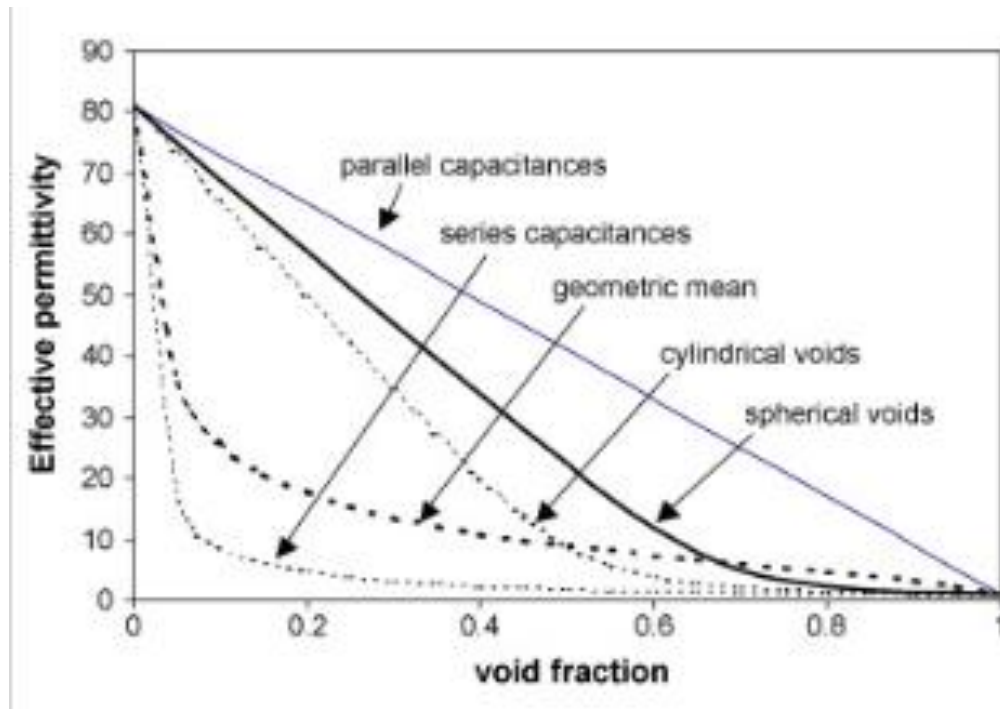


Figure 9: Effect of void fraction in water on effective relative permittivity for various models (Jaworek & Krupa, 2010)

To visualize what is happening in a capacitance measurement to determine void fraction, Figure 10 shows an excellent illustration. Notice the capacitance sensor is on the left, the top right is a cross-sectional view of the pipe, and lower right showing the capacitance circuit.

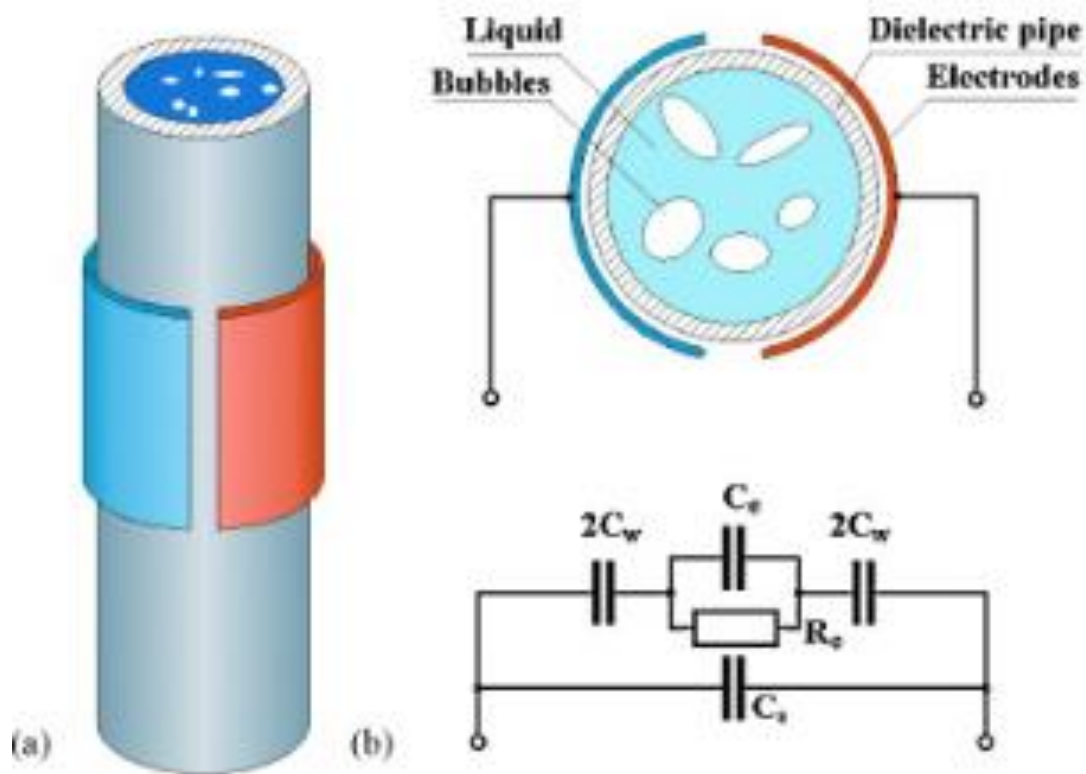


Figure 10: Capacitance sensor. (a) Scheme of the electrodes placed on the dielectric pipe. (b) Equivalent circuit. $2C_w$ is the wall capacitance, C_s is stray capacitance, C_e is an effective capacitance representing the medium within the pipe, R_e is an effective resistance of the medium within the pipe (Jaworek & Krupa, 2010).

Jaworek and Krupa (2010) ultimately determined the void fraction using a phase shift model for two-phase flow. They ran two separate measurements and ultimately were able to calculate the results as shown in Figure 11.

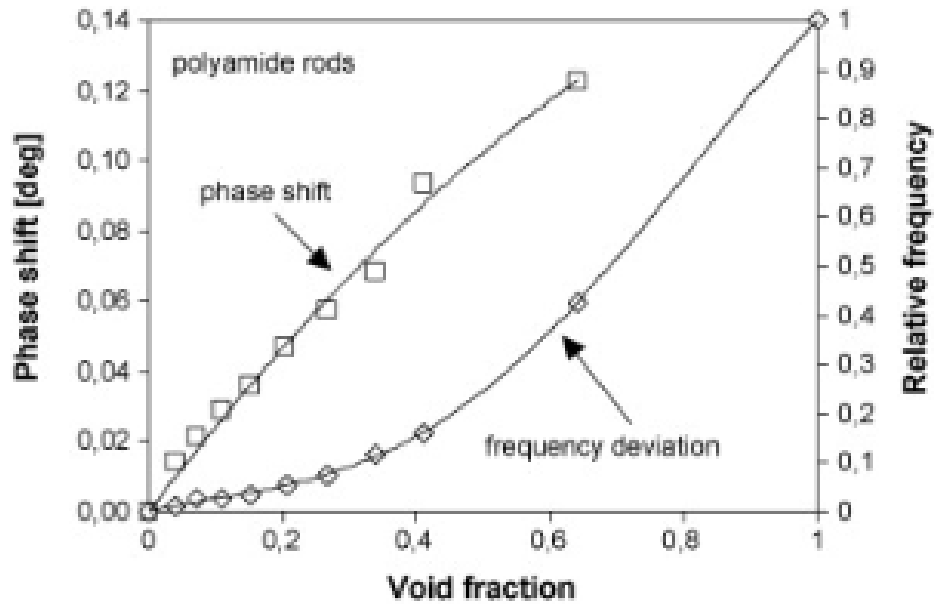


Figure 11: Phase shift and relative frequency deviation vs. void fraction in a vertical pipe of 32 mm I.D. and 40 mm O.D., electrodes length 10 mm. Liquid: distilled water. Voids in annular flow were simulated with polyamide rods of various diameters (Jaworek & Krupa, 2010).

Jaworek and Krupa (2010) found the main conclusions of this article are a model for detecting two-phase void fraction was determined by using a response signal from a capacitance sensor and reference sensor were shown theoretically and experimentally. They found the phase shift was extremely proportional to the phase shift (Jaworek and Krupa, 2010). They also state their method using the response function eliminates many intermediate steps used in other capacitance meters. The paper was published in 2010 and to the authors best knowledge, this was the first time anyone had used detection of phase shift between two signals for measuring void fraction in two-phase flows (Jaworek and Krupa, 2010).

2.5 Fuel Cell Application

Steinbrenner et al. (2011) have done research pertaining to two-phase microchannel flow. They were particularly interested in the effects of this flow on fuel cell applications. Previous studies

done in the 2000's by Li et al. (2007), (Barbir et al. (2005), Cha et al. (2004), and Nguyen and Knobbe (2003) were instrumental in providing a baseline of information on flow in fuel cell microchannels to assist the new research. According to Steinbrenner et al. (2011), "An important function of the gas delivery channels in PEM fuel cells is the evacuation of water at the cathode. The resulting two-phase flow impedes reactant transport and causes parasitic losses. There is a need for research on two-phase flow in channels in which the phase fraction varies along the flow direction as in operating fuel cells." Steinbrenner et al. (2011) decided to study flow that pertained to fuel cells by using a porous CDL wall in channel lengths of 0.6 meters long using a distributed water injection procedure. They also produced low maps using flow rates of local gas and liquids. The researchers also hoped to bridge the gap between the theoretical increased performance of proton exchange membrane fuel cells that utilize micro channels and the real-world underperforming microchannel practical systems. Steinbrenner et al. (2011) state, "While the performance of the membrane depends on ample humidification, liquid water in the microporous layer, gas diffusion layer (GDL), and/or gas delivery channels impedes the flow of reactant gases to catalyst sites and cripples cathodic reaction rates. Two-phase flow phenomena have been identified as concerns for flooding-induced performance degradation, cell voltage hysteresis, increased parasitic pumping losses, and the absence of predicted performance improvements." The researchers believe one of the main reasons for this real-world underperformance is increased flooding in channels of smaller size where surface tension can become a relatively large contributor of force when compared to the pressure, viscous, and inertial forces. They feel the experiment with porous walls and long channel lengths will help them discover characteristics of fuel cells and help them increase their efficiency. Steinbrenner et al. (2011) used a serpentine channel with a square cross channel of 500 micrometers wide and

0.6 meters long to conduct the experiment. It also had four short turns and five long segments (Steinbrenner et al., 2011). The layout can be seen below in Figure 12.

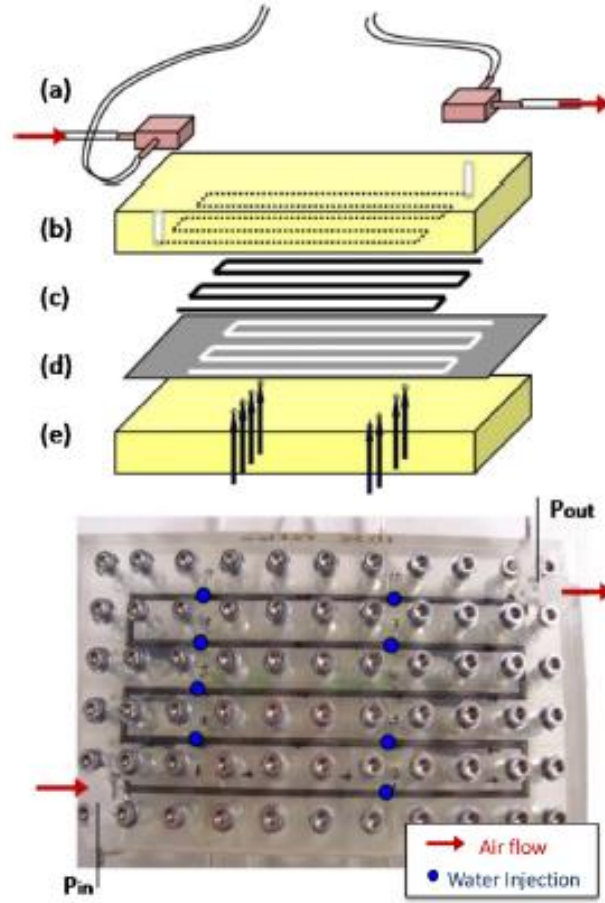


Figure 12: Channel assembly. The following layers are sandwiched together to create a sealed serpentine channel with distributed water injection through the porous GDL layer: (a) connections to air tubing and pressure transducers, (b) 1/4 m cast acrylic with 500 cm×500 cm×60 cm channel, (c) 190 cm thick×2mm wide Toray Carbon Paper GDL (0 or 10 wt% Teflon), (d) latex gasket, (e) 1/4 m thick cast acrylic with 300–500 mm diameter water injection holes (Steinbrenner et al., 2011).

This set up was complimented with a syringe pump pressure measurement device, and flow rate meters. They also used a camera to capture images of the moving flow. The flow can be seen below in representative images of Figure 13.

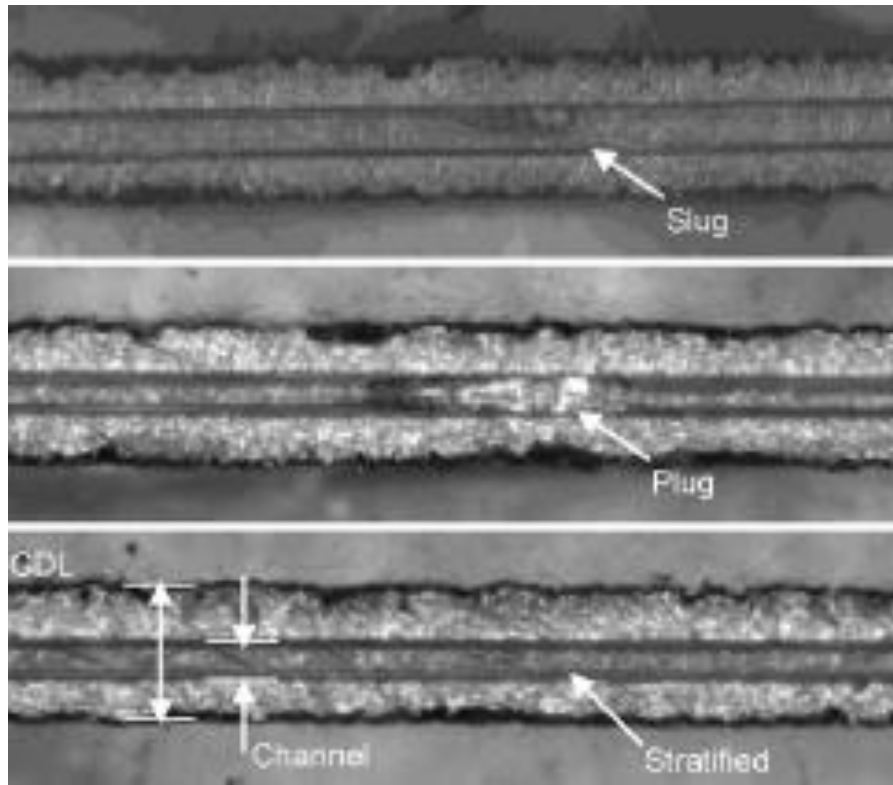


Figure 13: Representative images of two-phase flow structures: (a) slug, (b) plug, and (c) stratified (Steinbrenner et al., 2011).

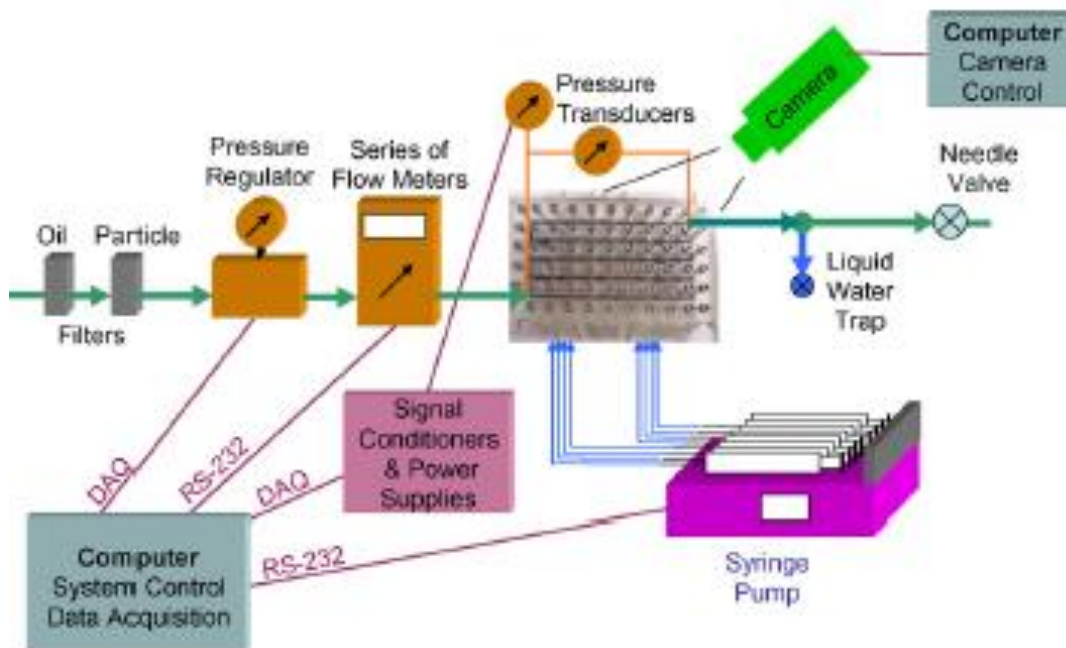


Figure 14: Schematic of the researchers' experimental setup (Steinbrenner et al., 2011).

Steinbrenner et al. (2011) found in the results the channel geometric configuration has a large impact on the local flow conditions. They found the liquid flow portion of the two-phase flow varies based on local conditions and parallel flow channels while the gas flow is proportional to the length of the test channel during the experiment. They also found using parallel channels had a number of effects (Steinbrenner et al., 2011). They found parallel channels negatively affect water expulsion by reducing the overall differential pressure for the system given a set flow rate and also found the water to air flow rate will change much quicker because of the smaller flow length (Steinbrenner et al., 2011). There is another downside to using multiple channels according to the researchers. They found instabilities in the flows of multiple channels because of the small geometric anomalies from inherent variations due to introduction of liquid water droplets. This can cause instability in fuel cell microchannels (Steinbrenner et al., 2011). Using fewer parallel channels can have some positive effects such as higher gas velocity in the channel and allowing for better mass transport and removal of water from the channels, and benefits from a larger differential pressure over the length of the channel (Steinbrenner et al., 2011). The researchers also point out correctly there will usually be more turns in an application with less parallel channels. More turns will cause liquid to accumulate and films to form in the channels Steinbrenner et al. (2011) close their paper by mentioning the results of their research show water evacuation will be reduced with increased corners because of the films that will be created in the corners They also say the increased differential pressure will help remove water from the channels. They hope this research will help provide useful information in creating more efficient proton exchange membrane fuel cells in the future.

2.6 Two-Phase Flow with T-Junction

Zhao et al. (2013) recently did an investigation into the effects on microchannel flow. They specifically studied two-phase flow with a T junction. They used studies from many past researchers including Coleman and Garimella (1999), Cubaud et al. (2006), Kawahara et al. (2002), and Triplett et al. (1999). The studies published from the late 90's to the 2000's provided an essential background for the work done by (Zhao et al., 2013). They used a deionized water and nitrogen combination with the T junction to look for specific flow patterns. They also used a variety of pressures ranging from 0.1 to 5 MPa. This allowed the researchers to analyze the flow using Weber numbers and looked for different varieties of flow patterns. They found the following flow patterns: bubbly flow, slug flow, unstable slug flow, parallel flow, slug-annular flow, annular flow, and churn flow (Zhao et al., 2013). Using a channel with a cross-section of 300 μm by 600 μm and a hydraulic diameter of 400 μm (Zhao et al., 2013) were able to perform various tests and confirm the test section was gas-tight and ready for applications up to 7 MPa. The test section can be seen in Figure 15.

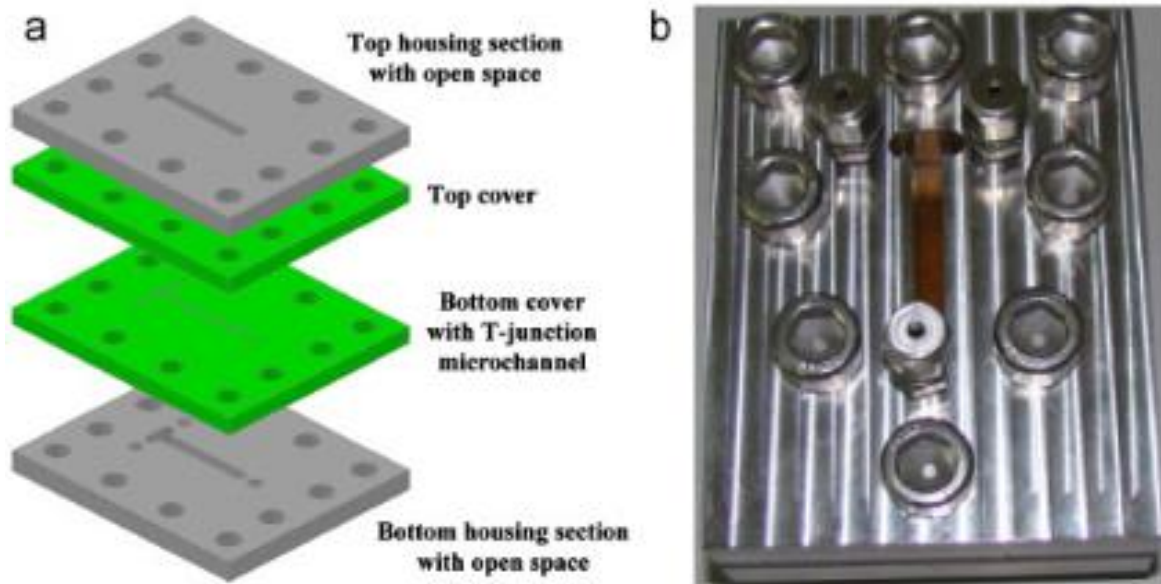


Figure 15: Components of T-junction microchannel for gas–liquid two-phase system at elevated pressure. (a) Construction of T-junction microchannel, and (b) actual picture of T-junction microchannel (Zhao et al., 2013).

The experiment also featured some additional hardware and can be seen below in Figure 16.

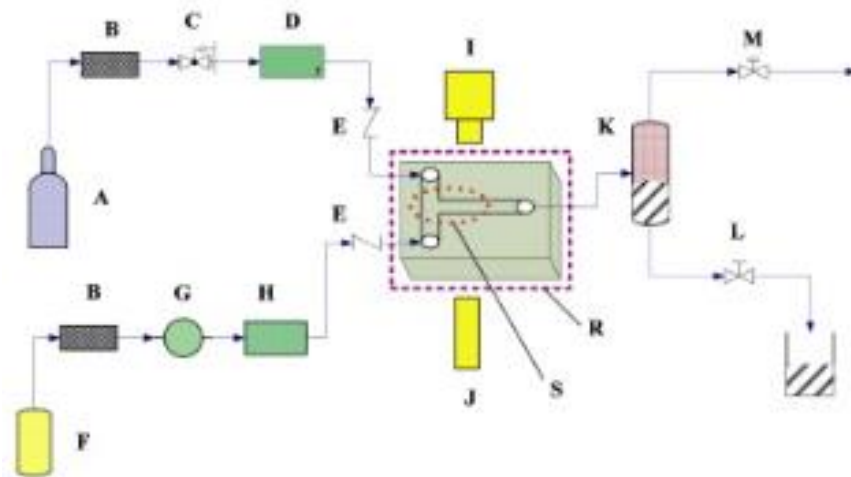


Figure 16: Schematic of the experimental setup for gas–liquid two-phase system at elevated pressure. (A), N₂ Cylinder; (B), filter; (C), pressure relief valve; (D), mass flow controller; (E), one-way valve; (F), water tank; (G), Series II digital pump; (H), liquid damper; (I), CCD high-speed camera; (J), illumination system; (K), gas–liquid separator; (L) high pressure stop valve; (M), back pressure regulating valve; (R) T-shaped microchannel; and (S), shooting zone (Zhao et al., 2013).

To record the flow patterns of the experiment, Zhao et al. (2013) used a camera system with a high performance 1000 frames per second recording capability. They used a shooting length of 15mm and it was set at the T junction as well as the area downstream of the T junction (Zhao et al., 2013). This was useful for capturing the superficial velocities that ranged from 0.062 to 23.15 meters per second.

The researchers found during their testing the gas Weber numbers will vary from 1.70×10^{-3} to 70.32 at elevated pressure and 1.37×10^{-5} to 3.46 at atmospheric pressure of around 100 kPa (Zhao et al., 2013). They found similar flow patterns will show a different set of details based on the flow pressure. They stipulate this may cause different gas-liquid mass transfer and reaction performance (Zhao et al., 2013). To summarize their work, Zhao et al. (2013) drew several conclusions from their experimental research. The first is different details and characteristics are shown in the same characterization of flow patterns such as: bubbly flow, slug flow, unstable slug flow, parallel flow, slug-annular flow, annular flow and churn flow. This is mainly due to adjusting the pressure at which they were measured and observed (Zhao et al., 2013). The researchers also discussed how Weber numbers can adjust based on changing pressures. Zhao et al. (2013) state, “The hydrodynamic characteristics of gas–liquid two phases are mainly affected by the interfacial tension of gas–liquid two phases, the gas inertia force and the liquid inertia force. The flow pattern maps are divided into five regions using We_{GS} and We_{LS} as coordinates based on their formation mechanisms. The transition lines shift to higher We_{GS} and lower We_{LS} at elevated pressure compared to the atmospheric pressure. The transition line, from zone I to II, shifts to higher We_{GS} and lower We_{LS} when the operating pressure increases from 1.0 MPa to 5.0 MPa. Other transition lines from zone II to III, from zone III to IV, and from zone III to V almost remain unchanged at elevated pressure.”

2.7 Branch Angles

Chen et al. (2013) have explored microchannel flow in their research. They explored some similar aspects related to this experimental study and are worthy contributions to the world of science and two-phase microchannel flow. The researchers in this particular paper discussed gas-liquid two-phase flow splitting at microchannel junctions with different branch angles. Many past researchers (Azzi et al., 2010; Azzopardi and Whalley, 1982; Chung and Kawaji, 2004; Hsieh et al., 2004) provided publications completed from the early 1980's all the way to the 2010's that proved to be essential to the development of the study by Chen et al. (2013). Azzi et al. (2010), Azzopardi and Whalley (1982), Chung and Kawaji (2004), Hsieh et al. (2004) and many others should be acknowledged for the instrumental work on previous projects leading to the information acquired on this project.

The researchers in 2013 used a setup including square microchannel cross-sections of 0.5mm by 0.5mm. They also assumed a completely adiabatic condition for the experiment. Chen et al. (2013) used five varying branch angles between 30 and 150 degrees. They used much faster velocities for the Nitrogen gas used than the pure water. The water was between 0.019 to 0.356 meters per second while the nitrogen was varied from 0.8 to 21.3 meters per second (Chen et al., 2013). Because of the high flow rates, the researchers had to use a high speed recording technique just as many other research experiments have needed in order to provide accurate results. This recording took place specifically at the junction at which the micro channel flow split. Chen et al. (2013) also discussed the surface area being a major factor in microchannel flow. When the size of the channels is reduced, the total surface area increases in order to carry the same mass flow rate. This increase in surface area will affect flow in multiple ways and can also increase heat transfer as discussed previously in the literature review. This is one major

reason for the heightened research happening in microchannel flow. The researchers used multiple pieces of equipment in their experimental setup. A diagram showing all the features and allowing for a visual description can be seen in Figure 17.

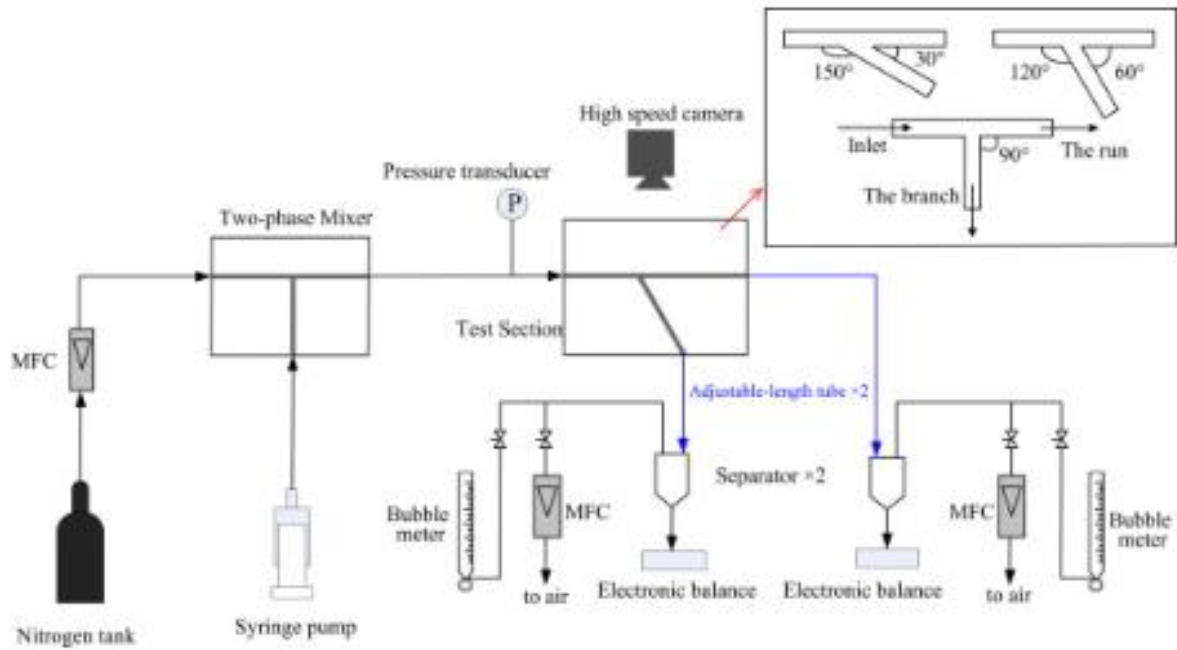


Figure 17: Schematic diagram of the experimental setup (Chen et al., 2013).

The researchers also provided information on the superficial velocities of both the gas and liquid and how this would affect the flow pattern for their particular experiment. This information can be seen below in Table 1.

Table 1: Gas and liquid superficial velocities and the corresponding flow patterns (Chen et al., 2013).

Case	U_{SG}	U_{SL}	Flow pattern
1	0.8	0.356	Slug flow
2	2.0	0.356	Slug flow
3	4.667	0.189	Slug-annular flow
4	7.333	0.104	Slug-annular flow
5	13.33	0.053	Slug-annular flow
6	23	0.033	Annular flow
7	23	0.019	Annular flow

As you can see in Table 1, as the velocity difference between the gas and the liquid increases, the flow pattern tends to turn from slug flow to annular flow (Chen et al., 2013). The research team also took several valuable images of their experimental procedures. These can be seen below in Figure 18, Figure 19, and Figure 20.

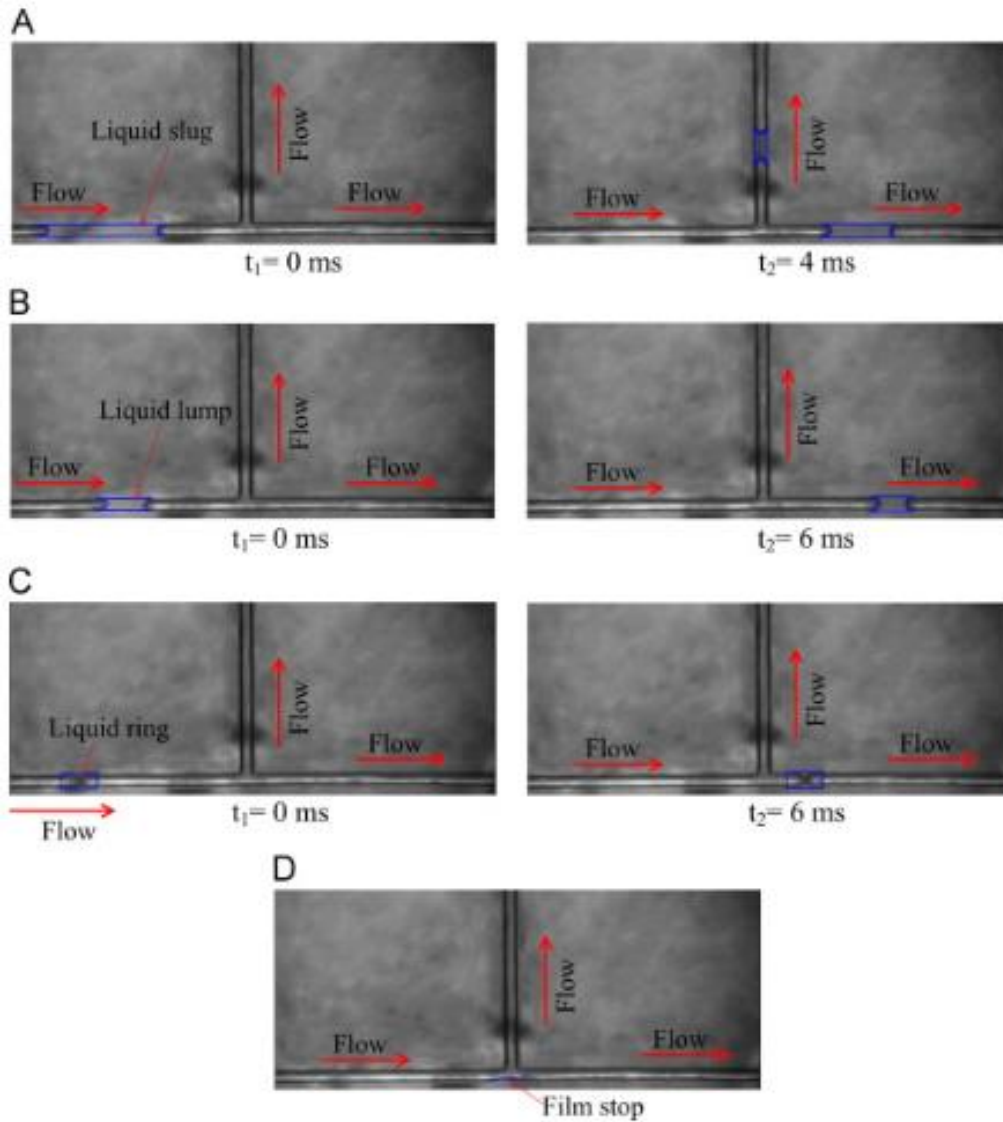


Figure 18: Time trace of liquid phase before and after the junction for each sub-flow pattern, fraction of gas taken off=0.5 (Chen et al., 2013).

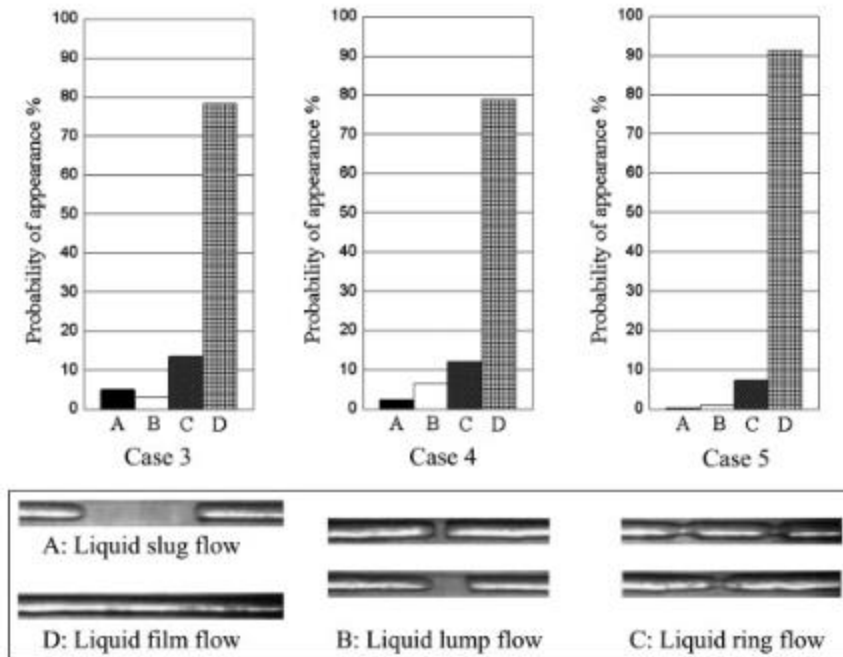


Figure 19: Probability of appearance of different sub-flow patterns of slug-annular flow for Cases 3–5 (Chen et al., 2013).

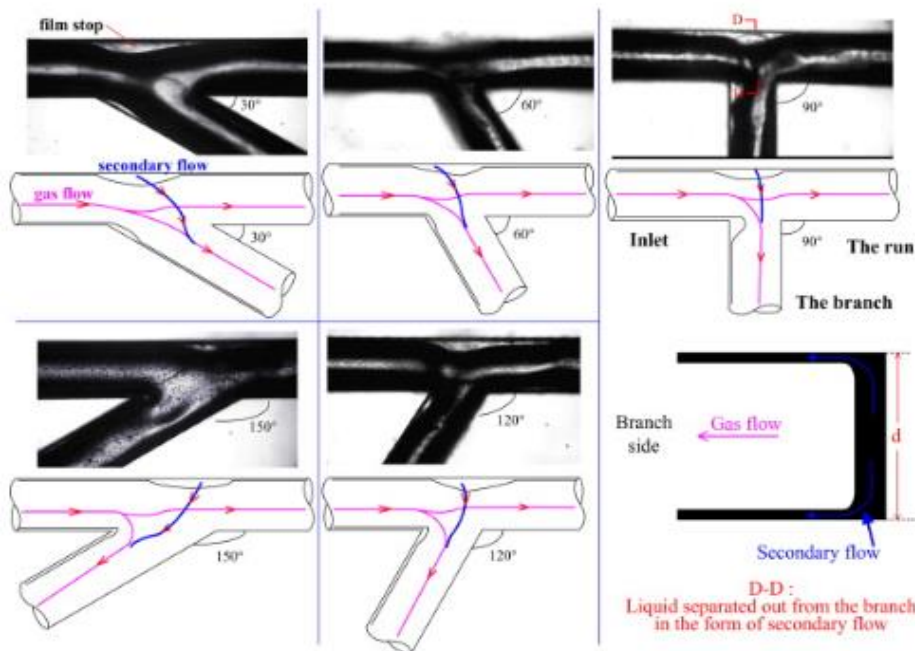


Figure 20: Captured images of film stop at junctions with different branch angles and the corresponding sketches of secondary flow (Chen et al., 2013).

2.8 Branch Angle Main Points

Chen et al. (2013) summarized three main focus points in their conclusion. The first point they mention is the flow patterns have a significant effect on the phase split at microchannel junctions. The researchers go on to say, “When the inlet is slug flow, gas phase preferentially flows into the branch while at inlet of annular flow more liquid is diverted into the branch, which is consistent with the previous study of mini- and macro-size junctions. However, for slug-annular flow, its phase split curve does not simply take on a transitional characteristic. Specifically, it gets farther away from the equal split line at first but moves up towards the liquid rich zone gradually” (Chen et al., 2013). The second focal point their main conclusion is increasing the branch angle does not guarantee an increase in liquid taken off the branch (Chen et al., 2013). During slug flow, they found as the angle was increased from 30 to 150 degrees, the amount of liquid separated out decreases due to liquid inertia (Chen et al., 2013). During annular flow, the maximum amount of liquid separation occurred at 90 degrees due to the strongest secondary flow (Chen et al., 2013). They found a transitional characteristic during slug-annular transitional flow when the angle was changed. The third and final point made in the summary of work by the research team shows more liquid is taken off the branch when using microchannel branches than with mini or macro channels (Chen et al., 2013). They believe this is attributed to phase misdistribution in microchannel junction applications. They also state that annular flow has a worse distribution than slug flow (Chen et al., 2013).

2.9 Flow through Porous Media

In the book “Essentials of Heat and Fluid Flow in Porous Media,” Narasimhan (2013) describes the essentials to understanding flow through porous media. In Chapter 3 of the book, Narasimhan (2013) begins by laying out the scientific history of studying fluid flow through porous media. He discusses past contributors such as Newton, Dupuit, Hazen, and Darcy. He then explains how they made discoveries important to research being conducted today. One of the equations created by Darcy’s Law allows differential pressure, length, viscosity, permeability, and fluid velocity to be related (Narasimhan, 2013). This was a big step in understanding fluid flow, but did not account for the losses created by form drag. To account for these losses, the Hazen-Dupuit-Darcy Model was created. This used the Darcy Model but also added a form coefficient as well as density and a square velocity term to account for both the linear effects of the viscous drag and the parabolic effects of the form drag (Narasimhan, 2013). Narasimhan (2013) also discusses Newton’s impact on the discovery and the study of form drag. To accurately determine the form and permeability constants, Narasimhan (2013) discusses using an experimental setup involving a gravity-fed system providing a mass flow rate of water through porous media. A differential pressure is then made across the porous media and divided by the distance the differential pressure is measured. The velocity is then varied and the results can be plotted with the velocity on the x-axis and the differential pressure divided by distance on the y-axis. The linear portion of the best-fit line can be then used to solve for the permeability constant and the squared term can be used to solve for the form constant. The form constant is in $1/\text{meters}$ and the permeability constant is in meters squared (Narasimhan, 2013). Using a relatively similar experimental method is the key to solving for both of the constants needed to model the flow through the porous media in question. In order to channel must be

straight and having a constant cross-sectional area. This is key to allowing the minimization of other effects besides viscous drag to be measured when determining the permeability. To reduce the uncertainty, it is also helpful to assume the wall effects are minimal for a practical experiment. In theory, they will not be zero, but this will allow the permeability to be calculated much easier. Since the flow can be either driven more by the viscous drag or the form drag, it is important to model where the flow transitions from each flow regime. Traditionally when studying internal flow, a Reynolds number can be used to determine when the flow has left the laminar stage of low velocity and entered the turbulent stage with relatively high velocity. When studying flow through porous media, the traditional Reynolds number cannot be used. A traditional Reynolds number uses a velocity, unit distance, and a viscosity. Narasimhan (2013) suggests using the square root of the permeability as the unit distance for calculating a modified Reynolds number based on permeability. This does not account for the form drag portion of the flow (Narasimhan, 2013). Narasimhan (2013) uses a lambda term to compare the form to viscous drag. The lambda term is a modified Reynolds number using also including the form constant explained previously. When lambda is greater than one, form drag is dominating the flow and when it is less than one, viscous drag is dominant (Narasimhan, 2013). The graph Narasimhan (2013) created to show the percentage of drag viscous and form effects are having on the flow can be seen in the results and discussion chapter of the thesis. Narasimhan (2013) also states that the previous calculations were all under the assumption of isothermal flow.

2.10 Turbulent Flow Through Porous Media

Barr (2001) discussed flow through porous media and different factors that influenced the flow. One of the first factors considered is whether the flow is considered to be laminar or turbulent (Barr, 2001). According to Barr, the pressure driving the flow through porous media when laminar or turbulent must be equal to the resistance of the fluid to flowing. When the flow is laminar, the resistance to flow will be entirely due to viscous forces. These forces are a result of the viscosity of the fluid and the zero wall velocity (Barr, 2001). When the flow is turbulent, the resistance to flow will come from two different sources. The first source is the viscous force, which is also found in laminar flow. The second source is from inertial resistance. Barr (2001) goes on to explain there are many instances where turbulence can occur in porous media. A few examples are a low viscosity liquid or a gas is used as the medium. Traditional water can also become turbulent under many circumstances. Barr (2001) elaborates on this issue and explains coarser porous media can cause the water to become turbulent much easier than a smooth porous media. Barr found experimentally the turbulence begins for the porous media and fluid tested at a head gradient of about 0.1 (Barr, 2001). Another conclusion drawn from this research shows the equation for permeability in laminar flow depends on density and viscosity of the fluid and porosity and hydraulic radius of the pores (Barr, 2001). Barr also used separate expressions to model both laminar and turbulent forces. When flow was determined to be laminar, Equation 2.10.1 represents B as the ratio of viscous resistance to driving pressure force through porous media. Equation 2.10.2 represents E as the ratio of inertial resistance to the driving pressure through porous media. Finally, Equation 2.10.3 represents a general expression for flow through porous media and is applicable to flow in laminar and turbulent regimes where the hydraulic radius cannot be determined (Barr, 2001). It should always equal 1 for this equation.

$$B = 5\mu V/\rho g \alpha m^2 (h/l) \quad 2.10.1$$

$$E = 2^{0.5} V^2/\alpha^2 g (h/l) 3m \quad 2.10.2$$

$$I = 5\mu V/\rho g \alpha m^2 (h/l) + 2^{0.5} V^2/\alpha^2 g (h/l) 3m \quad 2.10.3$$

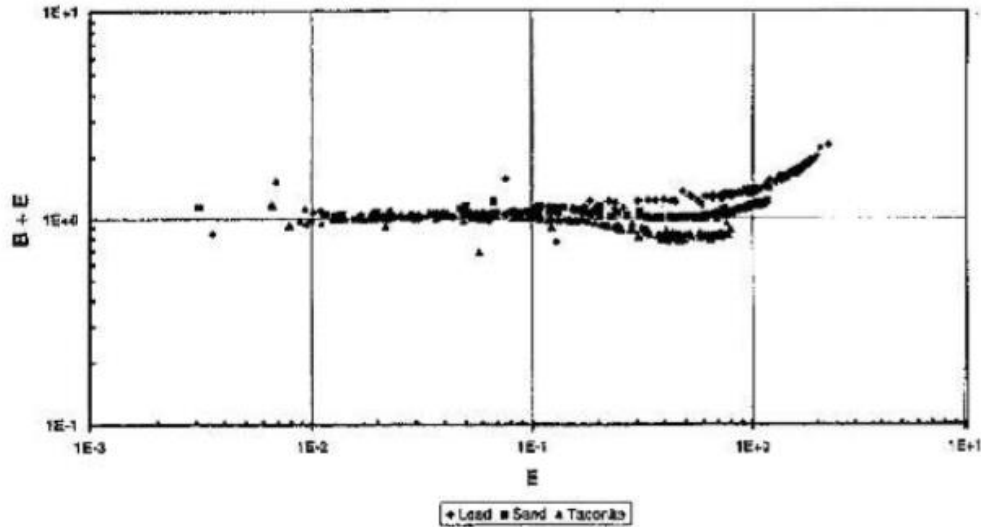


Figure 21 Plot of sum of B + E should equal 1. The plot of sum splits according to particle shape in the turbulent range (Barr, 2001).

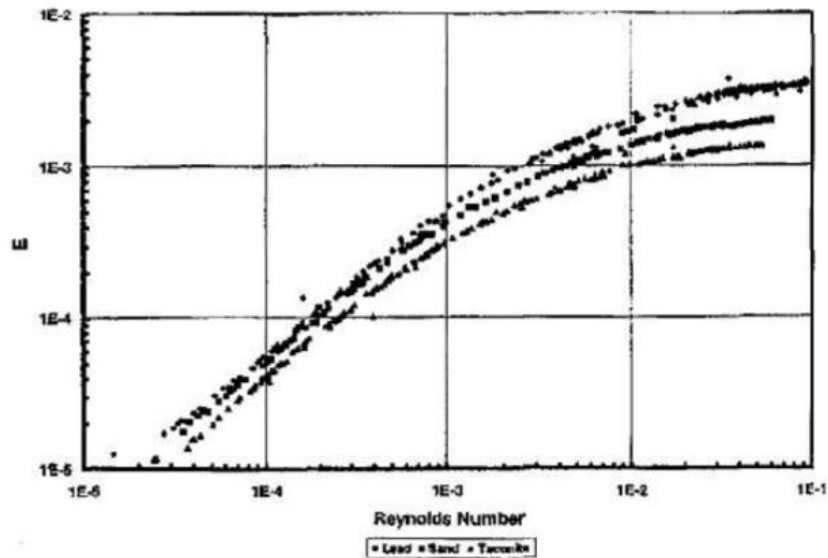


Figure 22: Dimensionless number E vs Reynolds number (Barr, 2001).

2.11 Using Porous Media Approximation to Model Microchannel Heat Sinks

Lim et al. (2010) used a technique of modelling the microchannels of a heat sink application as a porous media heat transfer application. This was then applied to a full three dimensional CFD simulation. The researchers found the simulation agreed well with the findings of previous methods of analytical and experimental research findings (Lim et al., 2010). The methodology was also found to be quite useful because the results were not dependent on the assumption of fully developed flow both thermally and hydraulically (Lim et al., 2010). This allows many more developing flow applications to be analyzed. There were also less computational requirements using this method versus previous methods making it an increasingly attractive way to model in CFD. Both microchannels and porous media have a very high surface area to volume ratio making the modeling as a porous media an effective means of measurement.

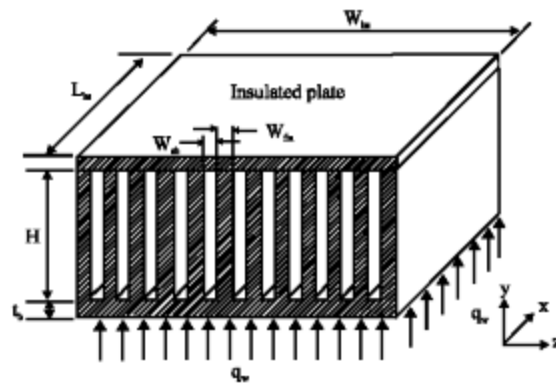


Figure 23: Schematic diagram of the microchannel heat sink (Lim et al., 2010).

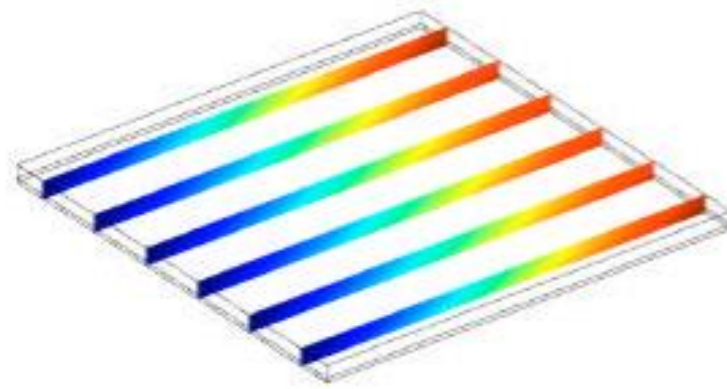


Figure 24: Temperature distribution of porous media microchannel (Lim et al., 2010).

2.12 Nanofluid Technology Overview

Throughout history, many people have been using nanotechnology for the benefit of their respective civilizations and cultures. They had no idea they were utilizing the technology, they just knew if they followed a specific procedure, the outcome would produce a favorable device with performance characteristics more advanced than the current equipment. An example of this is the Lycurgus cup. Today, we are constantly learning more about science at the nanoscale and using it to our advantage. We are trying to understand specific concepts and principles behind nano-behavior, and use them to develop new technology to advance our society. Much of the advance in nanoscience has been due to the advent of imaging devices such as the scanning electron microscope. This has allowed scientists to visually understand key concepts, and apply them to useful pieces of nanotechnology.

2.13 Nanofluid Properties

One of the exciting new advances stemming from new research in nanoscience is nanofluid technology. Nanofluids by definition are fluids with nanoparticles suspended in the fluid

(Pastore et al., 2012). The particles are less than or equal to 100 nanometers in diameter. The particles are typically made from substances much denser than the fluid in which they are suspended. If the particles are to remain suspended and not settle out eventually, there must be a driving force to keep them in place for long periods of time. To provide this force, a much higher surface area to volume ratio is needed (Pastore et al., 2012). As the diameter of spherically shaped particles decreases, the ratio of surface area to volume increases dramatically. Take for example a one meter diameter spherical ball. The total surface area of the ball will be π meters squared and the total volume will be 0.5236 m^3 . This gives a surface area to volume ratio of about 6 to 1. If a total volume of $.5236$ meters cubed nano-sized particles of 100 nanometer diameter were used instead of the one large sphere, the total surface area would be $\pi \times 10^7$ meters squared. This would result in a total surface area to volume ratio of 6×10^7 . The significance of this fact cannot be overstated. Increased surface area is vital to keeping enough attractive forces on the suspended nanoparticles to overcome the gravitational force trying to displace the fluid and bring the denser particles to the bottom of the reservoir (Xuan and LiHigdon, 2000). This term paper will allow me to show in detail some of the truly remarkable advances in nanofluid technology using some of the research of engineering researchers. I will now go into depth showcasing a few revolutionary advances in this developing field.

2.14 Shear-Thickening Nanofluid Applications

Pastore et al. (2012) have been working on a new revolutionary way to help protect people or objects from high velocity penetration and damage. Their idea utilizes the unique properties of nanofluids to help make this a reality. For many decades, the best approach to stopping a high velocity projectile in a short distance is using a high strength fiber known as Kevlar. This material is one of only a few recently discovered materials that have the strength to stop a bullet

from penetrating a human, without making the human incredibly immobile and uncomfortable. The key to the success of Kevlar lies in the strength to weight ratio. Pastore et al. (2012) tried to improve upon the previous generation technology by incorporating a combination of Kevlar and shear-thickening nanofluids. Many fluids we use commonly in day-to-day life are known as Newtonian fluids. This essentially means the shear rate versus shear stress model will provide linear results. The slope of this line is known as the viscosity of the fluid. Viscosity is the parameter in fluid mechanics used to describe the resistance of a fluid to flowing. Calculating the viscosity of Newtonian fluids is quite simple because of their linear characteristics. However, many substances do not follow this linear pattern of behavior. They are referred to as non-Newtonian fluids. There are two different varieties of said fluids: shear thickening and shear thinning. The viscosity of a shear thickening fluid will increase when a higher shear rate is applied. A shear thinning fluid will do the exact opposite of a shear thickening fluid. A majority of fluids that are non-Newtonian are the shear thinning variety. Nanofluids can be shear-thickening property making them highly unique and useful for a number of applications. To better understand this principle, Figure 25 shown below illustrates this principle well.

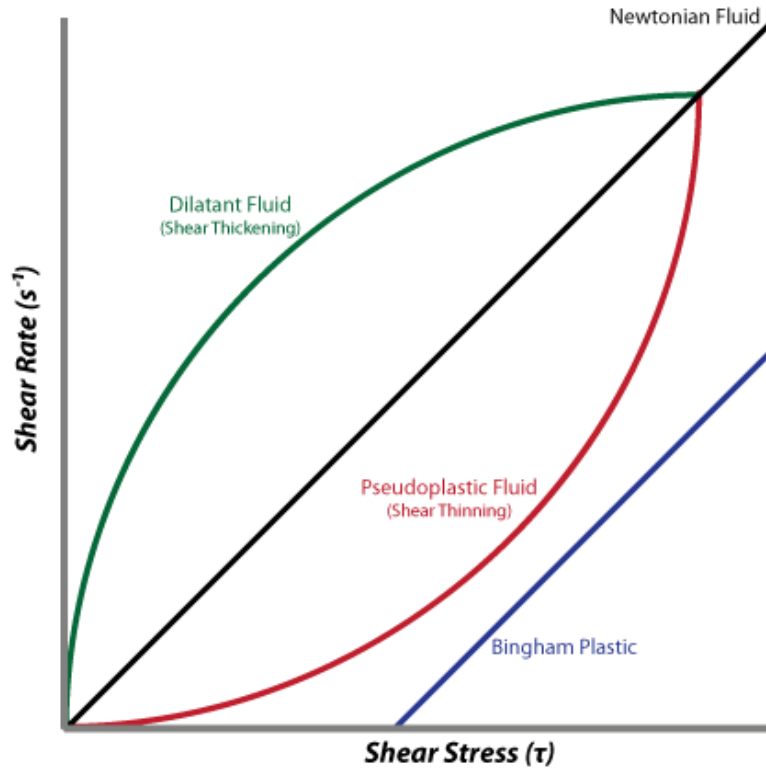


Figure 25: Shear rate vs. shear stress for shear thickening, Newtonian, and Shear thinning fluids, and Bingham plastic (Pastore et al., 2012).

Pastore et al, (2012) decided to compare different weight percentages of nanosilica for their experiment. They demonstrated the Non-Newtonian behavior shown in Figure 25. Notice how the viscosity increases as the weight percentage of nanosilica increases in their tests (Pastore et al., 2012).

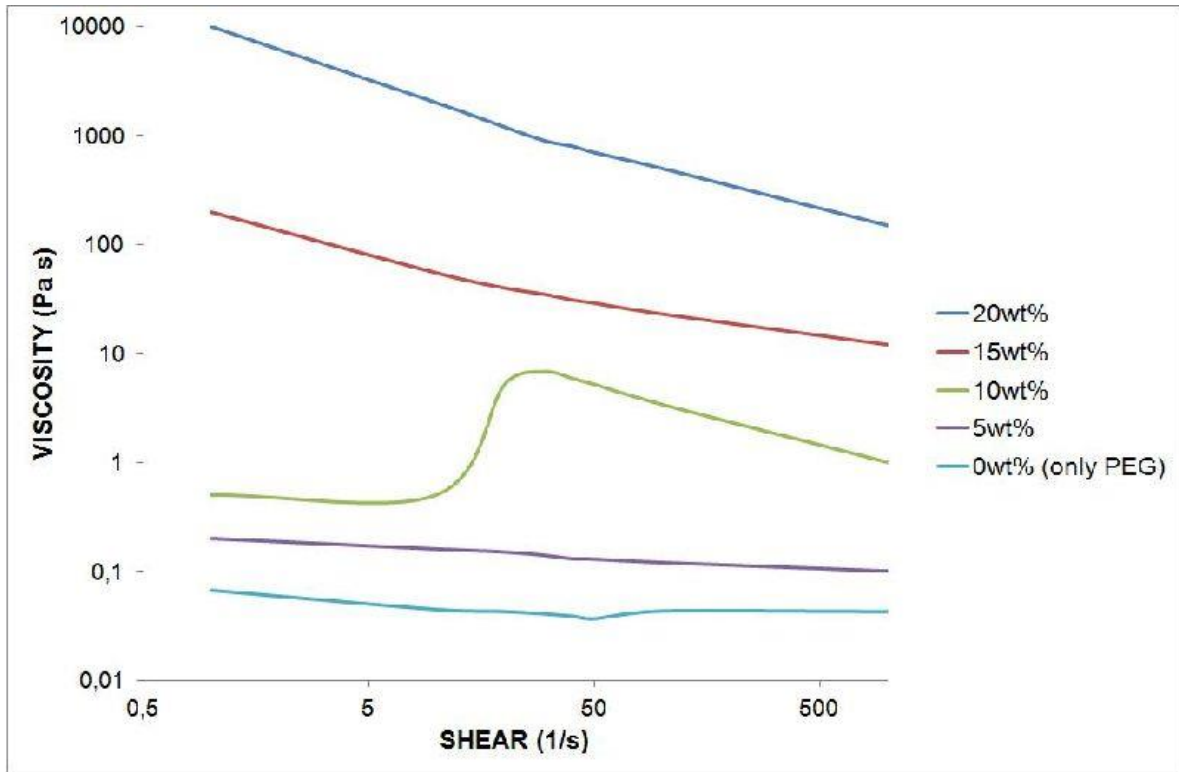


Figure 26: Logarithmic scale of viscosity vs shear rate for multiple percentage weights of nanosilica (Pastore et al., 2012).

The nanosilica selected had an average diameter of 70 nanometers. This was specifically selected for the tremendous surface area to weight ratio as mentioned above. The experimental setup consisted of a shear-thickening nanofluid used in conjunction with Kevlar fibers to test the durability of the lightweight test material. The projectiles were accelerated with an electromagnetic accelerating device known as a coil gun (Pastore et al., 2012). They went into depth discussing the electrical engineering behind the coil gun, but for our intents and purposes, I will focus on the results and how the shear-thickening nanofluid performed. A major performance parameter of how well the fluids performed is relative absorbed energy. The article compared the performance in this key characteristic for a number of low and high energy applications at various concentrations. This information is tabulated in Figure 27 below. Notice

how the relative absorbed energy increases in all four cases as the concentration increases. The equation describing the absorbed energy in the tests is: $\Delta E = (E_{inc} - E_F) / E_{inc}$ where: $\Delta E =$ absorbed energy, $E_{inc} =$ incident bullet's energy, $E_F =$ Friction physical work (Pastore et al., 2012).

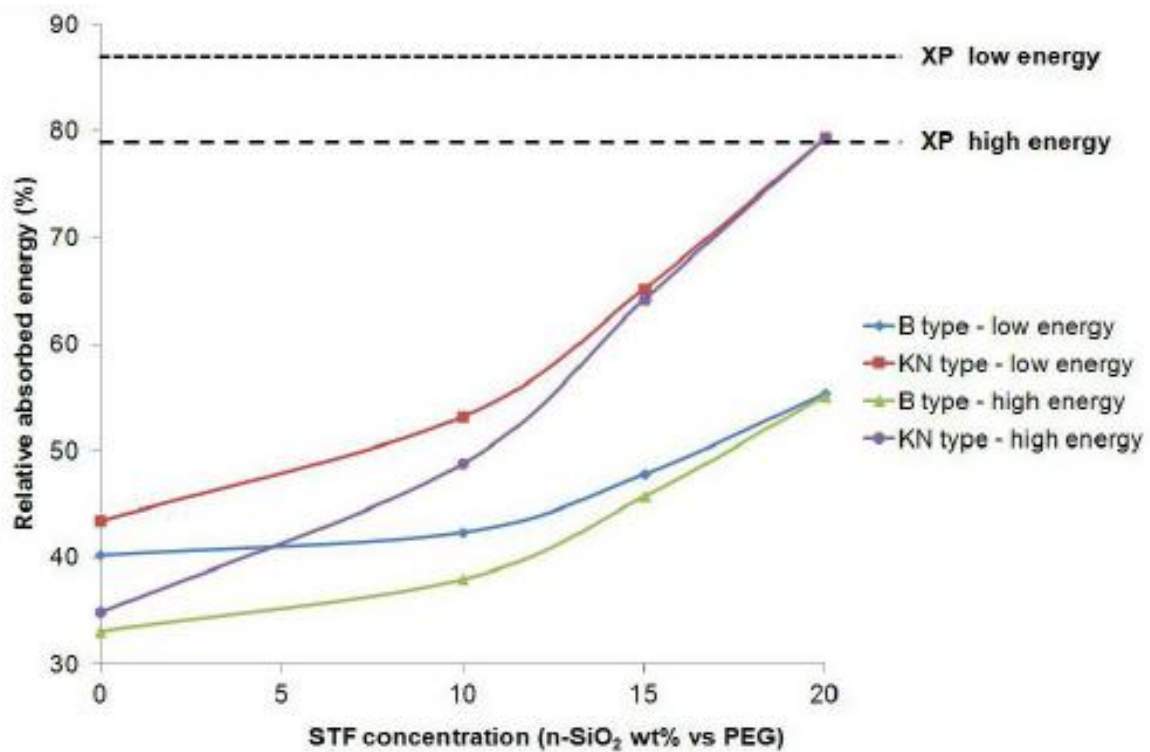


Figure 27: Relative absorbed energy vs. shear-thickening fluid concentration (Pastore et al., 2012).

Upon conclusion of the testing, several recommendations were made by the researchers responsible for the interesting data. The first is reinforcing the Kevlar test samples with a silicon oxide shear-thickening nanofluid increased the ability of the test samples to resist a high velocity projectile under a number of different energy tests (Pastore et al., 2012). They also were able to produce a higher relative absorbed energy than with Kevlar alone. The second major conclusion

drawn by the researchers was a higher weight percentage of the silicon oxide will produce a higher relative absorbed energy and will ultimately provide a better barrier for stopping high speed projectiles. Future testing on shear-thickening nanofluids recommended by the researchers would be the investigation of flexibility for practical prototypes instead of using a stiff model in the lab. Once the flexible models have been perfected, real-life armor could be produced for helping a variety of soldiers, law enforcement, and other people in need of lightweight, high performance bulletproof materials.

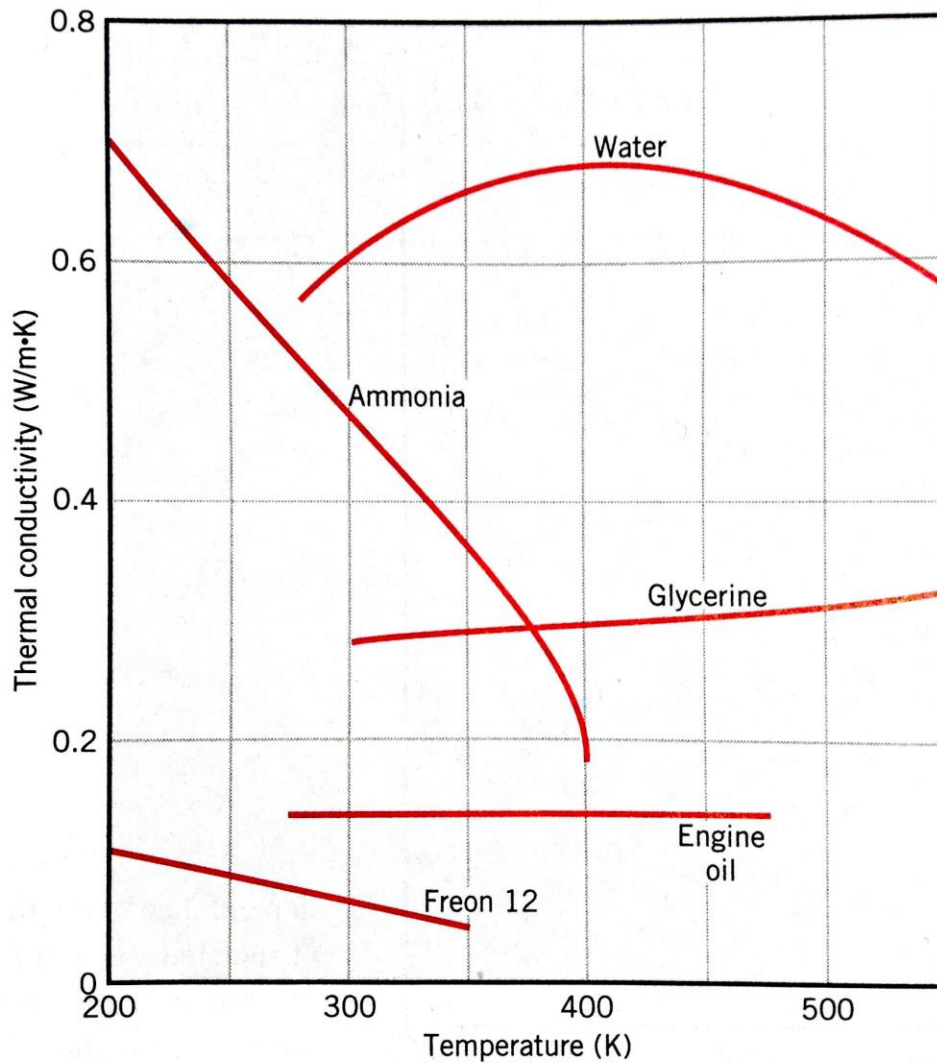


Figure 28: Thermal conductivity vs. Temperature of common liquids (Bergman et al., 2011).

2.15 Nanofluid Heat Transfer

Over the past 150 years, people across the earth have been exploring ways to manipulate the transfer of heat. The ability to efficiently transfer heat and energy is still being explored in cutting edge research (Xuan and LiHigdon, 2000). The use of nanofluids has opened the door to new fluids capable of transferring heat at a faster rate with less material (Xuan and LiHigdon, 2000).

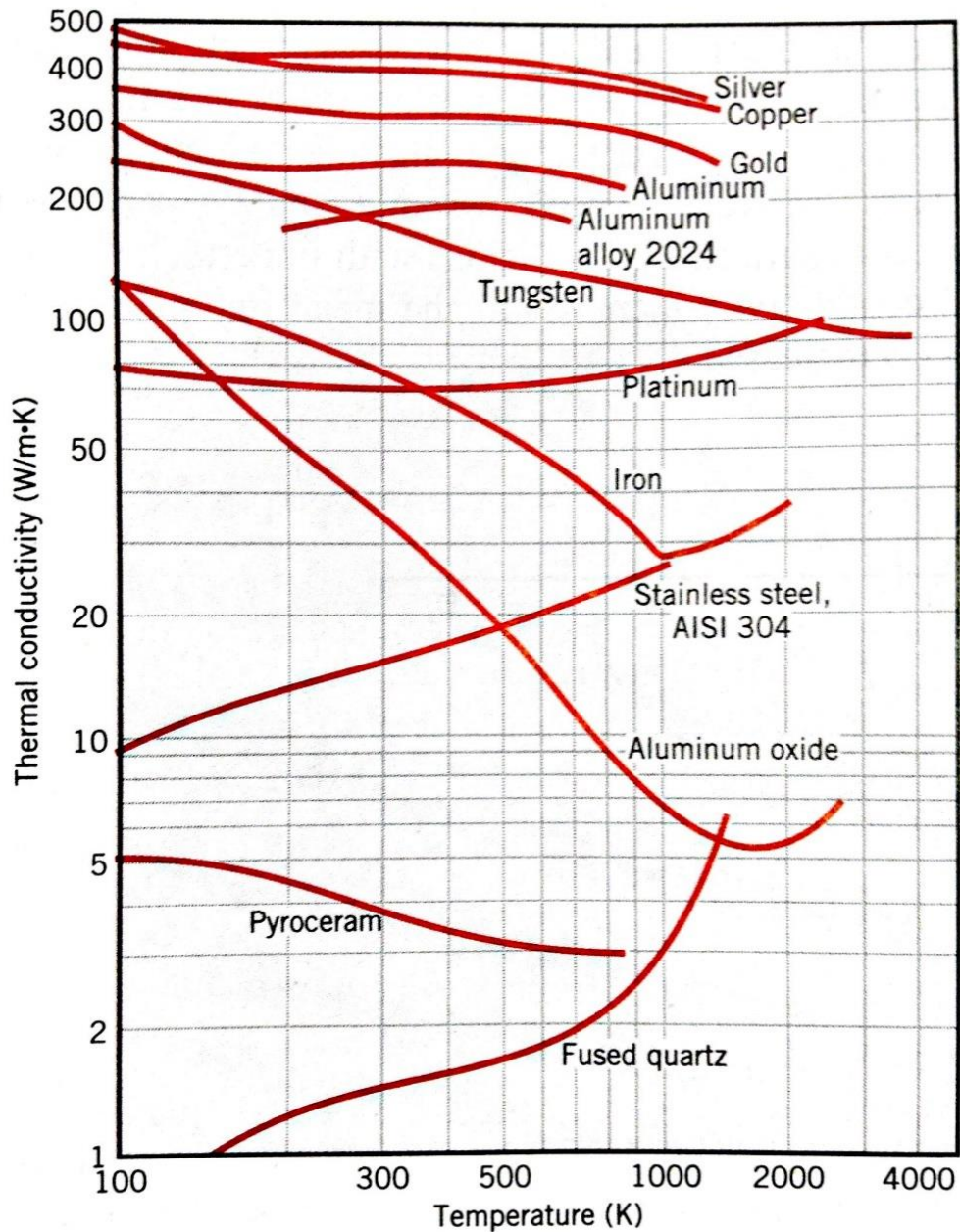


Figure 29: Thermal conductivity vs. Temperature of common solids (Bergman et al., 2011).

In general, fluids such as oil and water are able to hold much more heat than metallic materials, but metals are generally much better at quickly transferring the heat to another substance (Xuan and LiHigdon, 2000). The rate at which a material can transfer heat is known as thermal conductivity (Bergman et al., 2011). In Figure 28 and Figure 29, the thermal conductivities of

several materials are shown. Notice the difference between the liquids and the solids is significantly larger. In some cases, the solids have 500-1000 times higher thermal conductivity (Bergman et al., 2011). Nanofluids aim to combine the characteristics of both materials. This has had an impact on a number of industries, with the potential for many more future applications (Xuan and LiHigdon, 2000). Nanofluid heat transfer could be highly relevant for use in potential NASA applications. Regulating heat transfer is highly important because of the thermally rapidly fluctuating environment of space. Cooling and heating applications are used on many missions. The development of a smaller and lighter cooling device could be utilized on a variety of missions. This would eliminate excess mass, allowing for the usage of: a smaller fuel cell, more onboard scientific equipment, ability to capture more material in mining applications, and a larger acceleration for faster travel. The data obtained from research could also lead to the design of a more efficient space suit. This could increase the reliability and decrease the mass of the suit. The comfort of the astronaut completing the mission would also be enhanced with a more consistent operating temperature, leading to better performance in high-stress situations. Heat transfer is also important in many power system applications (Xuan and LiHigdon, 2000). Transformers used in the power industry allow voltages to be changed. However, there is wasted energy and a cooling liquid is needed to enhance heat transfer. Xuan and LiHigdon (2000) researched the ability of nanofluids to be used in transformers to increase the thermal conductivity of the oil inside the transformers. They found the thermal conductivity increased significantly when the oil was replaced with a nanofluid, as shown in Figure 30 (Xuan and LiHigdon, 2000).

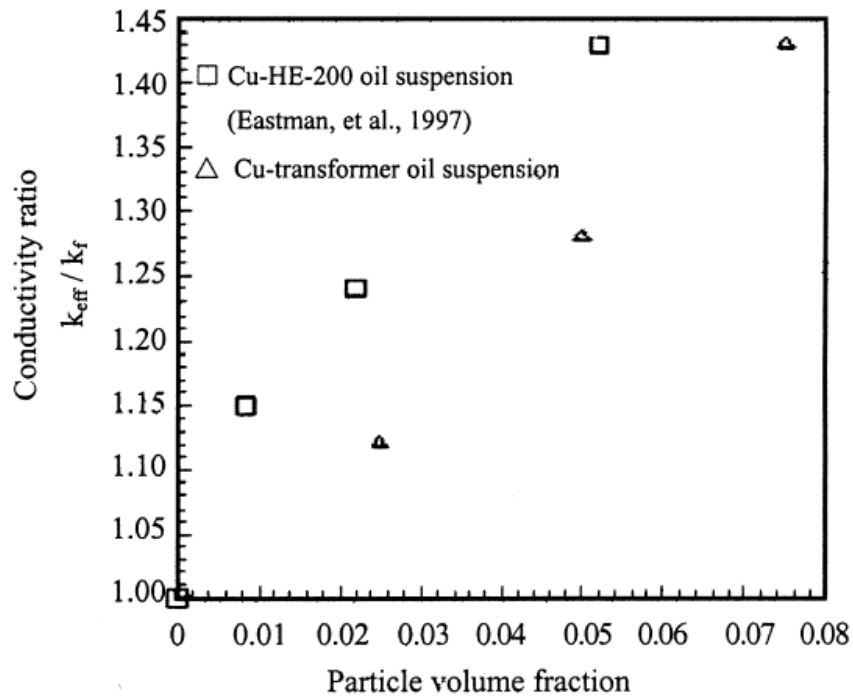


Figure 30 Conductivity ratio vs Particle volume fraction of a few selected nanofluids (Xuan and LiHigdon, 2000).

2.16 Nanofluid Societal Impacts

Many researchers have provided valuable data showing how nanofluids can have a lasting impact on society. Increasing the ability of substances to transfer heat is of high importance to current research (Xuan and LiHigdon, 2000). Xuan and LiHigdon (2000) state, “Low thermal conductivity of process fluid hinders high compactness and effectiveness of heat exchangers, although a variety of techniques is applied to enhance heat transfer. Improvement of the thermal properties of energy transmission fluids may become a trick of augmenting heat transfer.”

Mangalgi (1999) states, “The importance of stopping high speed projectiles should not be overlooked. In the last decades the research on composite materials have been acquiring importance due to the possibility of increasing the material mechanical performances while contemporary decreasing both mass and volume of the structures. Mass lowering is a “must”

especially in military and space applications, since aircraft aerodynamic profile needs to be optimized and because of the high costs of launch and launcher and payload mass constraints.”

Exploring new substances such as nanofluids is opening a new field for engineers to research and develop products that can help solve modern-day engineering problems. With more research and development, we will see many more advances in the years to come.

CHAPTER 3

EXPERIMENTAL SETUP AND METHODOLOGY

3.1 Overview

To fully understand the process of the experiment, I will first go into detail describing the experimental setup. The first physical feature of the process is our pumping system. The pump drives the flow in the process and allows for a continuous flow of water or any fluid that would be desirable to analyze. After considering many options, the decision was made to utilize a syringe pump for this specific application. Syringe pumps in general have many advantages. The first advantage is the ability to precisely apply a constant and specific mass flow rate of liquid through our system. Further analysis of syringe pumps indicated they are also an excellent option for unique fluids. There is currently a significant amount of interest in studying nanofluids. These fluids can be a challenging substance with which to work primarily because of the size of the particles suspended in the fluid. The particles on a nano scale will slip by traditional seals and can build up in unwanted locations. This can produce unwanted friction and wear down equipment extremely quickly. Using a syringe pump will reduce this effect significantly because the driving motor never comes in contact with the nanofluids. The nanofluid will be contained within relatively inexpensive syringes that can be disposed and replaced by new syringes when a new fluid is to be studied. Both of these reasons provide significant advantages over traditional pumping units. Peristaltic pumps would also be a good choice for reducing the wear and tear of using unique or exotic fluids. The large downfall of using a peristaltic pump is the pumping power and mass flow rates are too small for these

applications. Syringe pumps on the other hand will provide the system with enough pumping power to create laminar or flows with the onset of turbulence in the channel which will give the experiment testing flexibility. The experiment for this thesis will be primarily conducted using water in a single-phase flow, but having the flexibility to use the same experimental setup and compare the data to a nanofluid application with equivalent testing parameters will enable future work to be conducted without having to purchase new equipment. This will undoubtedly save time and money.

3.2 Syringe Pump

The syringe pump chosen for the experiment is the Nexus 3000 with a continuous flow rack attachment and can be seen below in Figure 31.



Figure 31: Nexus 3000 syringe pump with optional continuous flow rack and four 140 mL Monojet syringes installed

The Nexus 3000 is built by Chemyx and has specifications ideal for this particular application. The range at which the Nexus 3000 can provide accurate mass flow rates is quite exceptional. The flow rates can range from 0.00001 microliters per minute all the way to 300 milliliters per minute. This range is not only ideal for the relatively high volumetric flow rates of the current testing, but also for continued research into extremely slow flow rates resulting in laminar flow. The Nexus 3000 is also programmable for continuous flow applications, along with a series of settings allowing unique flow pattern options. It also provides a relatively high accuracy and reproducibility performance metrics of plus or minus 0.35% and 0.05%, respectively. To ensure our flow rates were accurate, an uncertainty analysis was performed on the pump. The uncertainty analysis procedures described by Kline and McClintock (1953) and Moffat (1988) were utilized to quantify the uncertainties encountered in this experimental study. The first step was to program the Nexus 3000 for a series of volumetric flow rates. The flow was then measured in a 10 milliliter graduated cylinder for low flow rates and a 50 milliliter graduated cylinder for relatively high flow rates. Volumetric flow rates measured varied from 2 milliliters per minute to 300 milliliters per minute. To ensure the analysis was valid, each individual test was rerun for a total of five runs per flow rate. Once this data was recorded, the uncertainty analysis was conducted taking into account the uncertainty of the data from the analyzed data, the pump, and the graduated cylinder. The final volumetric flow rate uncertainty was determined to be plus or minus 1.704 milliliters per minute or in terms of percentage, an average of plus or minus 1.17% with a 95% confidence level. Figure 32 below illustrates linearity of the uncertainty analysis.

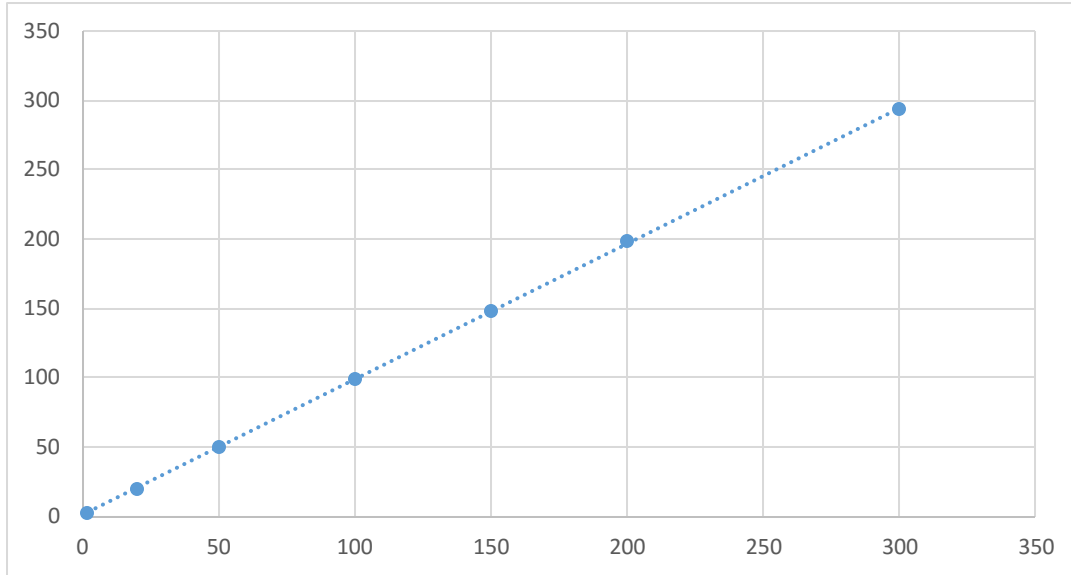


Figure 32: Claimed vs calculated syringe pump flowrate of ± 1.703828 ml/min and average error of $\pm 1.17\%$ with an R^2 value of 0.9999.

Flexible plastic tubing was then connected to the syringe valves that allow a continuous flow by having one set of syringes withdrawing and the other infusing at the same time. When the pump changes direction, the valves then switch from infusing to withdrawing or from withdrawing to infusing depending on the direction of force and which syringe is being analyzed. The infusing flow then is sent to the test section being analyzed.

3.3 Flow Test Sections

There are a total of three different test section orientations that will be analyzed. The first section that was analyzed was a square 1.59 mm channel with an abrupt expansion to a 1.59 mm by 6.35 mm rectangular channel. This allowed for two unique experiments to be considered with the exact same infrastructure by simply changing the side in which the flow is infused. A picture of the test section can be seen below in Figure 33



Figure 33: Image of test expansion and contraction test section. The square section is on the left side of the image and the rectangular, larger channel is on the right side.

This test section was developed with Creo 3D product development software and produced with a computer numerical control machining device. The raw material was made from 6061 aluminum and produced with the assistance of Jay Evenstad. The test section features a round inlet and outlet diameter of 1.5 millimeters. A 3D image of the test section viewed on Creo Parametric software can be seen below in Figure 34.

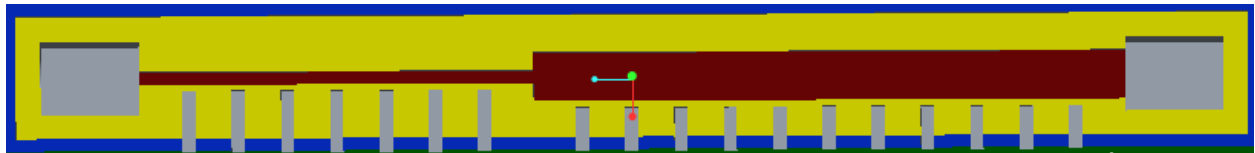


Figure 34: Creo Parametric 3D model top view of the expansion and contraction test section.

The test section also has the ability to study thermodynamic effects using a constant heat flux attached to the opening on the bottom of the test section. Thermal effects were not studied for this specific experiment, but will be studied in depth during testing at a later date. The constant heat flux can then be measured with the openings for thermocouples as seen in Figure 34. This will allow further exploration into the heat transfer rate and other notable areas of interest during subsequent testing. The inlet and outlet also have a thermocouple sensor to relay the temperature to the computer and allow the density of the fluid to be recorded independently for each run. There are also 10 pressure taps machined into the top of the test section to allow the static pressure at each location to be analyzed. These taps were carefully designed to allow the pressure to be accurately measured and the flow to be minimally impeded, resulting in accurate and precise pressure measurements. Each round pressure tap hole directly touching the flow along the channel has a diameter of 0.8 millimeters but then quickly expands to 1.6 millimeters for ease of connecting and sealing the pressure taps to the plastic tubing. The second test section allows testing of flow through a porous medium. The setup is similar to the previous test section except this test section is symmetrical and will allow flow in both directions with the same results. The test section is comprised of a base, middle and top sections. A picture of the unassembled base test section can be seen in Figure 35.

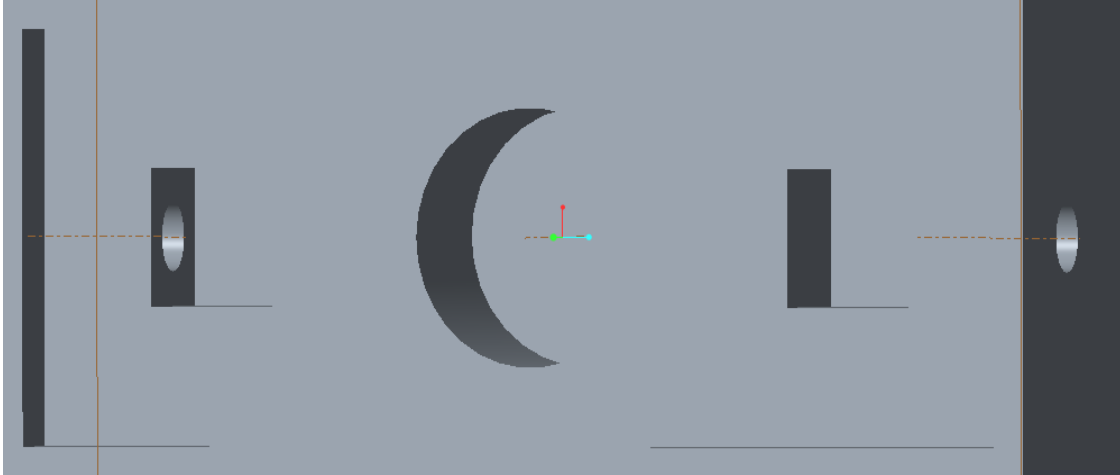


Figure 35: 3D model created with Creo Parametric software

The porous media was then added to the base section in the cylindrical hole in the middle of the flow passage. The porous media was then carefully manufactured and filed to fit well inside the passage. A 3.175 by 1.5875 mm rectangular extrusion was then manufactured from the top of the test section to provide a precise fit for the middle section slot seen below in Figure 37 and Figure 38. The middle section with the porous media in the designated slot can be seen below in Figure 36.



Figure 36: Base section with porous media inserted into testing slot

The middle section is a simple plate with a channel cut in the middle to provide a 3.18 mm passage for water to flow through. The height of the channel is 1.59 mm giving the channel a rectangular flow passage. This design also allowed sharp edges to be created that would not have been possible had the passage been integrated into the base test section given the rounded nature of the bits used in the CNC manufacturing process. This design also allows for future testing flexibility due to the replaceable nature of the middle test section. The middle piece can be seen below in Figure 37.



Figure 37 Image of middle test section used in the porous medium testing.

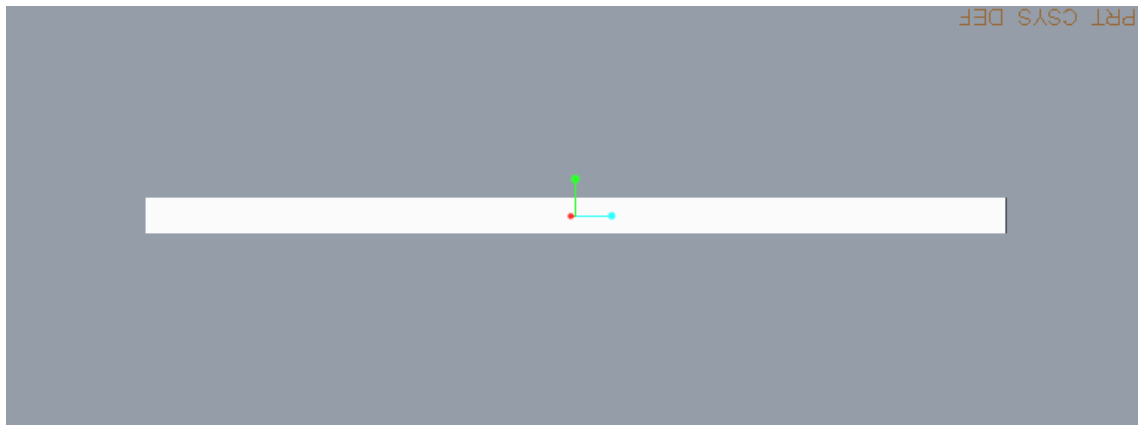


Figure 38: Image of middle piece created with Creo Parametric software

The top test section allows for 10 pressure transducers to be attached to pressure taps 1.5875 mm in diameter. The diameter is changed to 0.876 mm diameter at the interface between the fluid flow and the top test section to ensure there is minimal influence by the pressure taps on the flow. During the testing the flow is assumed to be unaffected by the small pressure holes

touching the flow surface. A 3D Creo Parametric image of the top piece can be seen below in Figure 39.

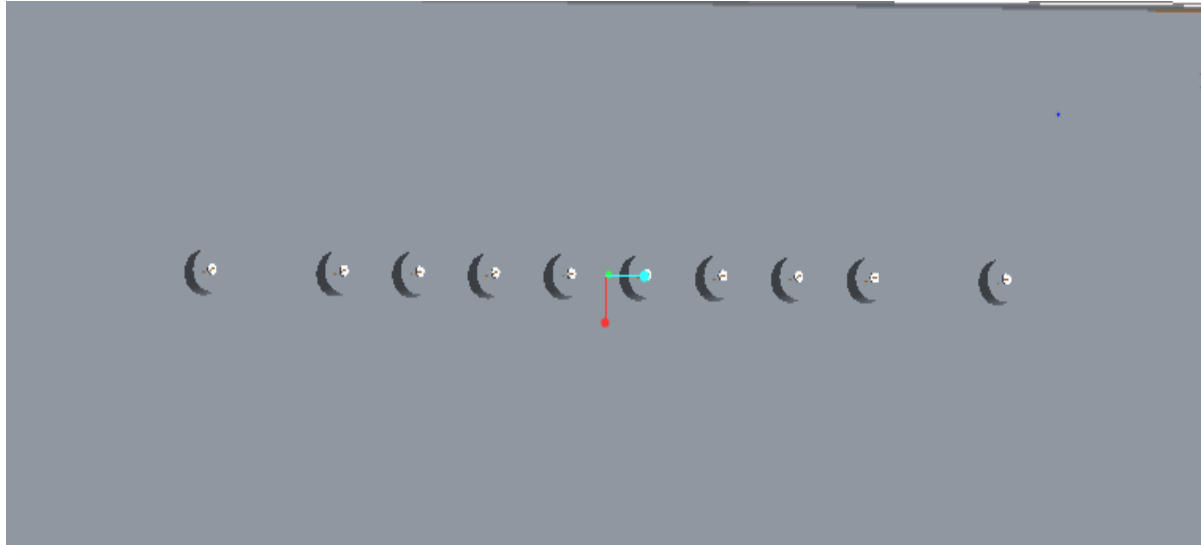


Figure 39: Top view of the top piece created with Creo Parametric Software

There is a reservoir on both the entrance and exit side of the flow. This is connected to the inlet and outlet by a 6.35 mm diameter hole and can be seen in Figure 40.



Figure 40: Inlet and outlet hole connecting the reservoir to the system tubing.

3.4 Porous Media

The porous media insert is comprised of titanium dioxide and was produced by Dr. Gupta who is a professor of mechanical engineering at the University of North Dakota. His area of expertise is material science and generously provided the test section for the experiment. He developed a new way to synthesize titanium dioxide and allowed fluid flow testing of his material. It is developed from polyethylene, graphite, and titanium and sintered at 1450 degrees C. The material has a porosity of 60 percent and microstructure is anisotropic due to the use of flaky graphite particles as pore formers (Gupta & Riyad, 2014). The material can be seen below in Figure 41.

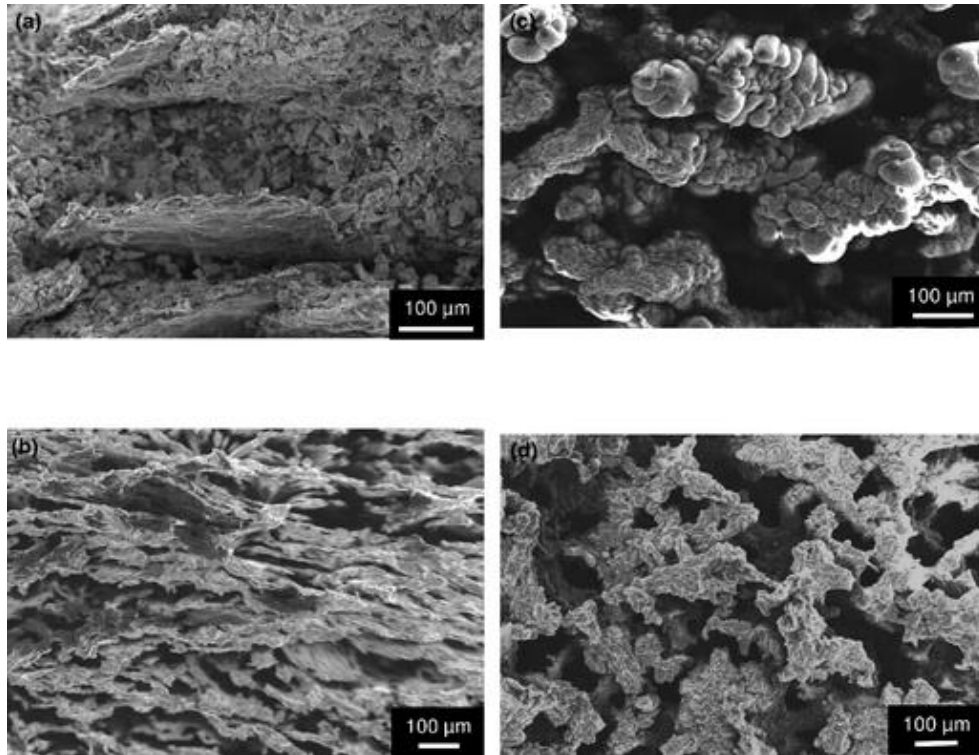


Figure 41: SEM micrographs of (a) fractured surface of the cross section of the green body of Composition C (Table 1), (b) fractured surface of the cross section of Composition C, (c) fractured surface of the cross section of Composition E (Table 1), and (d) top surface of the composition E after heat treatment at 1450 °C for 4 hours (Gupta & Riyad, 2014).

3.5 Uniqueness of Porous Media Experiment

A critical aspect of the experimentation involving the titanium dioxide porous media insert is the unlikeliness of any experimentation found during the research for the literature review. This is mainly due to the fact the titanium dioxide sintering process was recently patented by Dr. Gupta (Gupta & Riyad, 2014). In addition, the material has never been tested in this manner when produced with Dr. Gupta's sintering methods. Discovering new materials and methods of producing them allows the previously perceived limits of science and engineering to be broken. Producing materials with more advanced material properties allows products to be made for

previously unachievable goals. Using a titanium dioxide ceramic material is also intriguing for use in high temperature environments due to the relatively high melting point of 1843 degrees Celsius. Titanium dioxide ceramics also has a relatively high electrical resistivity of 1×10^{11} ohm meters while having a respectable thermal conductivity of around 10 Watts/meter Kelvin. This has a number of applications including high temperature heat exchangers. Traditional steel and aluminum alloys would melt at very high temperatures, but ceramics can withstand the temperature and allow heat transfer to occur in these applications. Further study of ceramics such as titanium dioxide will allow new applications to be developed in the future.

3.6 Microscope

Additional magnified views were made possible by the Amscope microscope seen below in Figure 42. This microscope has a total magnification of 225 times and allows for easily moving the viewing glass with an extendable booming feature. The microscope also allows digital images to be rendered with the optional digital camera included in the experimental setup. This will also be extremely useful for future experiments because of the ability to take live pictures of two-phase flow to study the formation of gas flow and determine which bubble type is being implemented. A picture of the microscope can be seen below in Figure 42.



Figure 42: Amscope microscope with boom and optional digital camera.

3.7 Pressure Transducers

Plastic tubing then connects the pressure taps along the line to the Honeywell PX2 series pressure transducers. One of the 10 transducers can be seen below in Figure 43. This configuration allowed for 5 transducers to be placed upstream and 5 downstream of the abrupt change and allowed for 25 unique differential pressure measurements to be made.



Figure 43: Honeywell 100 PSIA (690,000 Pa) PX2 series heavy duty pressure transducer

The Honeywell PX2 series are a high performance line of pressure transducers that are marketed as heavy duty. Honeywell states the PX2 will have a minimum life span of 10 million cycles. This will ensure the product has an extremely low probability of wearing out within the life of the experiment and also help ensure the data recorded is accurate and precise. The PX2 also features six sigma design standards which provides extra assurance the product is made properly and without inexpensive and unreliable manufacturing methods. Keeping a consistent set of pressure measurement infrastructure is a key to keeping the variability within experiments

minimized and maintain precise and reliable testing methodology. Having reliable equipment that will have a low probability of failure is one key to our testing infrastructure. Table 2 shown below lists the performance specifications for the Honeywell PX2 pressure transducer.

Table 2: Performance Specifications for the Honeywell PX2 pressure transducer.

Characteristic	Parameter
Operating temperature range ²	-40 °C to 125 °C [-40 °F to 257 °F]
Storage temperature range ³	-40 °C to 125 °C [-40 °F to 257 °F]
Compensated temperature range ⁴	-40 °C to 125 °C [-40 °F to 257 °F]
Overpressure minimum rating ⁵	(See Table 3.)
Burst pressure minimum rating ⁶	(See Table 3.)
Long term stability	±0.5 %FSS ⁹ (1000 hr at 25 °C [77 °F])
Accuracy ⁷	±0.25 %FSS ⁹ (See Figure 1.)
Offset error ⁸	±1 %FSS ⁹
Total Error Band ¹⁰	±2 %FSS ⁹ (-40 °C to 125 °C [-40°F to 257 °F]) (See Figure 1.)
Response time ¹¹	<2 ms
Turn on time ¹²	<7 ms
Life ¹³	min. of 10 million cycles to operating pressure

3.8 Pressure Transducer Calibration

The 10 pressure transducers were then calibrated with a Fluke pressure calibrator by increasing the pressure incrementally from the zero pressure reading all the way to 90% of the total pressure reading capacity. This was done individually for all 10 pressure transducers and allowed the data to be automatically adjusted and recorded using the Keysight data acquisition system. A picture of the Fluke pressure calibrator can be seen below in Figure 44.



Figure 44: Fluke pressure calibrator used to calibrate the Honeywell PX2 pressure transducers.

The Keysight data acquisition system has several key features. It has the ability to capture two data points per second on each channel utilized. The experiment utilized 10 pressure transducers and two thermocouples allowing for 24 data points per second to be measured.

3.9 Data Acquisition

The Keysight system also allowed for quick and easy setup for subsequent testing with the ability to save previous calibration settings. A picture of the data acquisition system can be seen below in Figure 45.



Figure 45: Keysight data acquisition system used in testing.

To summarize the experimental setup, a simple diagram is included in Figure 46 to help understand the process. The flow begins at the pump and flows to the inlet of the test section. The flow temperature is then measured and flows past 10 pressure transducers shown in black. The flow temperature is then measured once again before exiting the test section and then flows back to the pump to complete the cycle. The temperatures and pressures are recorded twice per second and stored on a computer for analysis.

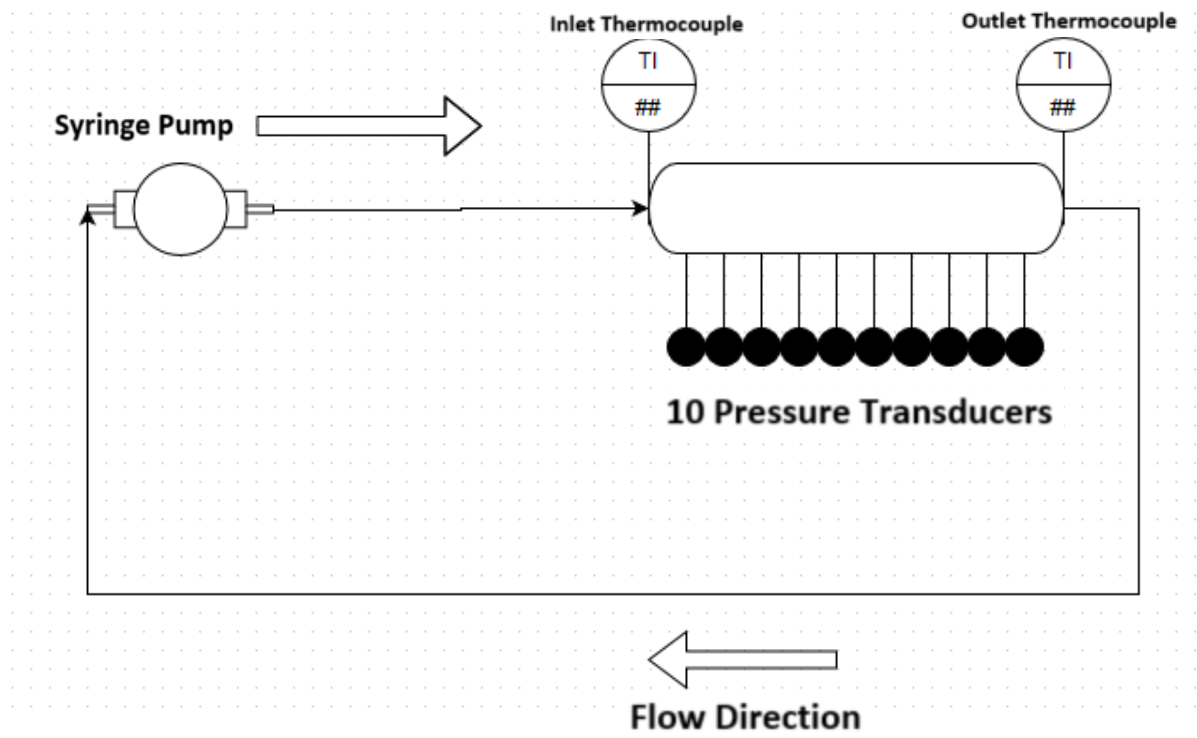


Figure 46: Process flow diagram of the experimental setup.

CHAPTER 4

RESULTS AND DISCUSSION

4.1 Overview

When exploring the results of the miniature channel testing one of the most basic and fundamental results relate to the differential pressure readings. The differential pressure readings are the basis for how a multitude of calculations are made. Calculating how much power, what type of drag is dominant, important coefficients, and many other useful pieces of information would not be possible without differential pressure readings.

4.2 Porous Media Testing

In Figure 47 below, differential pressure is plotted versus volumetric flow rate. Notice how as the flowrate increases, the differential pressure readings also increase. These differential pressure readings were taken from the beginning and end of the channel and include the flow through the whole porous media sample.

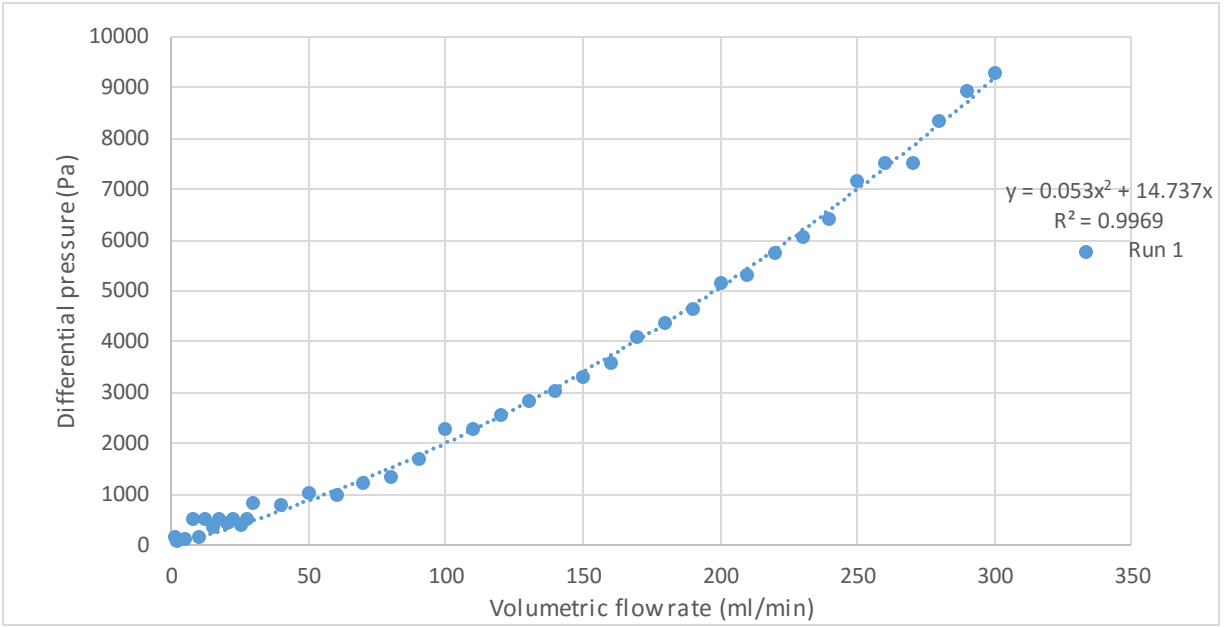


Figure 47: Differential pressure vs volumetric flow rate for independent porous test run #1

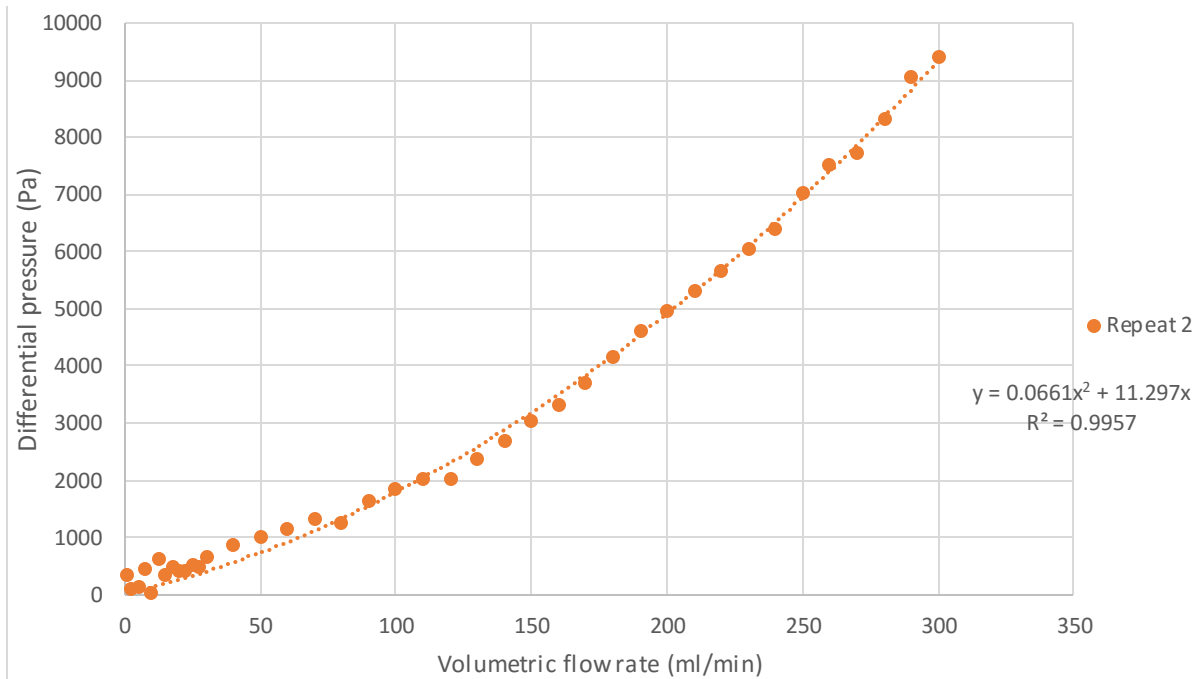


Figure 48: Differential pressure vs volumetric flow rate for independent porous test run #2.

Differential pressure was independently measured a second time for verification reasons. The same sample was used and the pressure transducers were used at the same location upstream and downstream from the sample. The results can be seen in Figure 48. Notice the results from Figure 47 and Figure 48 follow approximately the same trend line and the equations used are extremely similar. This shows the high repeatability of the experiment. Differential pressure was also measured at the reservoirs as discussed in the experimental methods chapter. These pressure readings were used in determining the calculations mentioned throughout the results. In order to produce results with a high repeatability, the raw data was plotted from both the first and second set of runs with an average line plotted on the graph. The differential pressures were then normalized to create a zero datum at zero flow rate to counteract the small amount of static differential pressure present at zero flow rate. These results can be seen in Figure 49 below.

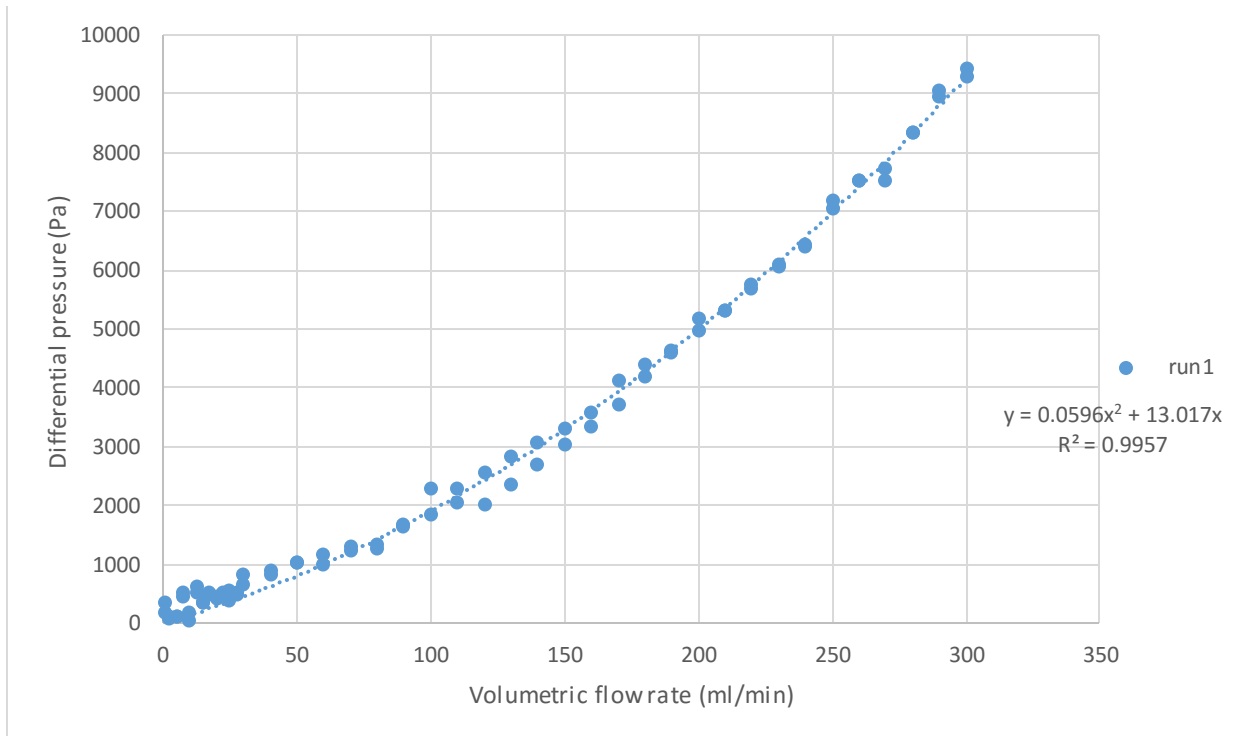


Figure 49: Reservoir differential pressure vs volumetric flow rate using ΔP from runs one and two averaged and plotted with best-fit line.

As shown in Figure 49, the r squared value indicates a strong correlation of the data to the regression line. The equation also indicates the differential pressure growth is a combination of both parabolic and linear equations. This will be discussed in more detail later in the results section.

4.3 Porous Media Differential Pressure by Location

As previously stated, it can be observed the differential pressure growth can be seen in Figure 47, Figure 48, and Figure 49. To highlight this growth further, Figure 50 and Figure 51 below show the local differential pressure of four sections on the flow path. The pressure was measured on two independent test runs of flow rates at 1, 150, and 300 ml/min. The graphs clearly indicate the local differential pressure is growing quickly and further highlights the nonlinearity of the differential pressure growth. Notice the repeatability of the experiment and the y-axis spacing between 1 and 150 ml/min is smaller than the y-axis spacing between 150 and 300 ml/min.

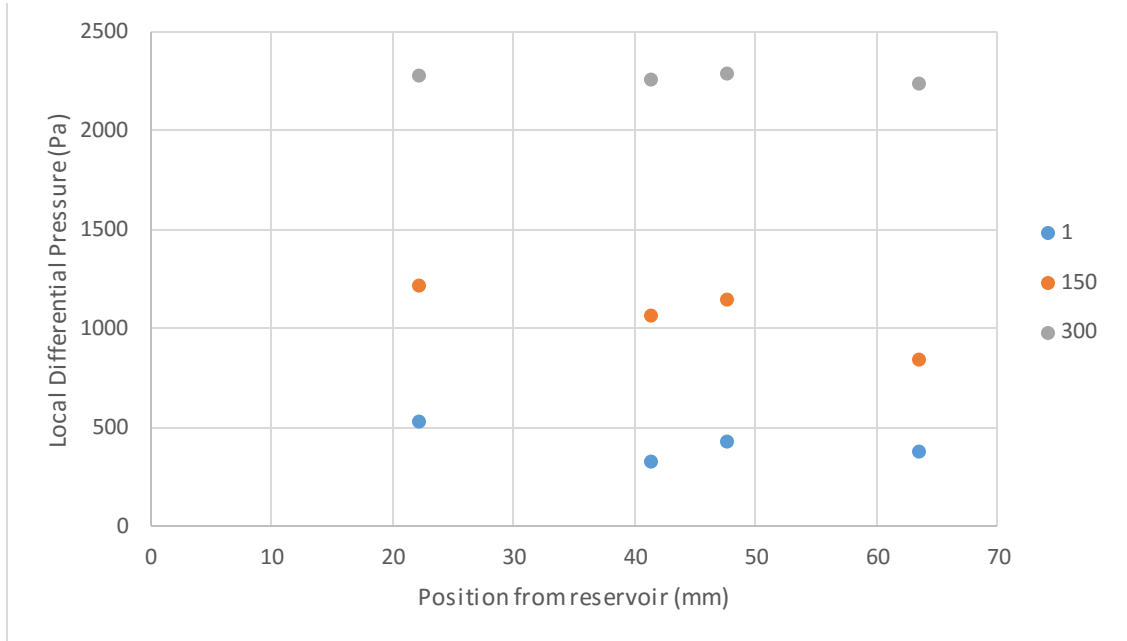


Figure 50: Test run #1 of local differential pressure vs position from the inlet reservoir showing repeatability and non-linear DP growth.

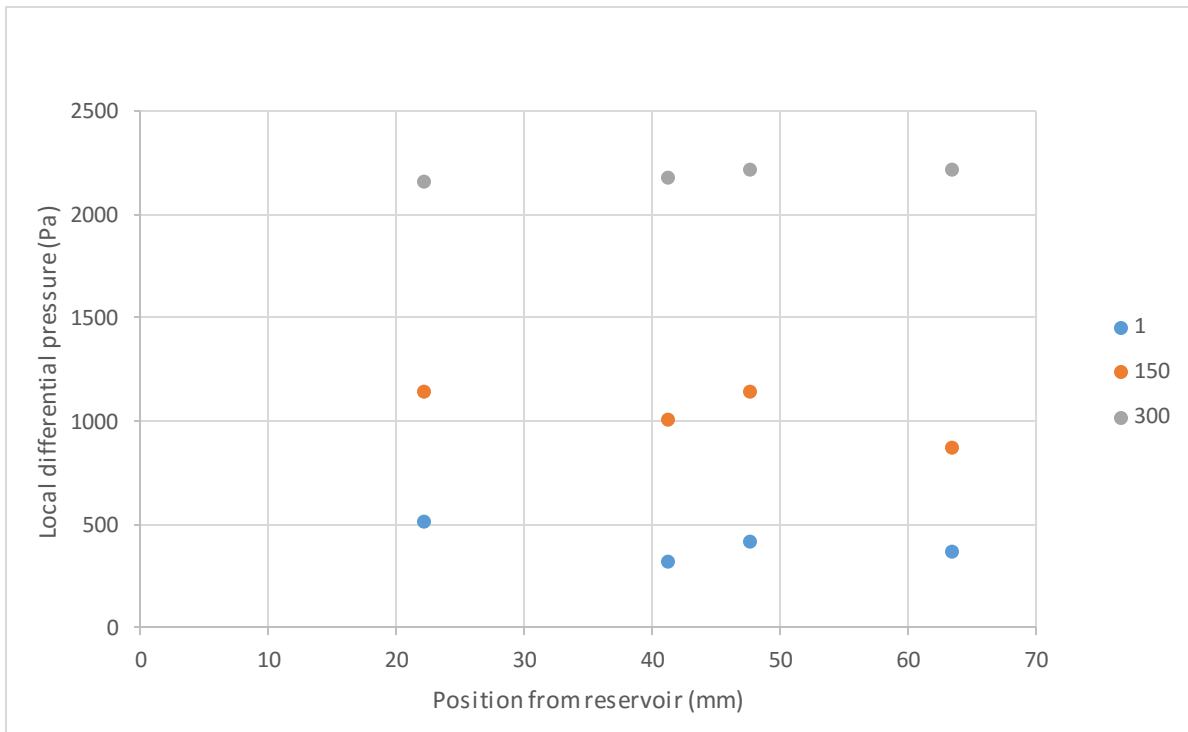


Figure 51: Test run #2 of local differential pressure vs position from the inlet reservoir showing repeatability and non-linear DP growth..

4.4 Form and Viscous Drag

Now that the differential pressure flow curves have been established for flow through the sample of porous material provided by Dr. Gupta of the University of North Dakota, further analysis of these results can be presented. According to Narasimhan (2013), in the book, “Essentials of Heat and Fluid Flow in Porous Media,” there are a variety of ways to model flow through porous media. Narasimhan (2013) begins by discussing Darcy’s Law which models flow through porous media by relating differential pressure, length of the flow passage, viscosity of the fluid, permeability of the media, and velocity of the fluid. He goes on to explain the Darcy model only incorporates a linear equation to explain differential pressure and based on the experimental data shown in the previous figures this is not highly accurate. Darcy’s Law can be seen below in Equation 4.4.1 (Narasimhan, 2013):

$$\Delta P/L = (\mu/K) U, \quad (4.4.1)$$

To create a model that reflects the parabolic nature of the differential pressure growth, Narasimhan discusses the Hazen-Dupuit-Darcy model. This model includes a velocity squared term along with density of the fluid and a C coefficient that describes the form factor of the porous media. This coefficient will vary based on the physical form of the media, even if the material properties are kept the same. The Hazen-Dupuit-Darcy model can be seen below in Equation 4.4.2 (Narasimhan, 2013).

$$\Delta P/L = (\mu/K)*U + C*\rho*U^2, \quad (4.4.2)$$

Narasimhan went on to discuss an experimental procedure to evaluate the differential pressure using a gravity-fed system. The experimental procedure outlined in the previous chapter discusses the setup for obtaining differential pressure in great detail. He also displayed the

results from previous work to obtain the permeability and form coefficients of K and C respectively. His plot showing three different porous materials and the graph to obtain the coefficients can be seen below in Figure 52.

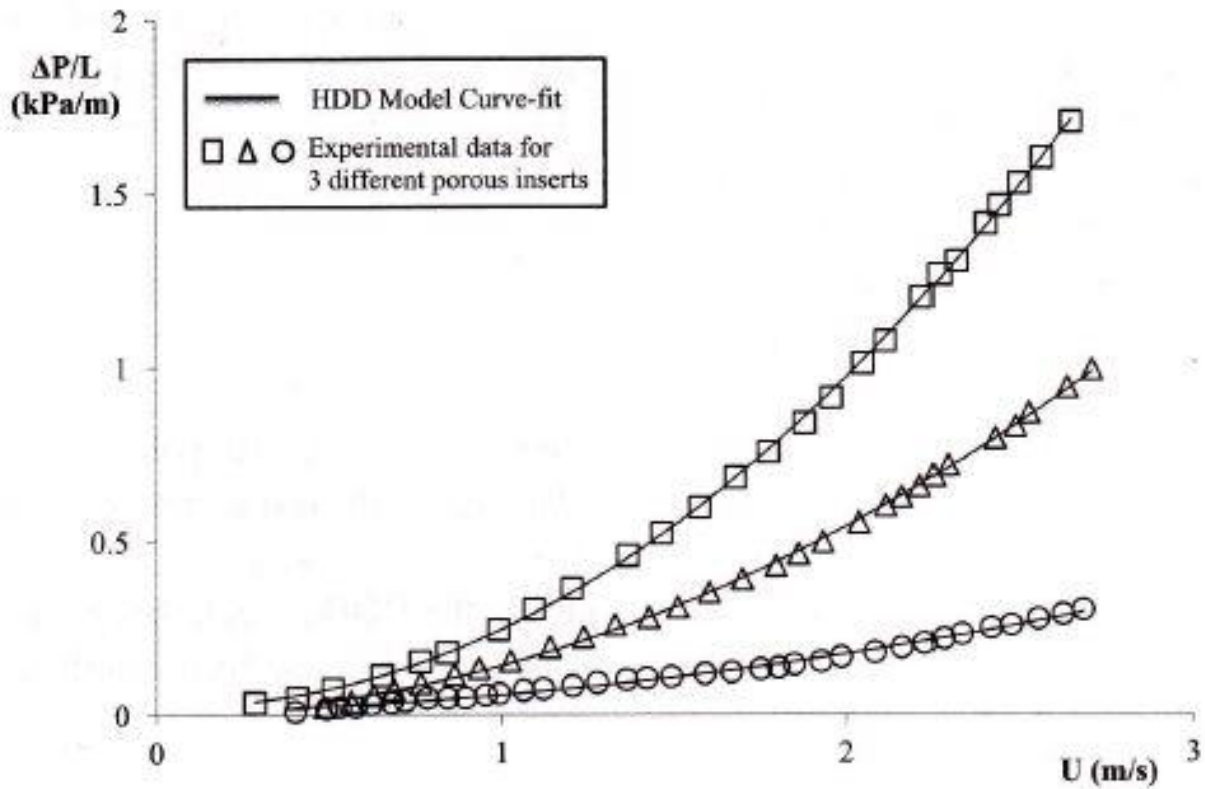


Figure 52: Chart showing usage of HDD model to determine K and C coefficients using: $\Delta P/L = (\mu/K)*U + C*\rho*U^2$ (Narasimhan, 2013).

Using the data obtained experimentally in Figure 49, a similar series of charts were formulated to determine the permeability and form coefficients needed to predict flow through the porous media. To show repeatability, two independent sets of data were used and can be seen graphically in Figure 53 and Figure 54 below.

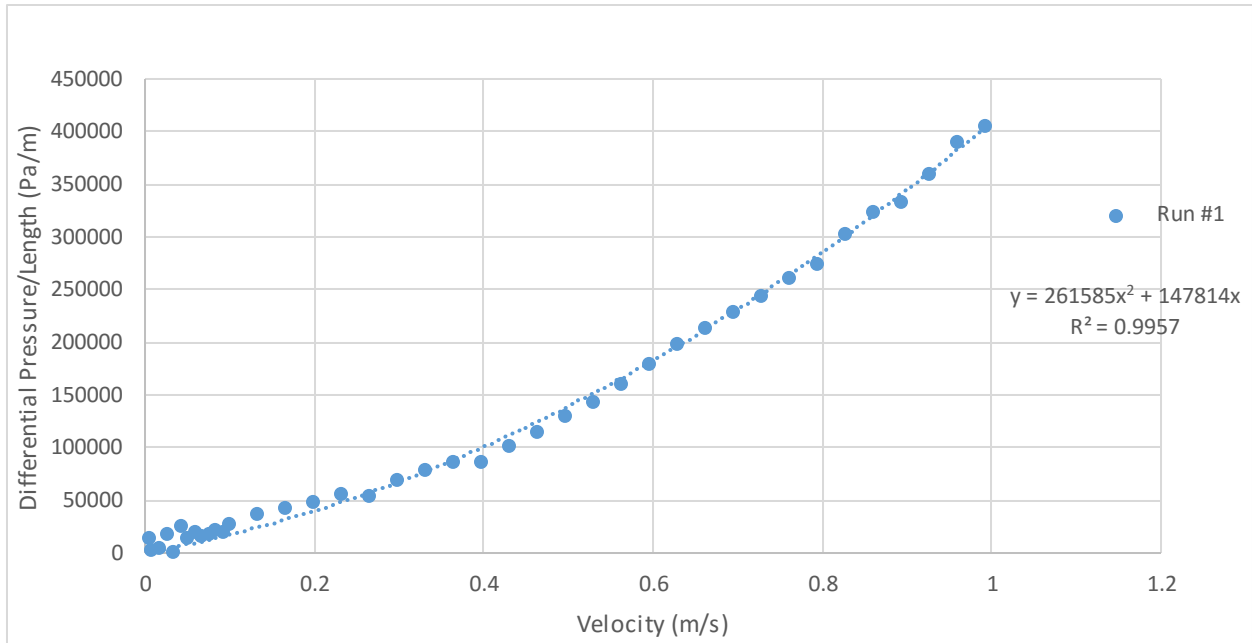


Figure 53: First independent data set showing differential pressure/length vs velocity to determine permeability and form coefficients using $\Delta P/L = (\mu/K)*U + C*\rho*U^2$.

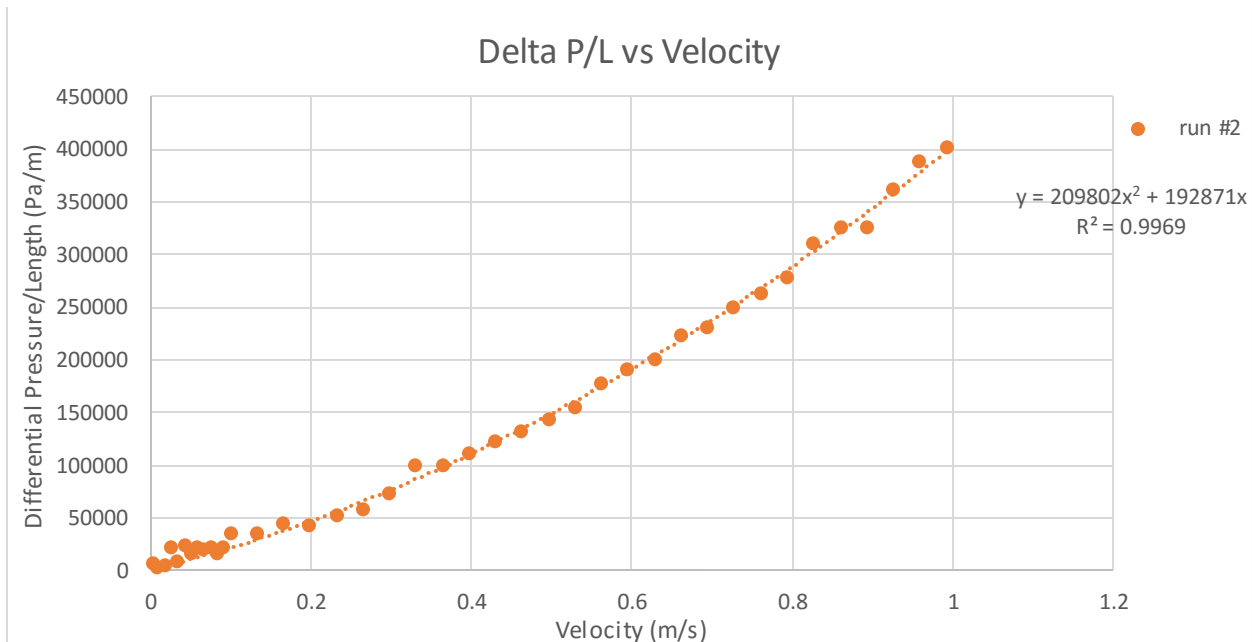


Figure 54: Second independent data set showing differential pressure/length vs velocity to determine permeability and form coefficients using $\Delta P/L = (\mu/K)*U + C*\rho*U^2$.

The data was then compiled and a best-fit line was created using the two independent data sets. This can be seen below in Figure 55.

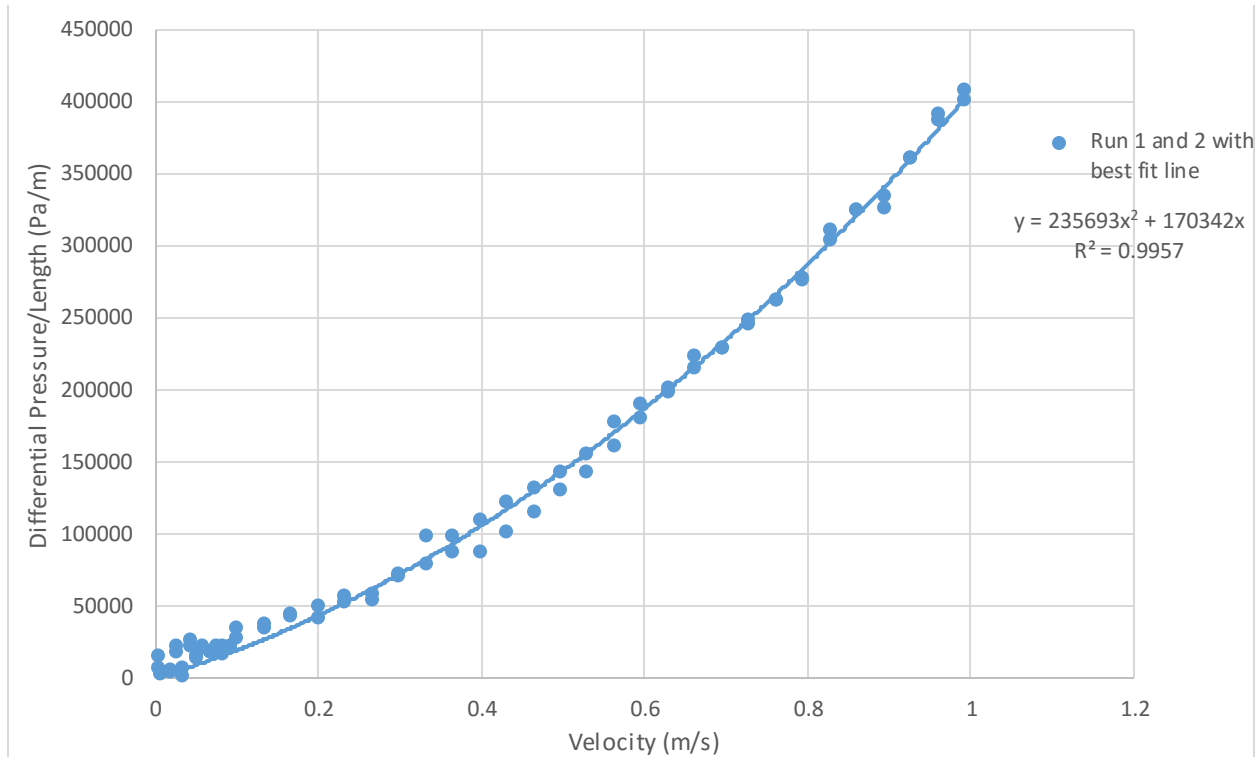


Figure 55: Best-fit line created using two independent sets of data for finding permeability and form coefficients using $\Delta P/L = (\mu/K)*U + C*\rho*U^2$

Using the equation generated in Figure 55 and the properties of water during our experiment, the permeability coefficient was calculated to be $5.28 \times 10^{-9} \text{ m}^2$. The form coefficient was solved using the same procedure and was found to be 236 m^{-1} .

4.5 Reynolds Number Calculations

Reynolds number is a highly used parameter in traditional fluid flow applications. It can be used in determining a transition from laminar to turbulent flow for a variety of internal and external

flow applications. A Reynolds number consists of a velocity, characteristic length, and viscosity. Typically, the onset of turbulence begins at a Reynolds number equal to 2,300 for internal flow applications. Full turbulence does not set in until a 10,000. Narasimhan suggests using a modified version for porous media to determine when flow is transitioning from viscous based drag to form based drag (Narasimhan, 2013). One modified Reynolds number based on permeability allows this calculation to be made based on using the square root of permeability for the characteristic length. This can be seen below in Equation 4.5.1.

$$Re_k = U \rho K^{0.5} / \mu \quad (4.5.1)$$

Based on experimental data produced by (Ward, 1964) and other researchers, the conclusion that transition began when the modified Reynolds number is of the order of 10 (Narasimhan, 2013). Using experimental data, a Reynolds number versus flow rate chart was created and can be seen below in Figure 56.

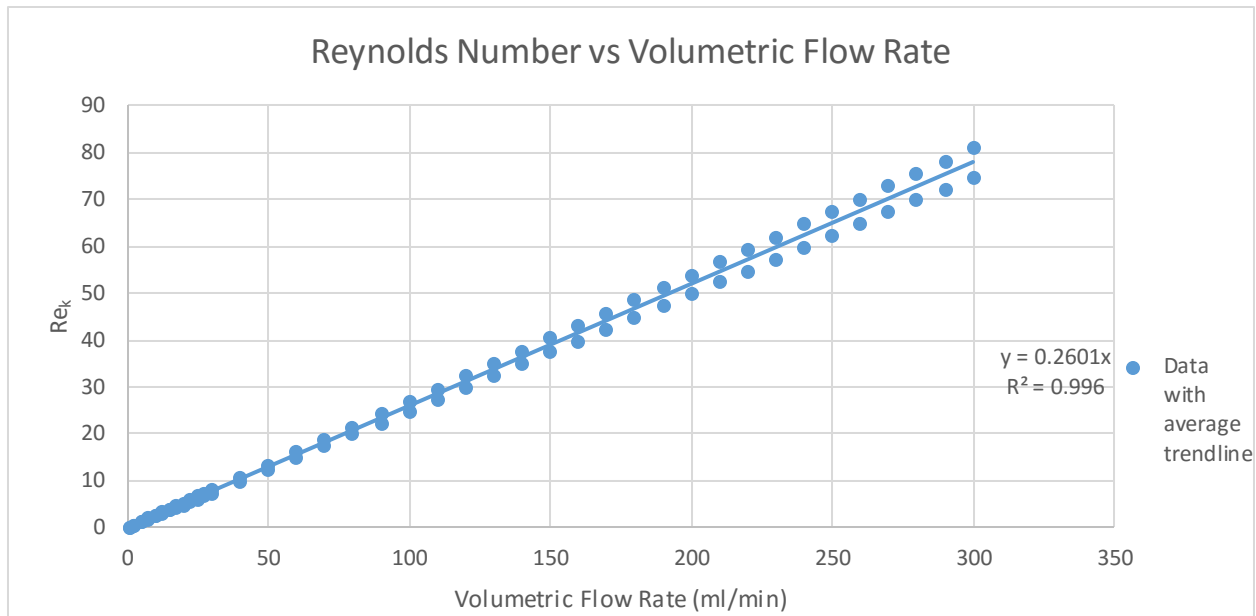


Figure 56: Reynolds number based on permeability vs volumetric flow rate using $Re_k = U \rho K^{0.5}/\mu$.

This Reynolds number did not include the coefficient for form drag, so using this model will not accurately represent the transition. As previously discussed, determining the coefficients of permeability and form are critical to correctly modeling the flow (Narasimhan, 2013).

Narasimhan discussed a key parameter to determining if the flow is dominated by viscous or form drag. This key parameter is represented as lambda. This is a Reynolds number created using both K and C coefficients. It is a linear correlation involving the permeability coefficient, form coefficient, viscosity of the liquid used, velocity of the liquid used and density of the liquid used. This equation can be seen below in Equation 4.5.2 (Narasimhan, 2013).

$$\lambda = (\rho * C_0 * K_0 / \mu_0) * U \quad (4.5.2)$$

4.6 Determining Dominant Drag

The key to understanding Equation 4.5.2 is determining if λ is less than or greater than one. When the flow is at a relatively low velocity, the flow will be dominated by viscous drag and can be modeled with relative accuracy and precision with the Darcy flow equation. At this relatively low velocity, λ will be much less than one. When the velocity of the fluid is increased, λ will eventually equal one. At this point, viscous and form drag are then equivalent and will have the same proportion of drag on the flow. Once λ increases past 1, the flow is then dominated by form drag. This ultimately means as the flow velocity increases, the differential pressure versus velocity curve will become more parabolic and less linear. As the flow velocity and volumetric flow rate decrease, the curve will become more linear and less parabolic. This effect can be seen in the previous figures representing the observed data. As previously noted, λ increases linearly. This can be seen below in Figure 57.

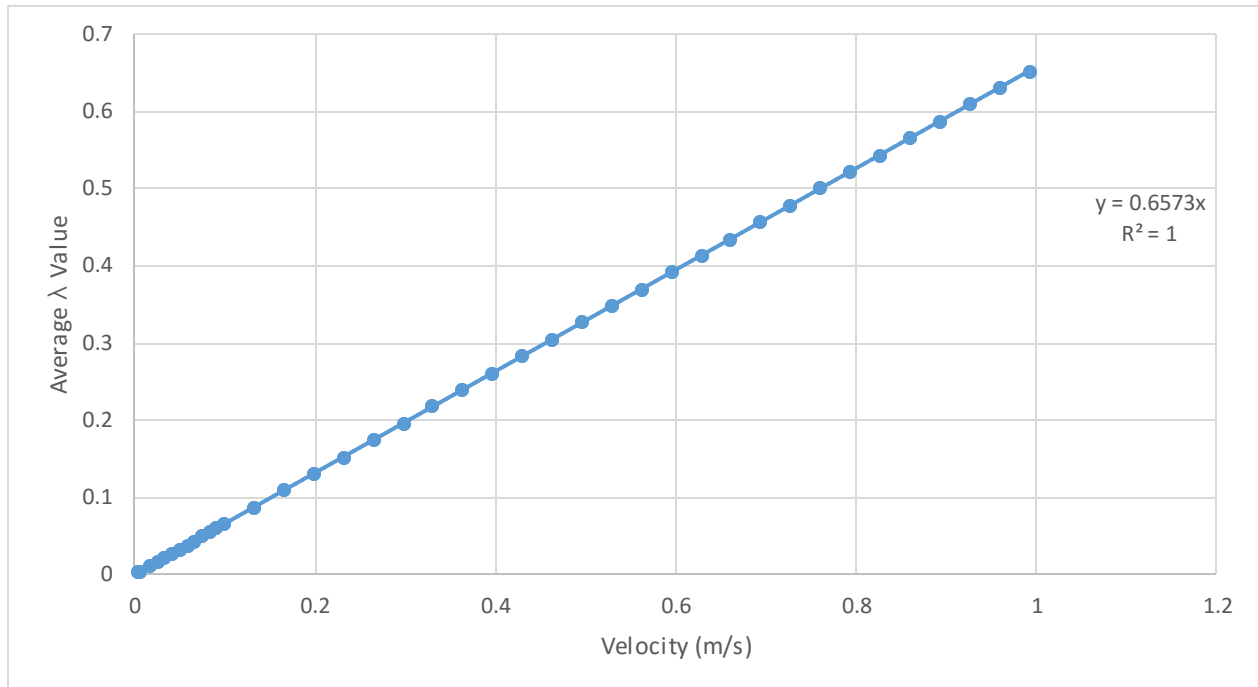


Figure 57: λ vs velocity with averaged trend line from all data points of first and second runs using $\lambda = (\rho \cdot C_0 \cdot K_0 / \mu_0) \cdot U$.

Figure 57 clearly shows the lambda value using the experimental results never reaches above 1.0. The highest point lambda reaches on the trend line average is 0.66. This indicates the flow is still viscous dominated. This also shows the flow differential pressure growth is more linear based than parabolic. This is reflected in the experimental data shown above in the previous figures. By visually inspecting the differential pressure versus volumetric flow rate and differential pressure/length versus flow velocity, the flow curve is clearly more linear than parabolic. This is especially true at lower velocities and volumetric flow rates, but still ultimately valid at the highest rates completed in this experiment. In order to discover the exact percentage the form and viscous drag are each contributing to the flow, the following chart provided by Narasimhan in Figure 58 allows the calculated lambda value to be correlated to the respective percentage of form and viscous drag.

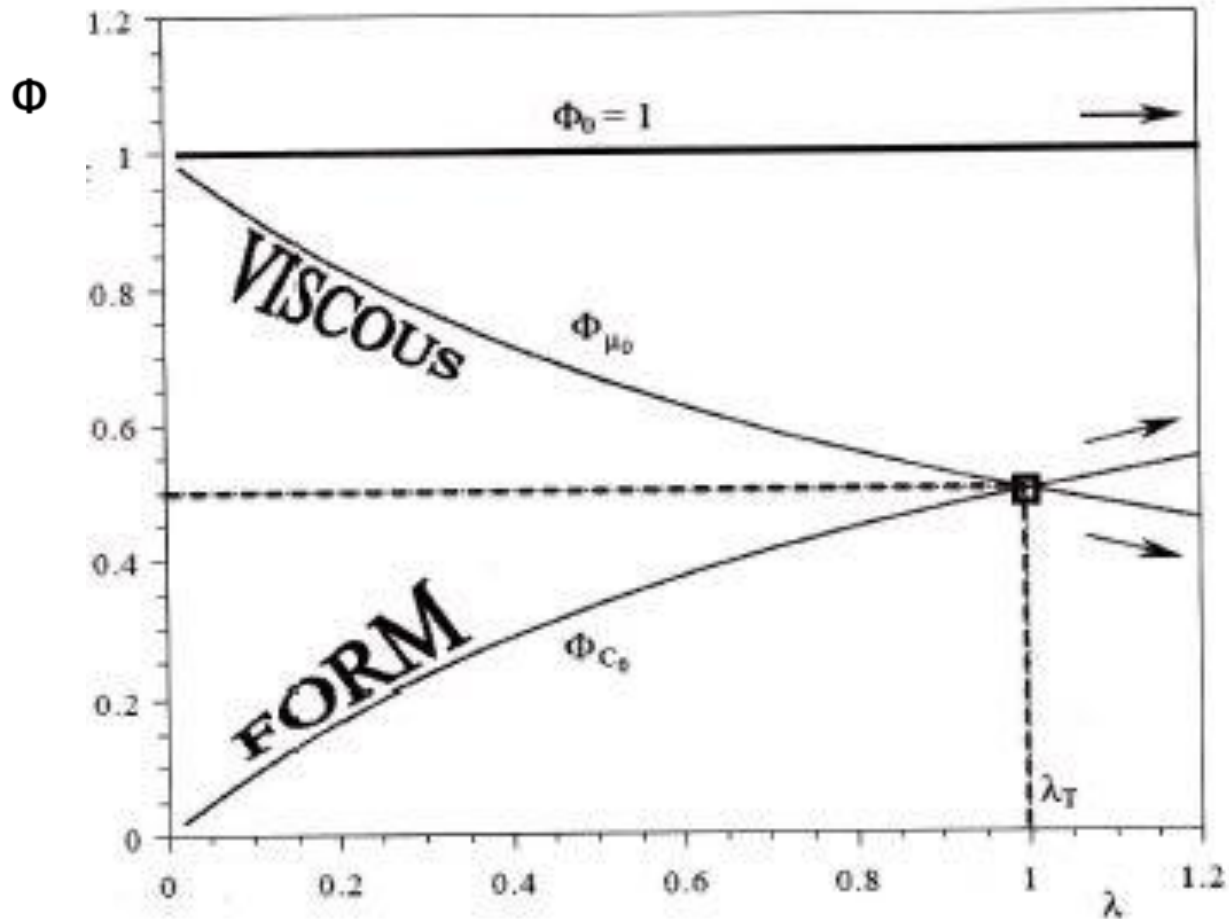


Figure 58: Viscous and form drag contributions vs lambda (Narasimhan, 2013)

Using Figure 57 and Figure 58 together, the drag contributions of form and viscous drag can be determined quite easily. When the flow velocity is below 0.2 m/s, the lambda value is less than 0.1, and using the chart in Figure 58, it can be determined over 90% of the drag is caused by viscous effects and less than 10% of the drag is caused by form drag. When the flow velocity is at 0.5 m/s, lambda is 0.35. Again, using Figure 58 shows viscous drag is responsible for 75% of the total drag and form is responsible for 25%. Finally, at 1 m/s lambda is 0.65 and correlates to

40% form drag and 60% viscous drag. Understanding if form or viscous effects are ultimately causing the drag can help design engineers produce more efficient designs of products involving fluid flow through porous media. Due to our limitations on pumping volumetric flowrate capacity, the velocity could not be increased to exceed an average λ value of 0.65. The results for the coefficients and equations are however valid for flows above the tested flow regime. In order to achieve a 50% balance of viscous and form drag the fluid velocity would need to be increased to 1.55 m/s. This could easily be achieved with a pump providing a higher volumetric flow rate capacity. To reach 1.55 m/s, the volumetric flow rate would have to be equal to 466 ml/min which is 166 ml/min or 55% higher than the maximum of the syringe pump used in the experiment.

4.7 Energy and Power Usage

Now that the drag dominance has been established, another key parameter in porous media flow can be discussed. The power needed to produce a specific flow rate through a porous media sample can be calculated using differential pressure and volumetric flow rate. This is extremely important for sizing pumps and determining the amount of energy that will be consumed by a process over a period of time. Since power is energy divided by time, simply multiplying the power by the time the process was completed will provide the amount of energy consumed. Below in Figure 59 is a graph of power versus flow rate for flow through the titanium dioxide porous media using two independent test runs. The trend line shows the average of all the compiled data. Notice the high correlation of the data to the trend line.

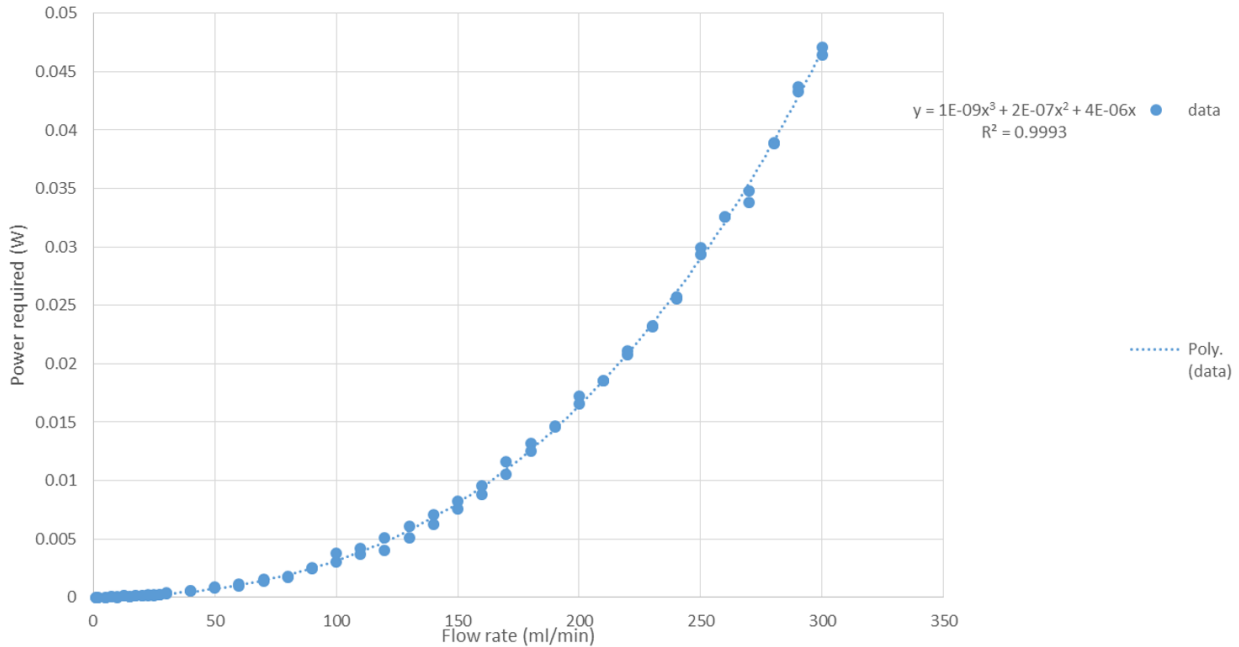


Figure 59: Power required vs volumetric flow rate through titanium dioxide porous media using Power (W) = ΔP * Volumetric flow rate

The power required is a function of volumetric flow rate to the cubed exponent. The power required increases much faster as a function of velocity than differential pressure, because as discussed previously, differential pressure grows with a velocity squared function. Since the higher flow rates require much more power, the total amount of fluid that can be pumped through the porous material with a fixed amount of energy is much lower at the higher flow rates. This also means the lower flow rates can pump much more fluid with a fixed amount of energy. Many applications involving performance in space are severely limited based on a fixed amount of energy. If an application involving flow through the porous media test sample had only 1000 Joules of energy to utilize, at 1 ml/min the total fluid pumped would be 3,967,309 ml. Using the same 1000 Joules of energy pumping at 300 ml/min would only allow for 108,225 mL to be pumped. Pumping at 1 ml/min would allow for 36.65 times more fluid to be pumped than

300 ml/min. This is a direct result of the power required to pump the fluid growing with the cube. Figure 60 below shows this effect with a chart of ml pumped with 1000 Joules versus flow rate.

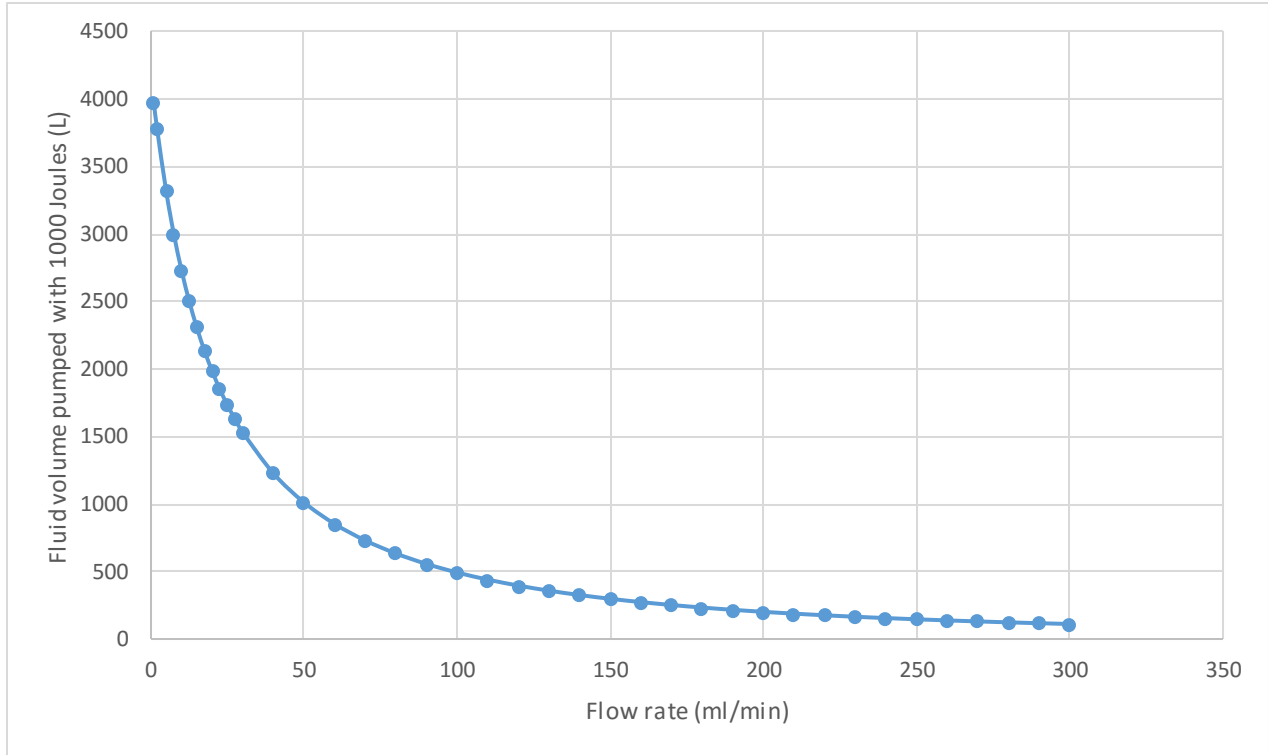


Figure 60: Volume of water in ml pumped with 1000 Joules vs flow rate (ml/min) through the titanium dioxide porous media using Energy = Power * time.

Using this information gained can provide some insights into optimizing the pumping efficiency. Since flowrates increase linearly with time and power required versus flowrate increases with the cube, it can be said that minimizing the flowrate is the best way to maximize total fluid pumped per unit of energy.

4.8 Square Non-Porous Channel Expansion and Contraction Flow

Studying flow through expanding and contracting channels is a much easier to model than flow through porous channels because of the relative simplicity and predictability of the geometry. Porous media on a micro level has a great deal of random passages making the fluid flowing through it change directions with a degree of uncertainty. On a macro level, the unpredictability of these passages can be negated by studying the overall effect of the flow through the sample as long as the overall properties of the samples are consistent. With a simple expansion or contraction, modeling the macro effects are quite similar to porous media. They both have a reduction in cross-sectional area available in the channel for the fluid to flow. They both allow for a differential pressure measurement to be made at individual flow rates. They both also have a transitioning effect based on a Reynolds number calculation. Using the exact same experimental setup as the porous media except for changing out the porous sample with a square channel expansion and contraction with an expansion ratio of 4/1, a comparison can be made between the two test sections.

4.9 Expansion Theoretical Differential Pressure

Using the expansion flow direction detailed in the experimental methods section, a theoretical differential pressure can be calculated. The theoretical differential pressure is based on the area ratio, density of the fluid, and velocity of the fluid. The equation to solve this differential pressure can be seen below in Equation 4.9.1 (Kays and London).

$$\Delta P_e = (A_1/A_2) * (1 - (A_1/A_2)) * \rho * V^2 \quad (4.9.1)$$

Using Equation 4.9.1 and the experimental data obtained through methods explained in the experimental methods section, a graph showing theoretical differential pressure versus

experimental data obtained through several independent test runs was produced. This graph can be seen below in Figure 61.

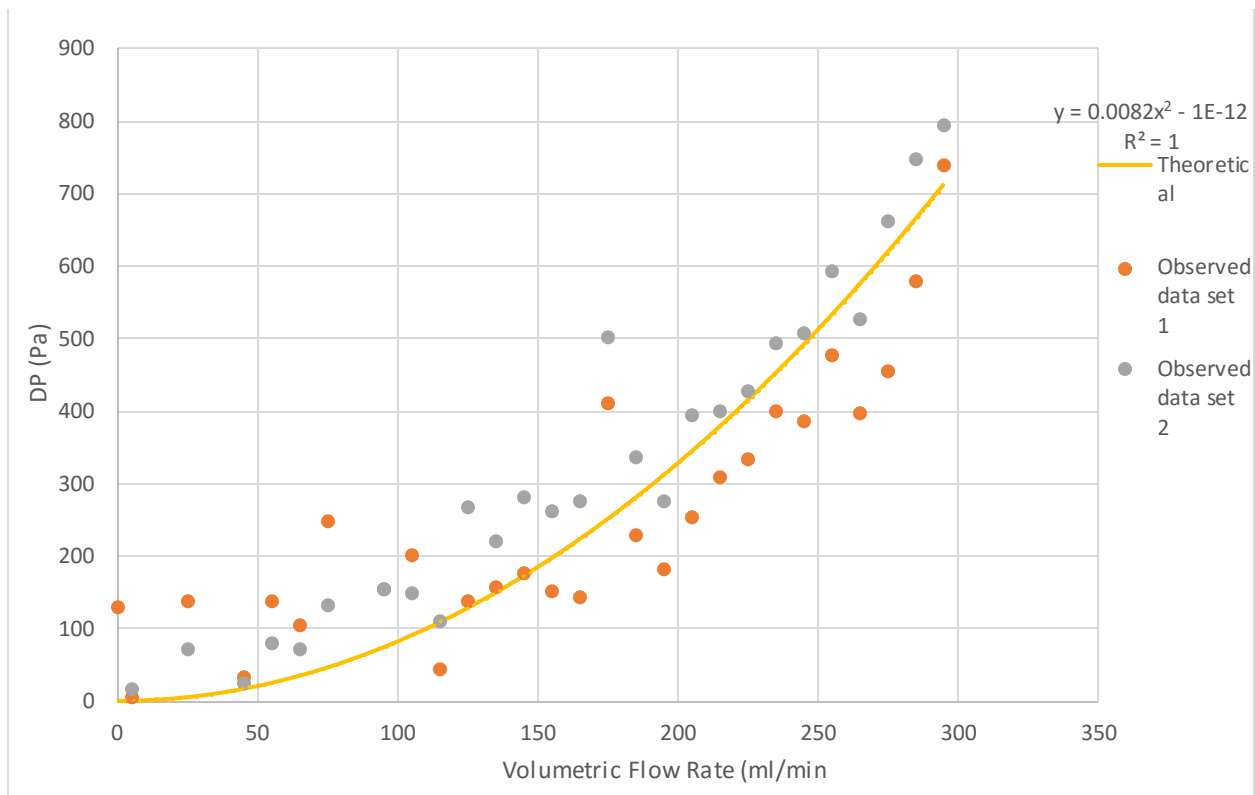


Figure 61: 4/1 area ratio rapid expansion theoretical trend line using $\Delta P_e = (A_1/A_2) * (1 - (A_1/A_2)) * \rho * V^2$ and experimental data for differential pressure vs volumetric flow rate.

4.10 Expansion Flow Required Power

It is important to note that differential pressure grows with a squared function just as the function did with the porous media even though it is a single channel and it is an expansion and not a

contraction. Power required to move a liquid or fluid through an expansion can also be modeled. Equation 4.10.1 below clearly shows how differential pressure and volumetric flow rate can be multiplied to obtain the power required to move fluid through a contraction or expansion.

$$\text{Power (W)} = \Delta P * \text{Volumetric flow rate} \quad (4.10.1)$$

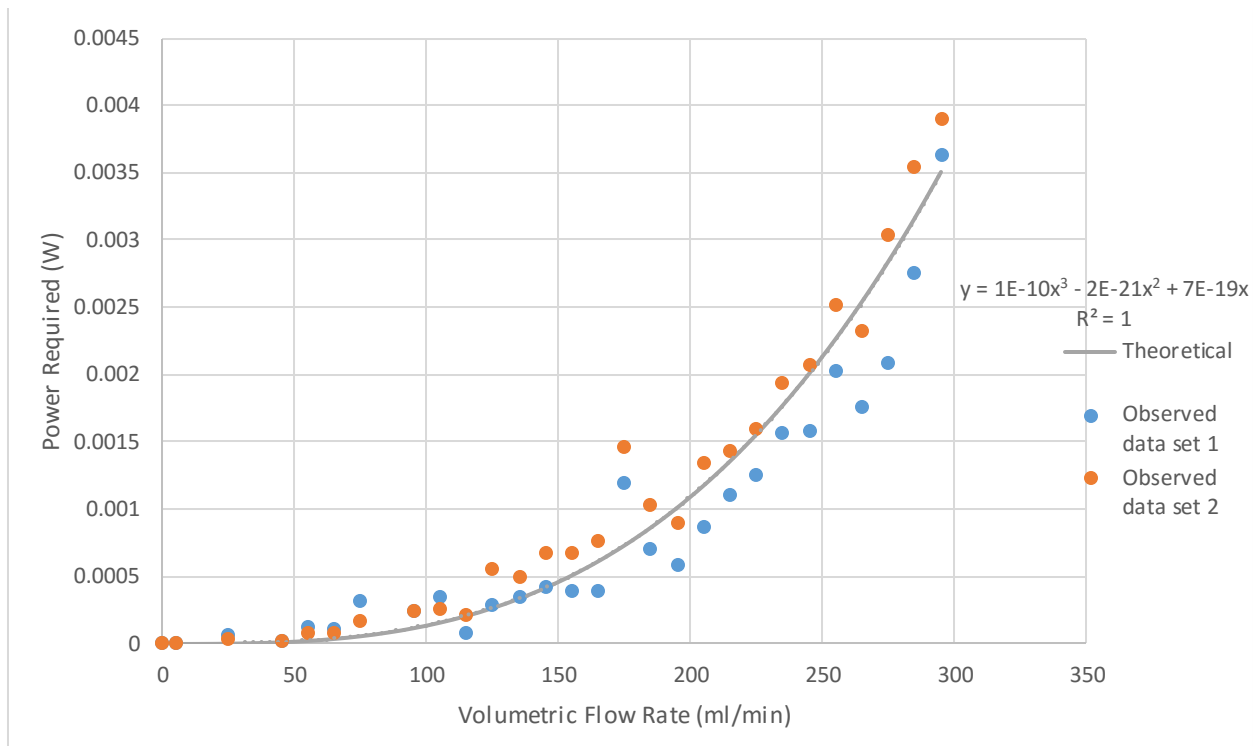


Figure 62: Expansion power required (W) vs volumetric flow rate (ml/min) for a 4/1 area ratio expansion with theoretical power required trend-line using Power (W) = $\Delta P * \text{Volumetric flow rate}$ and $\Delta P_e = (A_1/A_2)*(1- (A_1/A_2))*\rho*V^2$.

A theoretical power requirement can be calculated using the theoretical differential pressure shown in Equation 4.8.1 and multiplied by the volumetric flow rate. The theoretical line can be seen above in Figure 62 and is a solid blue. The orange and grey data points are experimental data taken from location just before and after the expansion. As you can see above, the data

follows the theoretical curve relatively well. Comparing the results of the power required for expansion in a square channel and power required for contraction through the porous media, there is a difference of about 8.5 times more power required for the porous media contraction than the non-porous expansion testing.

4.11 Total Fluid Moved with 1000 Joules

Total fluid moved with a set amount of energy can also be modeled for flow through a rapid expansion. The total amount of fluid moved with 1000 Joules of energy at different flowrates can be seen in Figure 63. This clearly shows the importance of using as slow of a flowrate as possible to maximize the total volume of fluid moved.

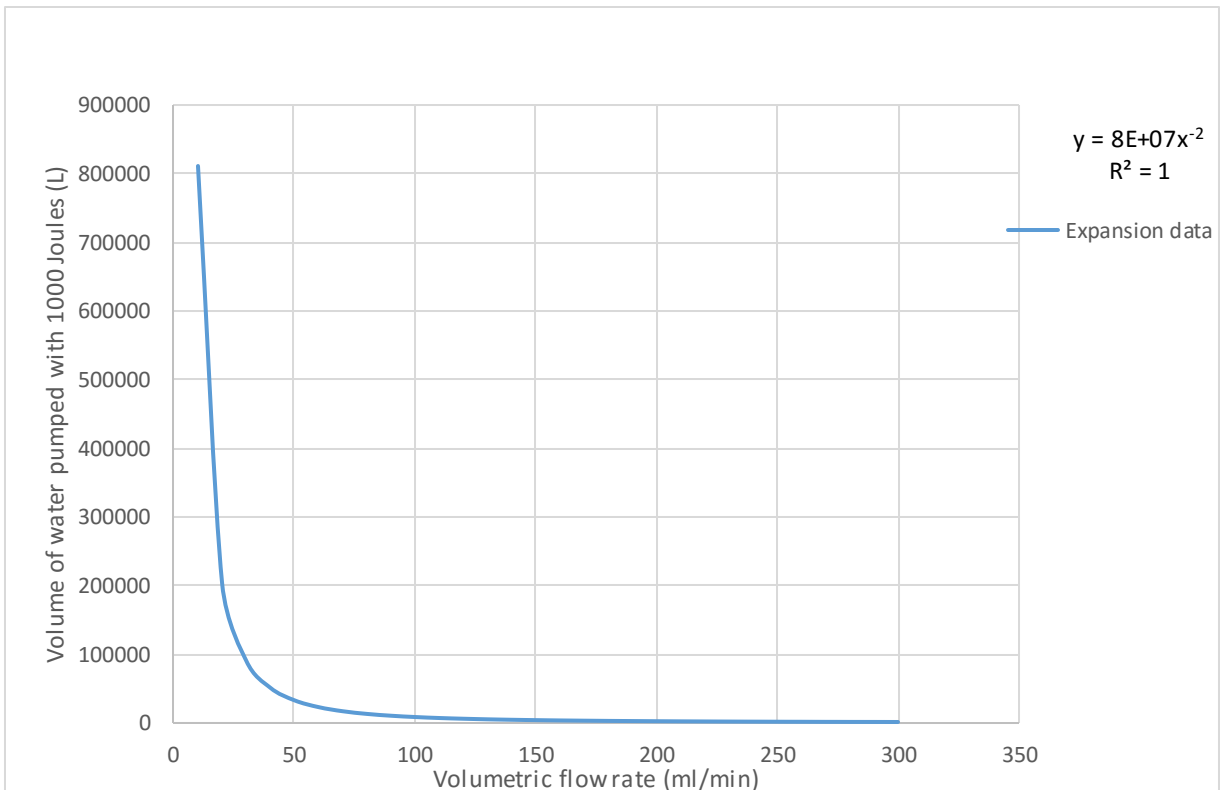


Figure 63: Total Liters of water moved with 1000 Joules of energy through a 4/1 area ratio rapid expansion using Energy = (P)*(t) vs volumetric flow rate (ml/min).

4.12 Square Channel Diameter

Traditionally, internal flow Reynolds numbers are calculated using a velocity, diameter, and viscosity. The diameter is assumed to be calculated for a round pipe, so adjustments must be made for the square and rectangular channels in the expansion test section. To create a usable diameter, Equation 4.12.1 is used below.

$$D = 4 \cdot A / P \quad (4.12.1)$$

The area is the cross sectional area and the perimeter used is the wetted perimeter. When using a square channel, the diameter used will be the length of any side of the square. A calculation must be made when using a rectangular channel because using either the short or long side will yield incorrect results. The correct Reynolds number equation needed for internal flow can be seen below in Equation 4.12.2.

$$Re = \rho \cdot V \cdot D / \mu \quad (4.12.2)$$

4.13 Determining Laminar and Turbulent Flow

A crucial determination of whether the flow is laminar or turbulent must be made from the Reynolds number calculation. In a traditional channel with no abrupt changes, the flow is fully laminar from Reynolds numbers of 0 to 2300. When it increases from 2300 to 10000 it is partially turbulent with some areas of the flow becoming turbulent and falling back to laminar states. Once the flow is above 10000, it is considered fully turbulent. When using a channel with an abrupt change in area and in the intermittent zone of Reynolds numbers between 2300 and 10000, it can be tricky to model the flow correctly. Using the traditional Reynolds number

equation for both the small and large channel area will yield different results. Below in Figure 64, the large area of the flow is considered. The Reynolds number is shown versus the volumetric flow rate. Notice this is a linear correlation.

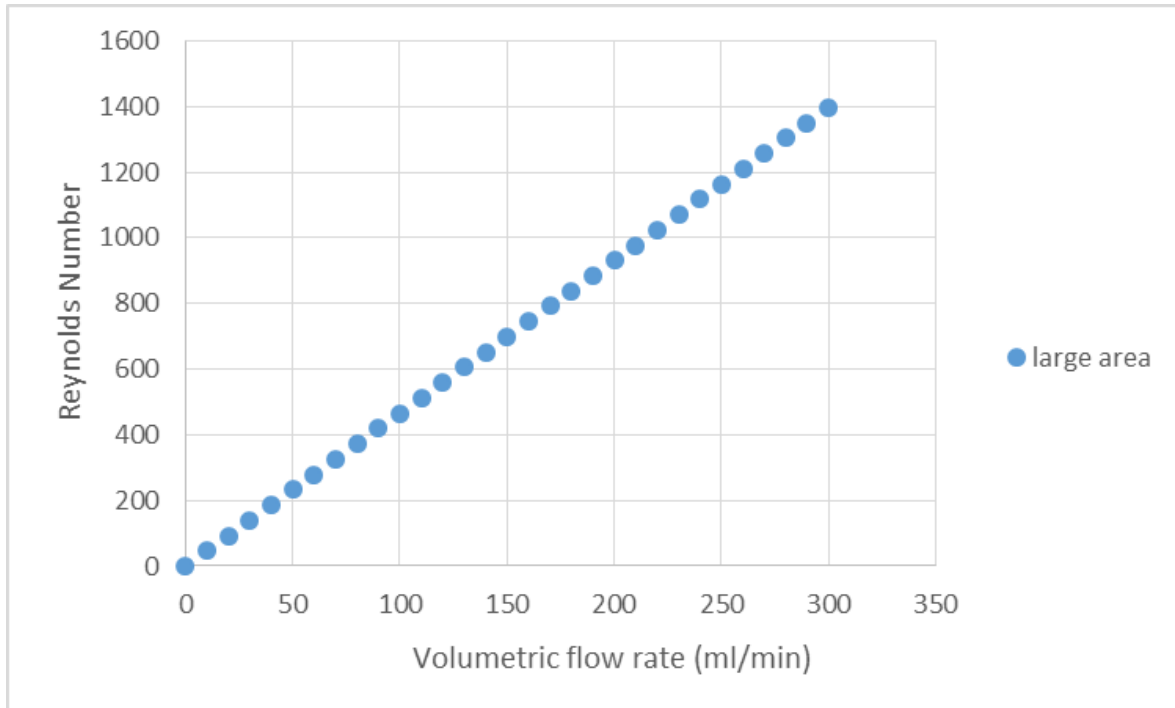


Figure 64: Reynolds number using $Re = \rho \cdot V \cdot D / \mu$ vs volumetric flow rate for the large area of the expansion channel.

The Reynolds number for the small square section is also considered below in Figure 65. Notice how it is much higher than the large area because of the higher velocity needed to maintain the same volumetric flow rate. The correlation between Reynolds number and volumetric flow rate is still linear.

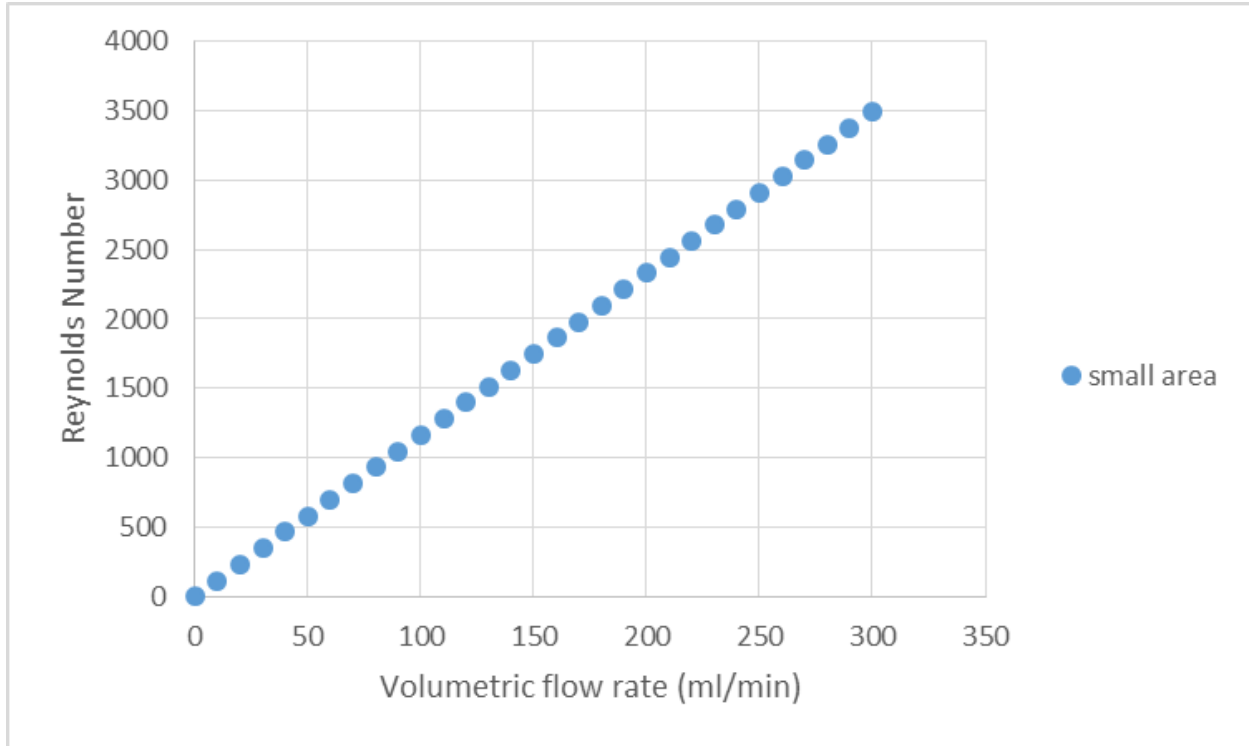


Figure 65: Reynolds number using $Re = \rho \cdot V \cdot D / \mu$ Volumetric flow rate for the smaller square cross sectional area expansion channel

4.14 Contraction Theoretical Differential Pressure

As explained in the experimental setup chapter of the thesis, the expansion test section was reversed to form a contraction test section. Just as we were able to model the theoretical differential pressure with the expansion, we can also use a different equation to model the contraction. It can be seen in Equation 4.14.1.

$$\Delta P = (0.5\rho V^2/g_c)[(1-\sigma^2)+K_c] \quad (4.14.1)$$

The contraction ratio of $1/4$ is used to represent sigma and K_c is represented by a constant shown in Figure 66.

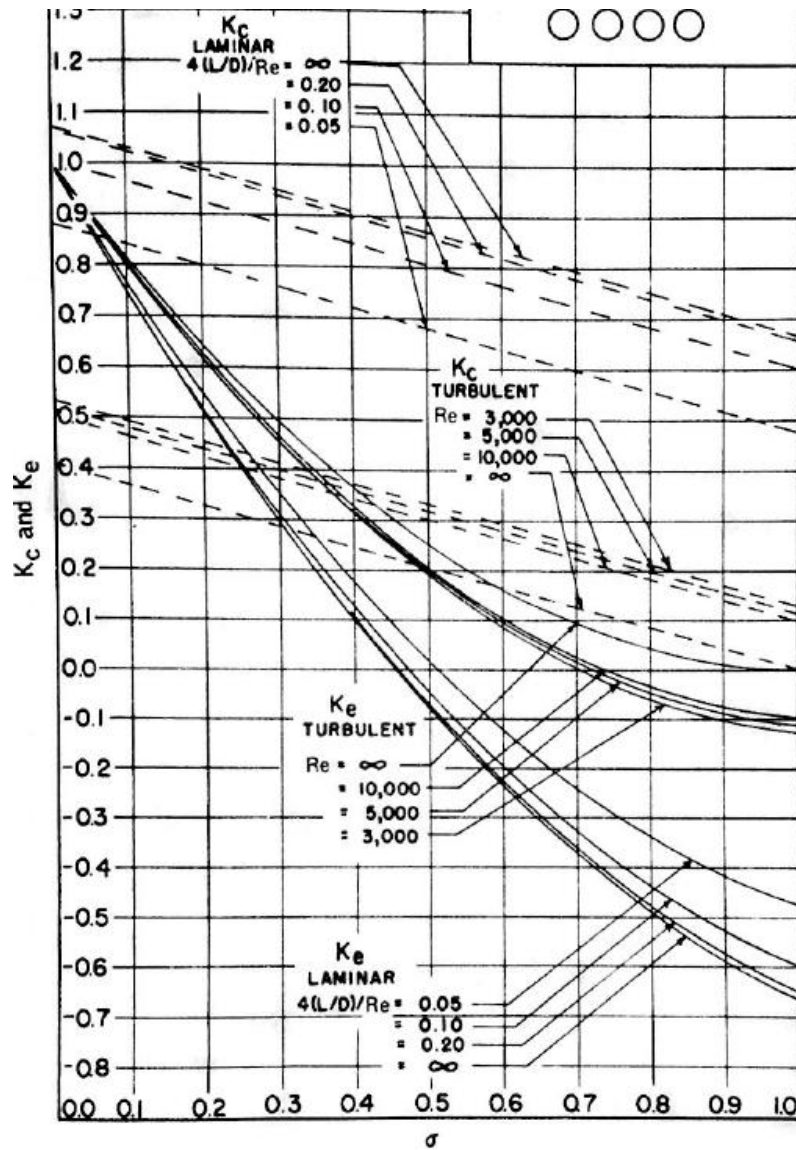


Figure 66: Chart showing correction coefficients (K_c) for turbulent and laminar flows using contraction and expansions.

4.15 Selecting K_c

Selecting the proper K_c has a large effect on the calculation shown in Equation 4.14.1. As seen in Figure 66, there are many possibilities for the coefficient. Modeling the flow as laminar or turbulent will have a significant impact on the accuracy of the differential pressure prediction.

To determine if the flow is laminar or turbulent, the Reynolds number calculations used for the expansion must again be used for contraction. The results can be seen in Figure 67 and Figure 68 below.

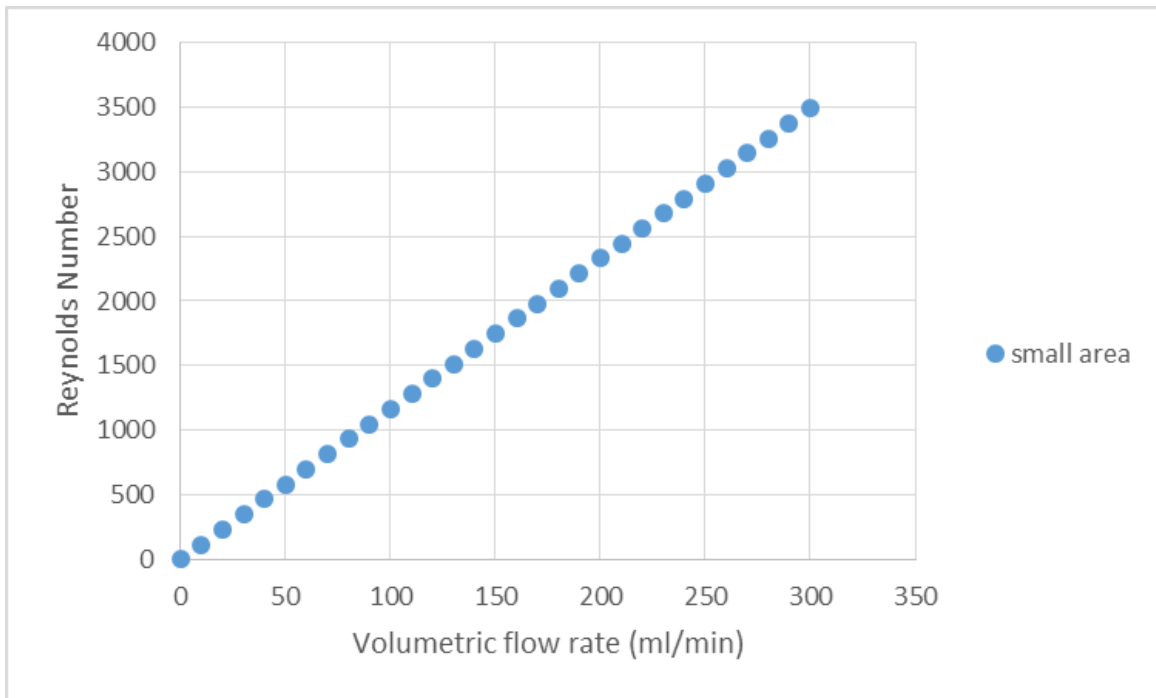


Figure 67: 1/4 area ratio contraction Reynolds number using $Re = \rho * V * D / \mu$ vs volumetric flow rate for the small area of the channel.

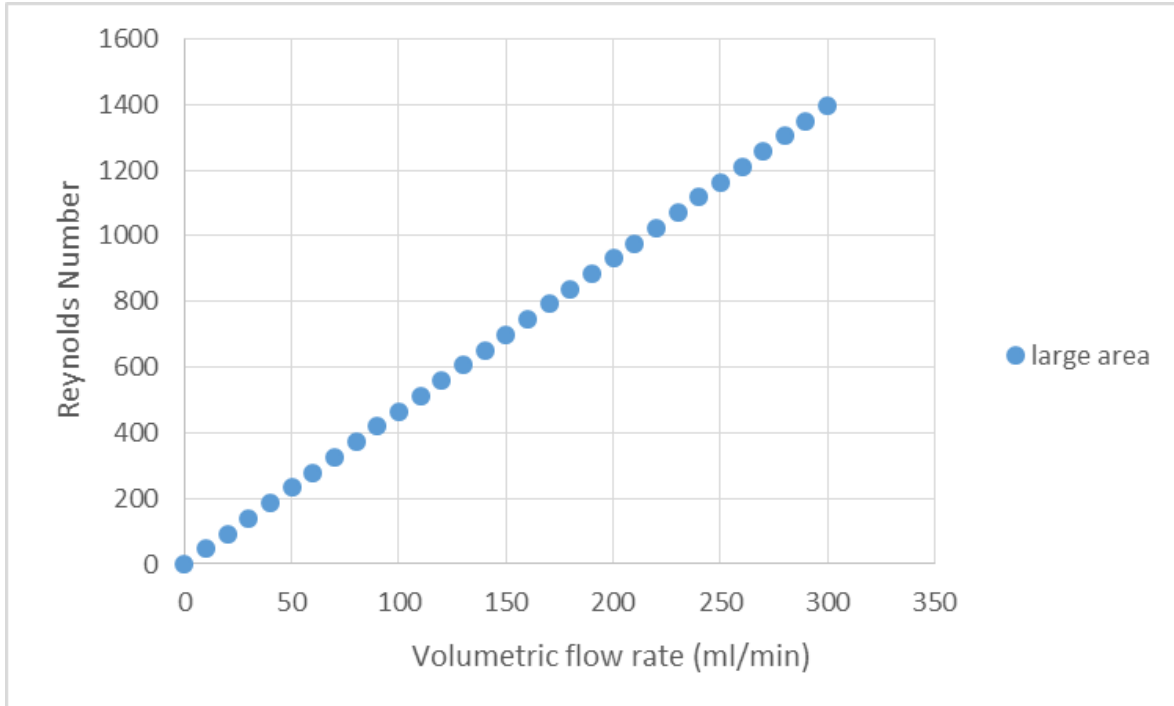


Figure 68: $\frac{1}{4}$ area ratio contraction Reynolds number using $Re = \rho \cdot V \cdot D / \mu$ vs volumetric flow rate for the large area of the channel.

4.16 Contraction Theoretical Differential Pressure Modeling

Notice how the Reynolds numbers for both the expansion and contraction did not change because the exact same volumetric flow rates were used for both experiments. Another important realization to make is the large area Reynolds number never reaches the onset of turbulence threshold of 2300, but the small area easily surpasses 2300 and increases all the way to 3500 at the volumetric flow rate of 300 ml/min. This further complicates matters because making a selection of laminar or turbulent will affect the results significantly. When using the chart in Figure 66, the K_c for laminar flow is dependent on the calculation of $4(L/D)/Re$. The calculation yields 0.07 meaning at a sigma of 0.25, the K_c should be calculated at around 0.78. If

turbulent flow is assumed, the K_c should be calculated around 0.43. This is not exact because the coefficient depends on the Reynolds number that fluctuates depending on the flow rate selected.

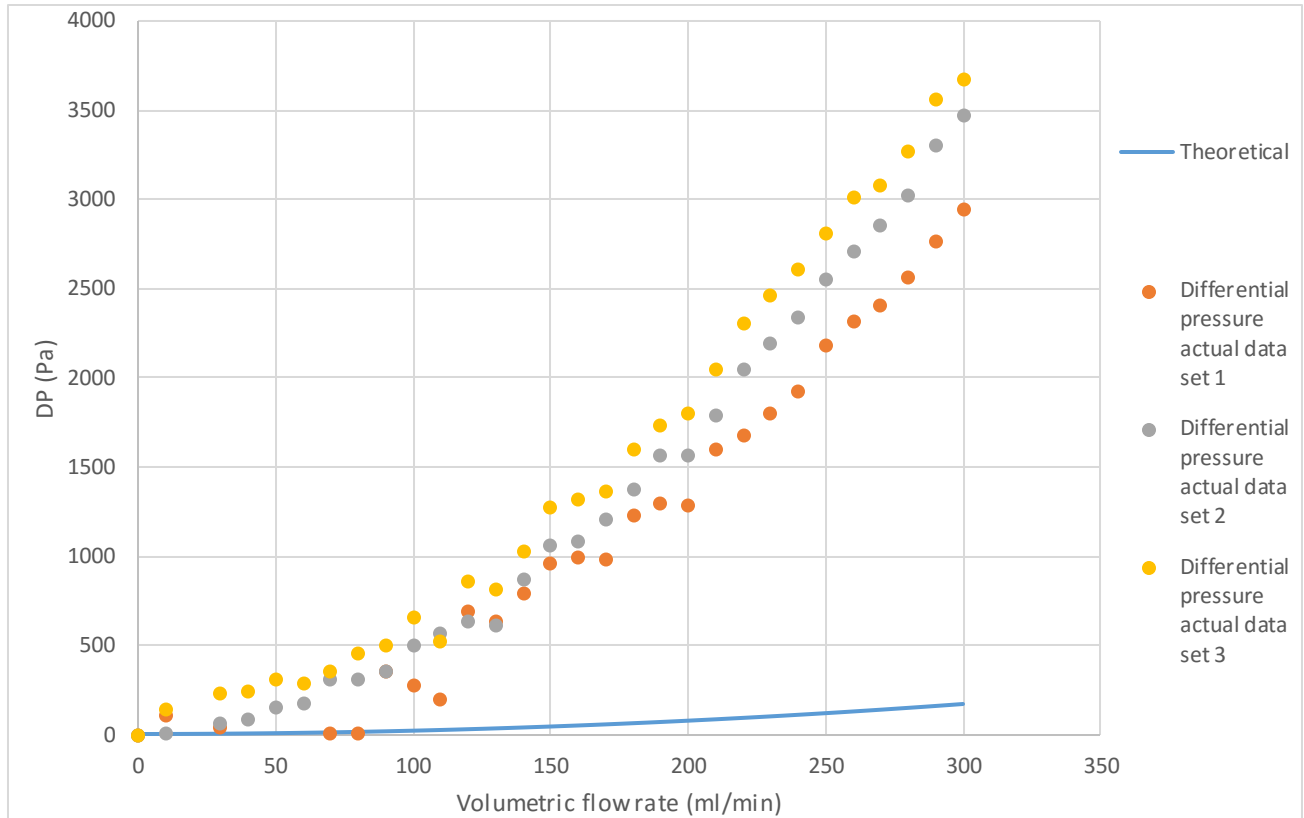


Figure 69: Contraction theoretical differential pressure using large area velocity, turbulent $K_c=0.4$ assumption, and $\Delta P_c = (0.5\rho V^2/g_c)[(1-\sigma^2)+K_c]$ vs volumetric flow rate plotted with experimental data

Above in Figure 69 theoretical differential pressure is plotted using the slower velocity from the large cross sectional area of the channel before the contraction. The K_c is also assumed to be turbulent. These assumptions are obviously incorrect because the data does not correlate well with the predicted differential pressure. These assumptions are most likely the worst to make as well because traditionally the fastest velocity in the channel is selected and the Reynolds number never reaches the onset of turbulence in the wide area of the channel.

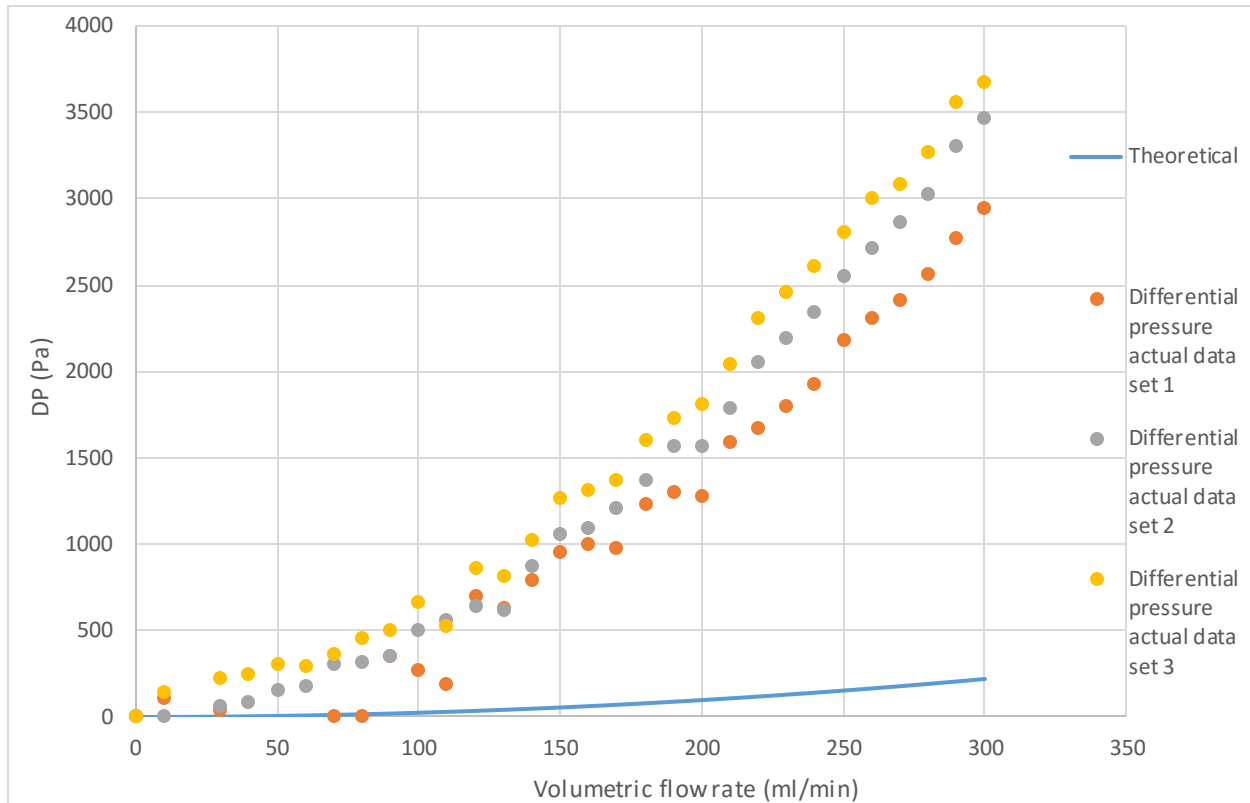


Figure 70: Contraction theoretical differential pressure using large area velocity, laminar $K_c=0.78$ assumption, and $\Delta P_c = (0.5\rho V^2/g_c)[(1-\sigma^2)+K_c]$ vs volumetric flow rate plotted with experimental data

Above in Figure 70 is a plot of the theoretical differential pressure plotted with a blue line. This pressure was calculated using the velocity in the wide part of the channel with a slower velocity than the narrow channel. As stated before, this assumption is probably incorrect and is reflected in the data. This differential pressure was also assumed to be laminar. This did improve the reliability of the calculation versus the turbulent assumption seen in Figure 69, but not a huge improvement.

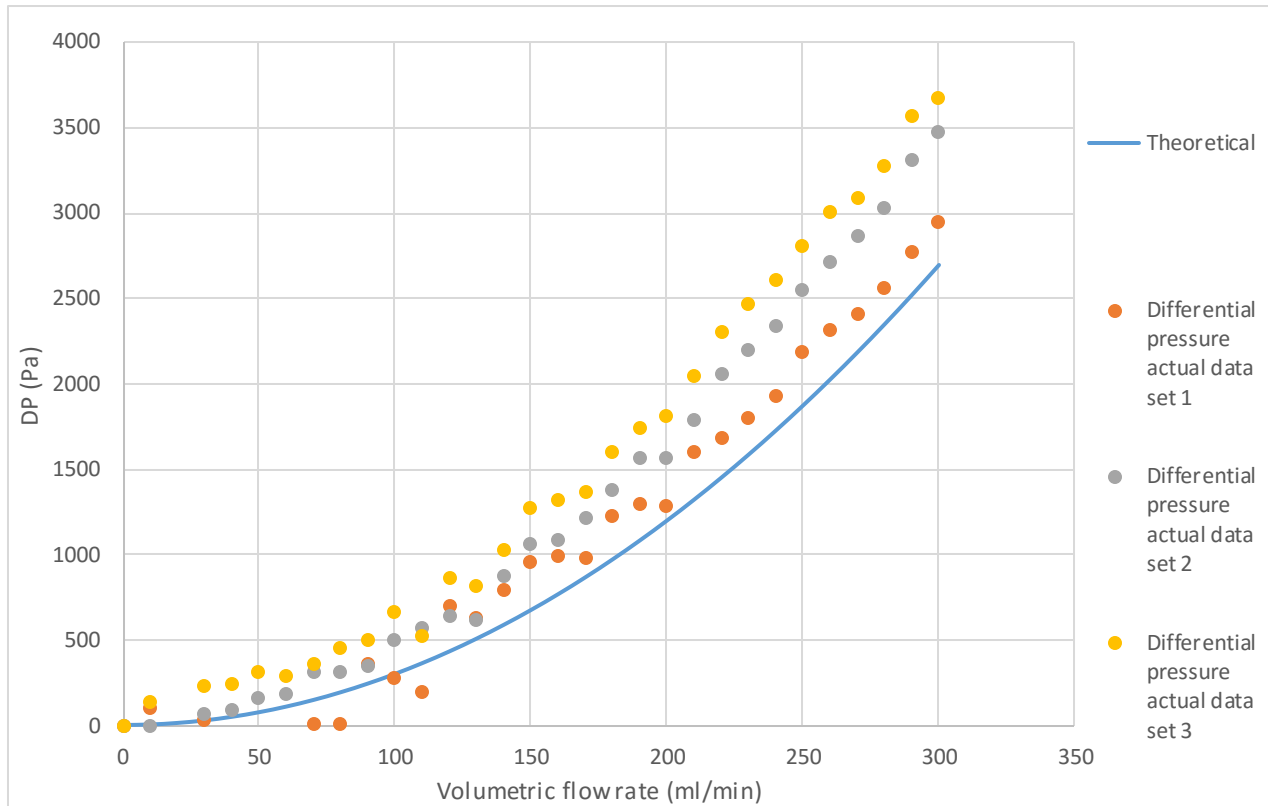


Figure 71: Contraction theoretical differential pressure using small area velocity, turbulent $K_c=0.4$ assumption, and $\Delta P_c = (0.5\rho V^2/g_c)[(1-\sigma^2)+K_c]$ vs volumetric flow rate plotted with experimental data.

Above in Figure 71 is a theoretical plot of differential pressure created using the velocity in the contraction portion of the test section and a turbulent K_c . As clearly shown in the data, this is a much better estimate of the test data acquired for the experiment. It is under predicting the pressure slightly, but is still a substantial improvement of the representation of data.

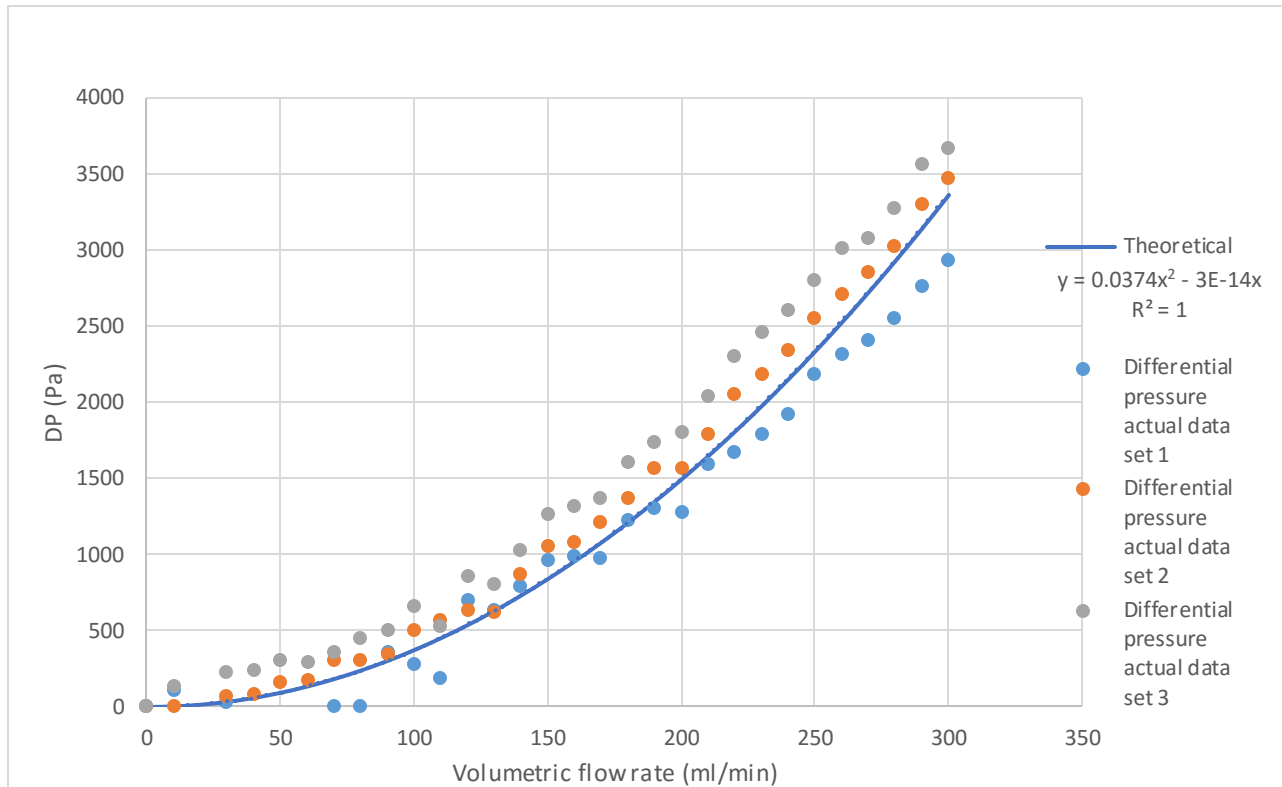


Figure 72: Contraction theoretical differential pressure using small area velocity, laminar $K_c=0.78$ assumption, and $\Delta P_c = (0.5\rho V^2/g_c)[(1-\sigma^2)+K_c]$ vs volumetric flow rate plotted with experimental data.

The blue line as shown above in Figure 72, the theoretical differential pressure for the contraction test section using the velocity in the smaller channel cross sectional area and laminar K_c provides the best estimate for predicting the experimental differential pressure measured before and after the contraction. To summarize the findings of the differential pressure testing for the contraction orientation, the main component to correctly predicting the theoretical differential pressure is selecting the highest velocity within the channel. Determining if the flow is laminar or turbulent will have a major effect on the results, but both will provide a decent rough estimate. Using a similar experimental setup with the onset of turbulence only in the contraction portion of the test section and Reynolds numbers never exceeding 3500, the best

prediction of differential pressure will come from using a laminar K_c and the velocity in the contraction portion of the test section with Equation 4.14.1.

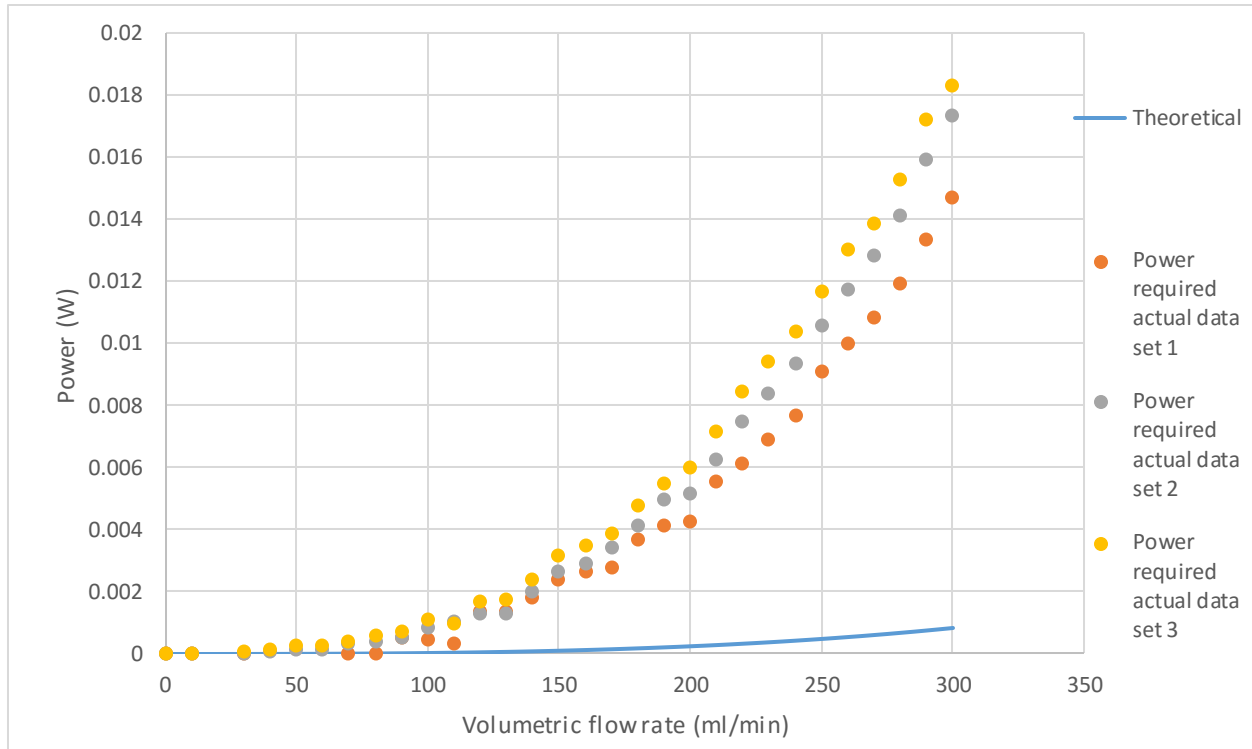


Figure 73: Contraction theoretical power required (W) using large area velocity, turbulent $K_c=0.4$ assumption, $\Delta P_c = (0.5\rho V^2/g_c)[(1-\sigma^2)+K_c]$, and $\delta E/\delta t = \text{Volumetric flow rate} * \Delta P$ vs volumetric flow rate plotted with experimental data.

4.17 Contraction Theoretical Power Modeling

Theoretical power needed to move the fluid through a contraction test section can also be modeled with the differential pressure data. The theoretical power can also be predicted using Equation 4.14.1 and substituting the results into Equation 4.10.1 previously listed. Just as the theoretical differential pressure had four different outcomes using two different turbulence and velocity profiles, the power needed also can be modeled with both. The predicted power outcomes are quite similar to the predicted differential pressures. The main difference is the

power needed grows with the cube and the differential pressure grows with the square. Above in Figure 73, it is clearly seen the lower velocity and turbulent assumptions are incorrect. These assumptions again provide the worst prediction of power needed.

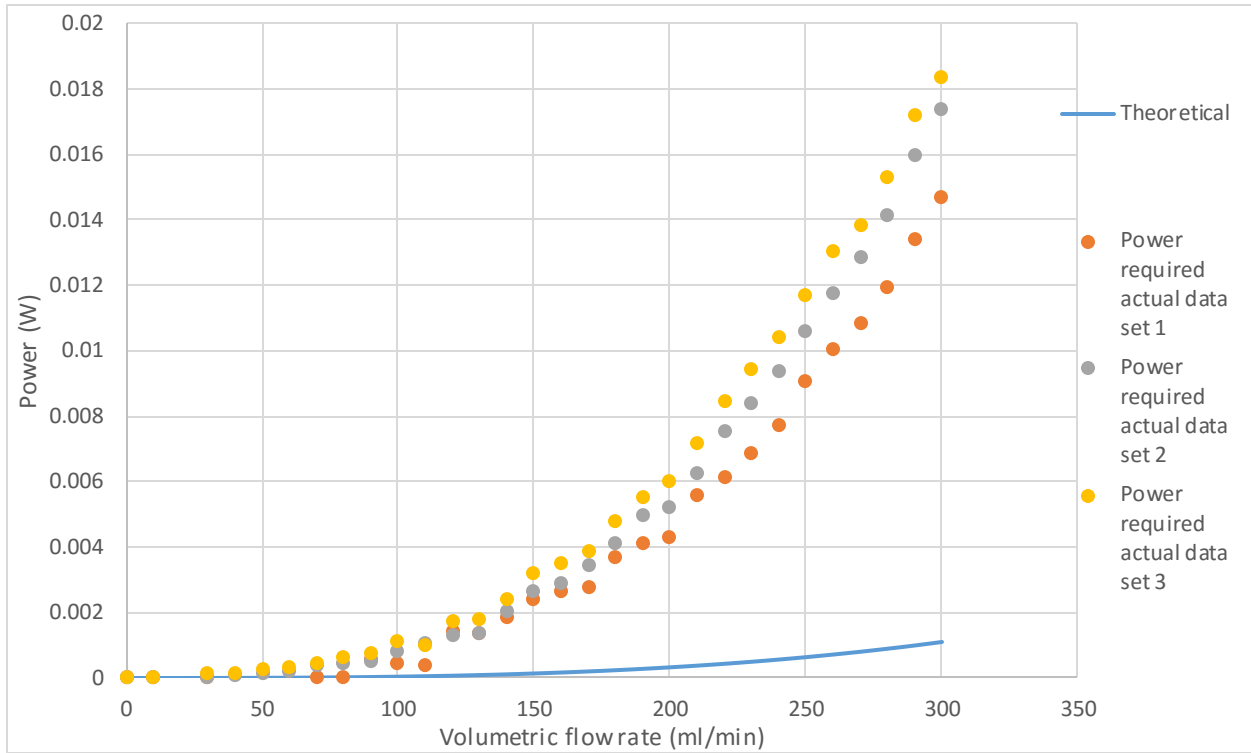


Figure 74: Contraction theoretical power required (W) using large area velocity, laminar $K_c=0.78$ assumption, $\Delta P_c = (0.5\rho V^2/g_c)[(1-\sigma^2)+K_c]$, and $\delta E/\delta t = \text{Volumetric flow rate} * \Delta P$ vs volumetric flow rate plotted with experimental data.

Again in Figure 74, it is quite clear from the data that the assumption of laminar flow coupled with the lower velocity before the contraction does not provide a reasonable prediction, even though it is slightly better than assuming low velocity and turbulent conditions.

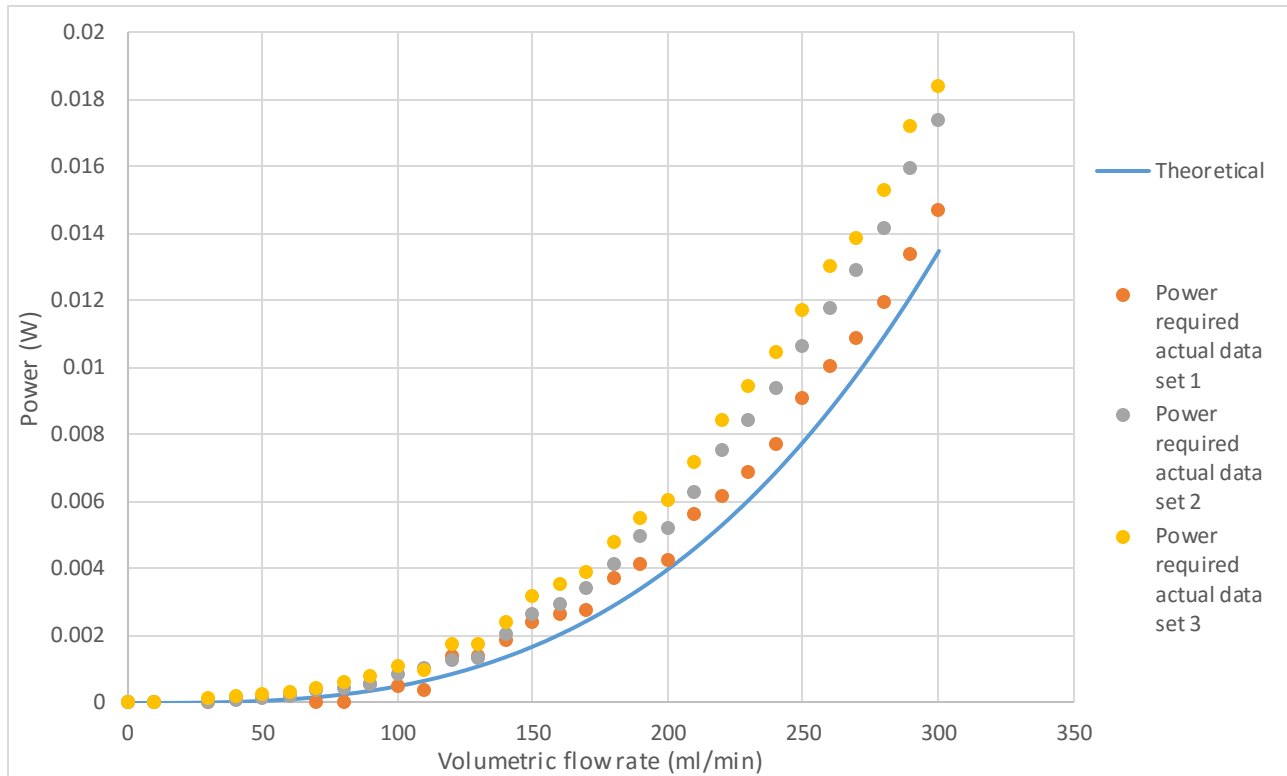


Figure 75: Contraction theoretical power required (W) using small area velocity, turbulent $K_c=0.4$ assumption, $\Delta P_c = (0.5\rho V^2/g_c)[(1-\sigma^2)+K_c]$, and $\delta E/\delta t = \text{Volumetric flow rate} * \Delta P$ vs volumetric flow rate plotted with experimental data.

Using the velocity in the smaller section creates a large increase in the predictability of the power needed as shown in Figure 75. Using a turbulent model still under predicts the power needed, but is a much better representation of the data obtained experimentally.

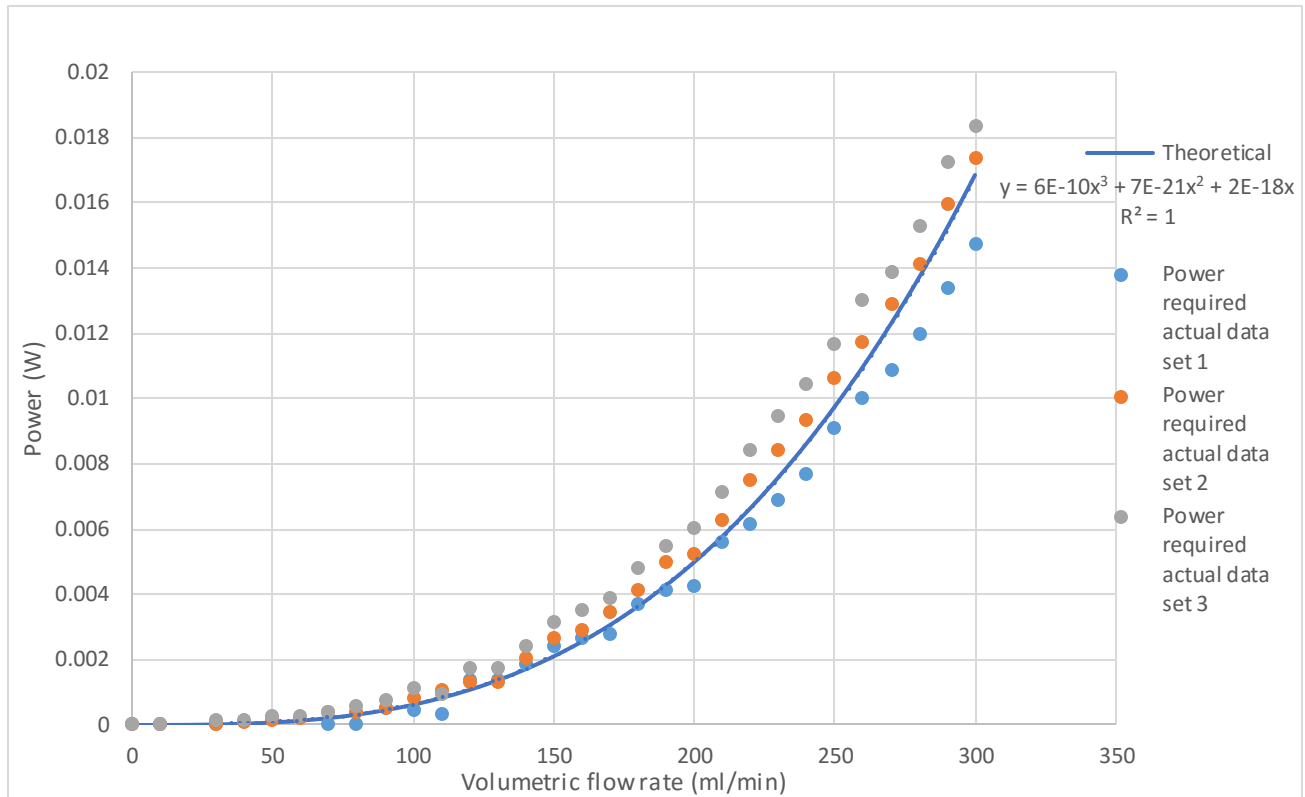


Figure 76: Contraction theoretical power required (W) using small area velocity, laminar $K_c=0.78$ assumption, $\Delta P_c = (0.5\rho V^2/g_c)[(1-\sigma^2)+K_c]$, and $\delta E/\delta t = \text{Volumetric flow rate} \cdot \Delta P$ vs volumetric flow rate plotted with experimental data.

4.18 Modeling Conclusions

Using the relatively large velocity in the contracted portion of the channel and the laminar K_c clearly provides the best prediction of power needed to move the fluid at all volumetric flowrates. This is true for the experimental data in the experiment because the pump is limited to a maximum of 300 ml/min. If a pump was brought in with a higher pumping capacity, the correlation would probably be better predicted with the turbulent coefficient assumption. In order to ensure a fully turbulent environment, a maximum velocity of 5.7 m/s would need to be achieved or a pumping rate of 861 ml/min. It should be noted this would require a pump with a

remarkably high pumping force in order to create such a large velocity in a short and narrow channel.

4.19 Total Volume Moved with 1000 Joules

The total amount of volume moved with a set amount of energy can be easily modeled for the contraction test as well. The results of the contraction test are similar to the expansion test, but there is less fluid moved at the same flowrate. This is due to the higher amount of power input needed to move the fluid at a set volumetric flow rate. This is quite evident when comparing the results of the contraction and expansion flow. The results can be seen in Figure 77. Notice how the Liters of water moved can be modeled with a negative 2 power function. The amount of Liters pumped severely drops off around a flowrate of 50 ml/min.

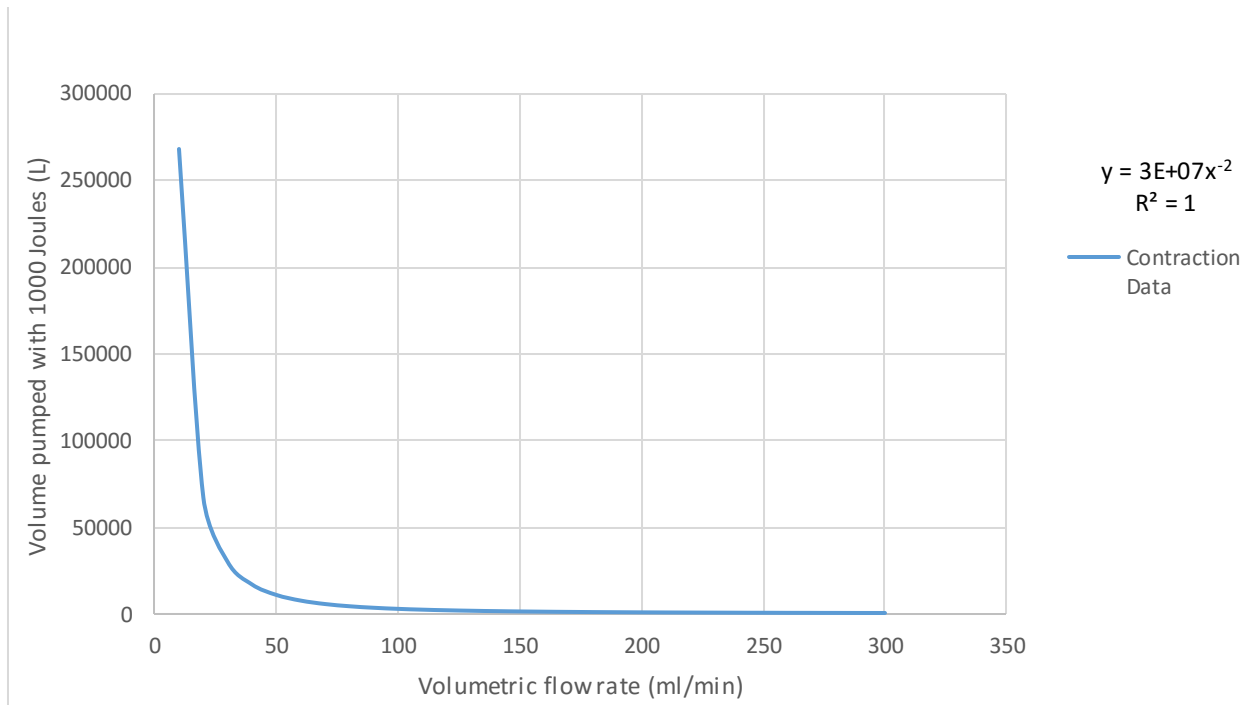


Figure 77: Liters pumped with 1000 Joules through the contraction channel using: Energy = P*t, $\Delta P_c = (0.5\rho V^2/g_c)[(1-\sigma^2)+K_c]$, and $\delta E/\delta t = \text{Volumetric flow rate} * \Delta P$ vs volumetric flow rate (ml/min).

4.20 Summary of Expansion and Contraction Testing

When looking at the overall outcome of the pressure and power results for porous media, expansion, and contraction channels, several key realizations can be made. The first key point is flowing through the contraction orientation requires 3 times more power than the expansion at 300 ml/min. This is critical to understanding how to create an efficient design in industry for miniature channel applications. The flow through the porous test section needed 2.8 times more power than the contraction channel and 8.5 times more power than the expansion test section at 300 ml/min. It is also important to note the porous test section was 4 times shorter than the expansion and contraction test sections. To flow through an equivalent length of porous material would have needed much more power and energy. It is also important to note the comparison between the porous material and the expansion and contraction test section orientations is not completely valid because they are made from different materials. The expansion and contraction test section is made from 6061 aluminum as stated in the experimental setup chapter, and the porous material is made of aluminum dioxide, which is a much rougher, course surface. The comparison between the expansion and contraction is extremely valid, because the only variable in the experiment was the direction of flow.

4.21 Hydrodynamic Development

Another topic closely pertaining to the expansion and contraction miniature channel flow is the hydrodynamic development. When the flow is coming in from the reservoir and first touches the channel, there is a uniform velocity throughout the flow. As the viscous friction begins to the flow at the walls, the middle of the flow is beginning to move faster. Once the flow is hydrodynamically developed, the zero wall velocity assumption can be made (Bergman et al.,

2011). The flow velocity will also take on a parabolic form. Until the flow is fully developed, there will be a transient velocity pattern. This is illustrated in Figure 78 below.

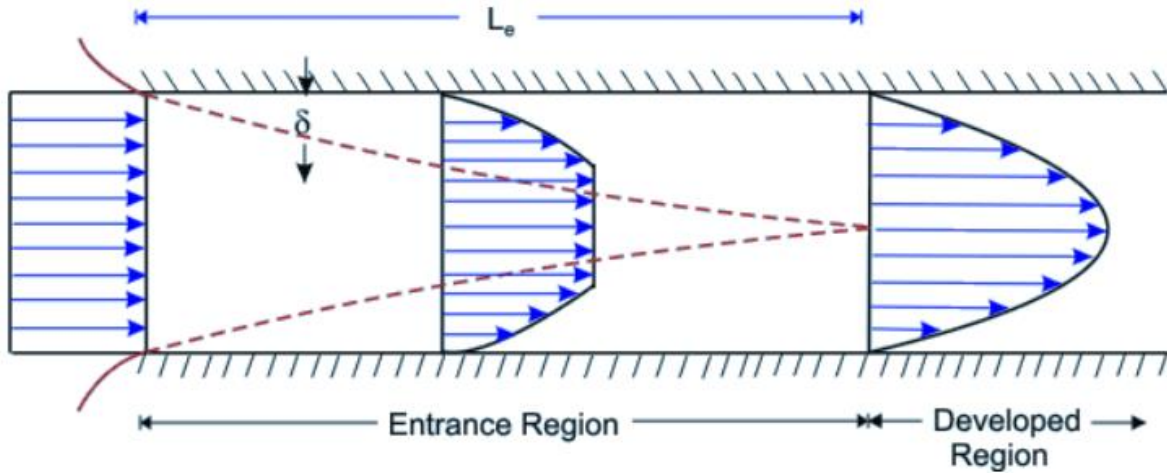


Figure 78: Hydrodynamic development of flow through a channel (Bergman et al., 2011)

To determine if the flow is hydro-dynamically developed when the flow is not fully turbulent, but the onset of turbulence has begun, Equation 4.21.1 below allows the calculation to be made.

It is a function of hydraulic diameter and Reynolds number (Bergman et al., 2011):

$$X_{fd,h} = 0.05 * D * Re_d, \quad (4.21.1)$$

Using the hydraulic diameter and traditional Reynolds number for the wide and narrow sections of the expansion and contraction test section, the flow will become fully developed in the narrow section at the exit when the Reynolds number is below 400. The flow will become fully developed at the exit of the wide channel when the Reynolds number is below 450. It should be mentioned this is an assumption based on traditional flow channels and does not take into effect the separation that takes place around the abrupt change in cross sectional area. To ensure that

the flow is fully developed at both the small and large cross sectional areas, a Reynolds number of 400 or less should be used.

CHAPTER 5

CONCLUSION AND RECOMMENDATIONS

5.1 Conclusion

Upon conclusion of the research thesis, several conclusions can be made. The first and most obvious conclusion is the power and energy needed to flow through the titanium dioxide porous material is much greater than the square channel expansion and contraction test sample. The porous media required 8.5 times more power than the expansion test section and 2.8 times more power than the contraction test section. This is due mainly to the cross-sectional area of the flow area in the porous material being much smaller than the expansion and contraction sample due to the insert in the channel. The more flow-intrusive porous material shape causes form drag, especially with increasing velocity. There is also much more drag in the porous material channel due to the increased surface area to volume ratio. The viscous drag effects of the increased surface area on the fluid also increase the total drag at all velocities, causing increased power and energy needed to move the liquid through the channel. A second conclusion drawn from analysis of the data indicates minimization of volumetric flow rate is essential to reducing power and energy needed to move a fluid through the channel. When using miniature channel heat exchangers, the amount of heat transferred is maximized at relatively high flowrates. When designing heat exchangers with a limited amount of pumping power and energy available; such as many space-related applications, a balance between increased velocity with increased heat

transfer and energy saving slower velocity flow must be achieved. The porous material made of titanium dioxide was found to have a permeability coefficient of $5.28 \times 10^{-9} \text{ m}^2$ and a form coefficient of 236 m^{-1} . These can be used to model the flow at volumetric flow rates under 300 ml/min and predict the amount of form and viscous drag provided with Equation 4.5.2 and Figure 58. The final simplified equation to accurately determine differential pressure in the titanium dioxide porous material using standard metric units is Equation 5.1.1.

$$\Delta P_{\text{porous}} = (L/g_c) * [(1.9 * 10^8 \text{ m}^{-2}) * \mu * U + 236 \text{ m}^{-1} * \rho * U^2] \quad (5.1.1)$$

Analyzing the data from the expansion and contraction test runs reveals several key points. The flow through the expansion channel required much less power and total energy than the contraction channel. To model the flow through the expansion channel, Equation 4.9.1 yielded accurate predictions of differential pressure test data. Equation 5.1.2 is the simplified version of 4.9.1 and provided the most accurate results in predicting differential pressure for the 4 to 1 area expansion ratio channel tested.

$$\Delta P_e = (0.19/g_c) * \rho * U^2 \quad (5.1.2)$$

To model flow through the 4 to 1 area ratio contraction test section, 4.14.1 yielded accurate results and the final simplified equation can be seen below in Equation 5.1.3.

$$\Delta P_c = (0.86/g_c) * \rho * U^2 \quad (5.1.3)$$

The required energy to flow single phase liquid through the porous material, rapid expansion, and rapid contraction test sections can be seen in equations (5.1.4), (5.1.5), and (5.1.6) respectively along with required power in (5.1.7), (5.1.8), and (5.1.9).

$$E_{\text{porous}} = (L/g_c) * \Lambda * [(1.9 * 10^8 \text{ m}^{-2}) * \mu * U + 236 \text{ m}^{-1} * \rho * U^2] \quad (5.1.4)$$

$$E_e = \Lambda * (0.19/g_c) * \rho * U^2 \quad (5.1.5)$$

$$E_c = \Lambda * (0.86/g_c) * \rho * U^2 \quad (5.1.6)$$

$$\delta E / \delta t_{porous} = (L/g_c) * [961 * \mu * U^2 + 0.0012 m * \rho * U^3] \quad (5.1.7)$$

$$\delta E / \delta t_e = (4.9 * 10^{-7} m^2) * (\rho/g_c) * U^3 \quad (5.1.8)$$

$$\delta E / \delta t_c = (2.2 * 10^{-6} m^2) * (\rho/g_c) * U^3 \quad (5.1.9)$$

Flow was studied from completely laminar conditions to partially turbulent flow up to a Reynold's number of 3500. Traditional round channel flow without expansions or contractions dictates a laminar zone using Reynold's numbers ranging from 0-2300, partially turbulent from 2300-10000 and fully turbulent when above 10000. Since the experiment used a sudden contraction coupled with a square channel at multiple Reynold's number values, a determination was made based on empirical results as to which velocity to choose and whether the flow should be modeled as laminar or turbulent. As discussed in the results and discussion chapter, to provide the most accurate model of the contraction flow, a K_c using the relatively higher velocity in the contracted portion of the channel coupled with laminar flow assumptions from Figure 66 must be used. Using a turbulent assumption will slightly underestimate the differential pressure and the relatively slower velocity in the wide cross sectional area will drastically underestimate the differential pressure. It is also advised the results of the experiment be used for laminar applications and flow with Reynold's numbers below 3500. Due to limitations on volumetric pumping capacity, the results could not be tested at Reynold's numbers higher than 3500.

Previous literature suggests the flow can be accurately modeled as turbulent when a Reynold's

number reaches 4000 in traditional channels, which supports the empirical data and analysis showing laminar flow up to 3500 in this study for rapidly expanding and contracting channels. The total linear pushing power of the syringe pump is 1.25 Watts and since both withdrawal and infuse are simultaneous, the infuse side only has 0.625 Watts of maximum power. The flow through the porous material at the maximum flow rate of 300 ml/min yielded a needed power of 0.0475 Watts. Only 7.6% of the available power was used to move the fluid through the porous material. When running the pump, it occasionally stalled due to lack of power, showing that most of the available power was being utilized. This clearly indicates the system inefficiencies accounted for most of the power usage during testing. Experiments with less porous material or more viscous fluid would require modifications such as: a more powerful syringe pump, a system setup without inlet and outlet reservoirs which require additional pumping power, or removal of the convenient withdrawal syringes to reduce the pumping requirements.

5.2 Recommendations

One major component of the overall project was the development of a testing system capable of testing a wide variety of fluids in miniature channels for the University of North Dakota. As stated in the literature review chapter, nanofluids provide faster transfer of heat than traditional fluids by using nano-sized particles with a higher thermal conductivity than the bulk fluid. The nano-sized particles can cause traditional pumps and seals to fail because the extraordinarily small particles can get into cavities and bearings and cause friction and wear. The system designed with the syringe pump for the thesis is capable of testing nanofluids without excessive wear due to the nanofluid being contained away from moving parts susceptible to damage. This gives the University of North Dakota the ability for tremendous fluid testing selection flexibility. With this in mind, the research going forward should build upon the work done in this thesis with research comparing the Newtonian water data, results, and analysis with non-Newtonian nanofluids and colloids for noncircular microchannel flow through porous and nonporous abrupt expansions and contractions. Analysis of pumping power and energy requirements should be analyzed and compared with the theoretical additional heat transfer provided with using nanofluids. Once this comparison is made, an energy and power savings analysis versus using only water bulk fluid can be completed.

This project focused primarily on single-phase flow. Future research should also look into the effects of using an inert gas flowing with water to create a two-phase flow on noncircular miniature channel flow with porous and nonporous abrupt expansions and contractions. The water can also be substituted for a nanofluid and the same experiment can then be run again to compare and contrast both runs. The pumping power and energy required should be compared to each other and a correlation of pumping power increase versus void fraction can be obtained.

Using the previous recommended experiments, the permeability and form constants of porous media should be determined and see if they fluctuate based upon the fluid being run through it. If the constants do change, a correlation could then be calculated to test porous media with a two-phase fluid, non-Newtonian fluid, or two-phase non-Newtonian fluid, and convert the results back to the original results of single-phase, Newtonian flow constants.

Using the future experiments outlined above would allow one variable to be changed at a time and compared to the original data obtained in this thesis. Once the results of energy and power requirements, losses, and other valuable data is compiled, an experiment testing heat transfer for the previous work could then be completed. This would allow engineers designing porous media heat exchangers to be able to optimize the amount of heat transferred while minimizing the required energy and pumping power. These results could dramatically help designers of heat exchangers where pumping energy needs to be conserved. When designing space-related heat exchangers, using many small channels will provide a significantly higher surface area to volume ratio than a few large channels at an equivalent mass flow rate. This increase will be magnified further by using porous media inserts. When using a pump with a defined mass flow rate, using many small channels with porous media inserts will also conserve pumping energy. The individual channel mass flow rate will be smaller using lower velocity through many small channels than using a relatively high flow rate through a few small channels. Using many small channels decreases the fluid velocity and form drag as shown in Figure 58, therefore saving energy. When using a Newtonian fluid as a heat exchanging medium, many miniature channels with porous media inserts should be utilized to increase heat transfer and reduce the pumping energy required. The porous media used in the experimentation was not flexible. However, applications such as space suits would require a flexible porous media to allow astronauts to

have flexibility and mobility. Developing a flexible porous media would be necessary to utilize the advantages of porous media heat exchangers for this application. However, many other applications such as heat exchangers for a space station would be rigid, allowing relatively non-flexible porous media to be utilized. Hopefully the future experiments coupled with this thesis will bring further insight into the world of fluid flow.

REFERENCES

- Abouelwafa, M.S.A., Kendall, E.J.M., 1980, The use of capacitance sensors for phase percentage determination in multiphase pipelines *IEEE Trans. Instrum. Meas.*, 29 (1), pp. 24–27
- Agostini, B., Revellin, R., Thome, J.R., Fabbri, M. Michel, B., Calmi, D., Kloter, U., 2008. High heat flux flow boiling in silicon multi-microchannels – Part III: Saturated critical heat flux of R236fa and two-phase pressure drops *Int. J. Heat Mass Transfer*, 51, pp. 5426–5442
- Ahmed, W.H., Ismail, B.I., 2008. Innovative techniques for two-phase flow measurements *Recent Patents Elect. Eng.*, 1, pp. 1–13
- Ali, M., Sadatomi, M., Kawaji M., 1993. Adiabatic two-phase flow in narrow channels between two flat plates. *Can. J. Chem. Eng.*, 71, pp. 657–666
- Azzi, A., Al-Attiyah, A., Liu, Q., Cheema, W., Azzopardi, B.J., Whalley, P.B., Chung, P.M.-Y., Kawaji, M., Hsieh, S.S., Lin, C.Y., Huang, C.F., Tsai H.H., 2010. Gas-liquid two-phase flow division at a micro-T-junction. *Chem. Eng. Sci.*, 65, pp. 3986–3993
- Azzopardi, B.J., Whalley, P.B., 1982. The effect of flow patterns on two-phase flow in a T junction. *Int. J. Multiph. Flow*, 8, pp. 491–507
- Barbir, F., Gorgun, H., Wang, X., 2005. Relationship between pressure drop and cell resistance as a diagnostic tool for PEM fuel cells, *J. Power Sources*, 141 (2005), pp. 96–101
- Barr, W., D, 2001, *Turbulent Flow Through Porous Media, Ground Water*, Vol 39 pp. 646-650.
- Bergman, Adrienne, Incropera, Dewitt, 2011. *Fundamentals of Heat and Mass Transfer* 7th Edition, John Wiley & Sons, Inc. 111 River Street, Hoboken, NJ 07030-5774
- Brauner, N., and Maron, D. M., 1993. The Role of Interfacial Shear Modeling in Predicting the Stability of Stratified Two-Phase Flow, *Chemical Engineering Science*, vol. 48, pp. 2867–2879.
- Caniere, H., T’Joen, C., Willockx, A., De Paepe, M., Christians, M. van Rooyen, E., Liebenberg, L., Meyer, J.P., 2007. Horizontal two-phase flow characterization for small diameter tubes with a capacitance sensor. *Meas. Sci. Technol.*, 18, pp. 2898–2906
Caniere, H., T’Joen, C., Willockx, A., De Paepe, M., 2008. Capacitance signal analysis of horizontal two-phase flow in a small diameter tube. *Exp. Thermal Fluid Sci.*, 32, pp. 892–904

- Cha, S.W., O'Hayre, R., Prinz, F.B., 2004. The influence of size scale on the performance of fuel cells, *Solid State Ionics*, 175, pp. 789–795
- Chen, J., Wang, S., Ke, H., Cai, S., Zhao, Y., 2013. Chemical Gas–liquid two-phase flow splitting at microchannel junctions with different branch angles *Engineering Science*, 104, 881–890
- Choi, C.W., Yu, D.I., and Kim, M.H., Adiabatic two-phase flow in rectangular microchannels with different aspect ratios: Part I – Flow pattern, pressure drop and void fraction, *International Journal of Heat and Mass Flow*, 54, 1-3, 616–624
- Chung, P.M.-Y., Kawaji, M., 2004. The effect of channel diameter on adiabatic two-phase flow characteristics in microchannels. *Int. J. Multiph. Flow*, 30 (2004), pp. 735–761
- Coleman, J.W., Garimella, S., 1999. Characterization of two-phase flow patterns in small diameter round and rectangular tubes. *Int. J. Heat Mass Trans.*, 42, pp. 2869–2881
- Cubaud, T., Ulmanella, U., Ho, C.M., 2006. Two-phase flow in microchannels with surface modifications. *Fluid. Dyn. Res.*, 38, pp. 772–786
- Gupta, S. and Riyad, M., 2014. Oxidation-Induced Sintering: An innovative Method for Manufacturing Porous Ceramics, *Applied Ceramics Volume 11*, Issue 5 September/October 2014 Pages 817–823
- Harvel, G.D., Hori, K., Kawanishi, K., Chang, J.S., 1996. Real-time cross-sectional averaged void fraction measurements in vertical annulus gas–liquid two-phase flow by neutron radiography and X-ray tomography techniques *Nucl. Instrum. Methods Phys. Res. A*, 371, pp. 544–552
- Haverkamp, V., Hessel, V., Lowe, H., Menges, G., Warnier, M.J.F., Rebrov, E.V., de Croon, M.H.J.M., Schouten, J.C., Liauw, M.A., 2006. Hydrodynamics and mixer-induced bubble formation in micro bubble columns with single and multiple-channels *Chem. Eng. Technol.*, 29, pp. 1015–1026
- Hsieh, S.S., Lin, C.Y., Huang, C.F., Tsai H.H., 2004. Liquid flow in a micro-channel. *J. Micromech. Microeng.*, 14, pp. 436–445
- Huang, S.M., Green, R.G., Płaskowski, A.B., Beck, M.S., 1988a. Conductivity effects on capacitance measurements of two-component fluids using the charge transfer method. *J. Phys. E: Sci. Instrum.*, 21, pp. 539–548
- Huang, S.M., Fielden, J., Green, R.G., Beck M.S., 1988b. A new capacitance transducer for industrial applications *J. Phys. E: Sci. Instrum.*, 21, pp. 251–256

- Huang, S.M., Stott, A.L., Green, R.G., Beck, M.S., 1988c. Electronic transducers for industrial measurement of low value capacitances *J. Phys. E: Sci. Instrum.*, 21, pp. 242–250
- Jaworek, A., Krupa, A., 2004. Gas/liquid ratio measurements by RF capacitance sensor *Sens Actuators A: Phys.*, 113 (2), pp. 133–139
- Jaworek A., Krupa A., Phase-shift detection for capacitance sensor measuring void fraction in two-phase flow, *Sensors and Actuators*, 160, 1-2, 78-86
- Jaworek, A., Krupa, A., Trela M., 2004. Capacitance sensor for void-fraction measurement in water/steam flows. *Flow Meas. Instrum.*, 15 (5/6), pp. 317–324
- Jaworski, A.J., Dyakowski, T. Davies, G.A., 1999. A capacitance probe for interface detection in oil and gas extraction plant *Meas. Sci. Technol.*, 10 (3), pp. L15–L20
- Kandlikar, S.G., 2002. Fundamental issues related to flow boiling in minichannels and microchannels. *Exp. Thermal Fluid Sci.*, 26 (2002), pp. 389–407
- Kang, H. C., Kim, M. H., 1993. The Relation Between the Interfacial Shear Stress and The Wave Motion in a Stratified Flow, *International Journal of Multiphase Flow*, vol. 19, pp. 35–49.
- Kawahara, A., Chung, P.M.Y., Kawaji, M., 2002. Investigation of two-phase flow pattern, void fraction and pressure drop in a microchannel. *Int. J. Multiphase Flow*, 28, pp. 1411–1435.
- Kawahara, A., Sasatomi, M., Nei, K., Matsuo H., 2009. Experimental study on bubble velocity, void fraction and pressure drop for gas–liquid two-phase flow in a circular microchannel. *Int. J. Heat Fluid Flow*, 30, pp. 831–841
- Kawaji, M., 2008. Unique Characteristics of Adiabatic Gas-Liquid Flows in Microchannels: Diameter and Shape Effects on Flow Patterns, Void Fraction and Pressure Drop, in: *Proceedings of the International Conference on Heat Transfer and Fluid Flow in Microscale*, Whistler, Canada.
- Keska, J.K., Williams B.E., 1999. Experimental comparison of flow pattern detection techniques for air–water mixture flow *Exp. Thermal Fluid Sci.*, 19, pp. 1–12
- Kline, S. J., and McClintock, F. A., 1953, Describing uncertainties in single-sample experiments. *Mechanical Engineering*, 75, pp. 3–8.

- Li, X., Sabir, I., Park, J., 2007 A flow channel design procedure for PEM fuel cells with effective water removal. *J. Power Sources*, 163, pp. 933–942
- Lim, F., Y., Abdullah, S., Ahmad, I., 2010. Numerical Study of Fluid Flow and Heat Transfer in Microchannel Heat Sinks using Anisotropic Porous Media Approximation, *Journal of Applied Sciences*, 10 (18): pp. 2047-2057
- Lockhart, R.W., Martinelli, R.C., 1949. Proposed correlation of data for isothermal two-phase, two-component flow in pipes *Chem. Eng. Prog.*, 45, pp. 39–48
- Mangalgi, P. D., 1999. Composite materials for aerospace applications, *Bulletin of Materials Science*, 22(3) 657-664.
- Mishima, K., Hibiki, T., Nishihara, H., 1993. Some characteristics of gas–liquid flow in narrow rectangular ducts. *Int. J. Multiphase Flow*, 19, pp. 115–124
- Moffat, R. J. 1988. Describing the uncertainties in experimental results. *Experimental Thermal and Fluid Science*, 1, pp. 3–17.
- Moriyama, K., Inoue, A. and Ohira, H. 1992. Thermohydraulic Characteristics of Two-Phase Flow in Extremely Narrow Channels (The Frictional Pressure Drop and Heat Transfer of Boiling Two-Phase Flow, Analytical Model). *Heat Transfer Japanese Research*, vol. 21(8): 838–856.
- Narasimhan, A., 2013. *Essentials of Heat and Fluid Flow in Porous Media*, CRC Press Taylor & Francis Group.
- Nguyen, T.V., Knobbe, M.W., 2003. A liquid water management strategy for PEM fuel cell stacks. *J. Power Sources*, 114, pp. 70–79
- Pastore, R., Giannini, G., Morles, R.B., Marchetti, M., Micheli, D., 2012. Impact Response of Nanofluid-Reinforced Antiballistic Kevlar Fabrics, Nanocomposites, *New Trends and Developments.*”.
- Squires, T.M., Quake, S.R., 2005. Microfluidics: fluid physics at the nanoliter scale. *Rev. Mod. Phys.*, 77, pp. 977–1026
- Serizawa, A., Feng, Z., Kawara, Z., 2002. Two-phase flow in microchannels. *Exp. Thermal Fluid Sci.*, 26, pp. 703–714
- Steinbrenner, J. E., Lee, E. S., Hidrovo, C. H., Eaton, J. K., Goodson, K. E., Impact of channel geometry on two-phase flow in fuel cell microchannels, *Journal of Power Sources*, 196, 5012-5020
- Stott, A.L., Green, R.G., Seraji K., 1985. Comparison of the use of internal and external electrodes for the measurement of the capacitance and conductance of fluids in pipes *J. Phys. E: Sci. Instrum.*, 18, pp. 587–592

- Taitel, Y., and Dukler, A., 1976. A Theoretical Approach to the Lockhart-Martinelli Correlation for Stratified Flow, *International Journal of Multiphase Flow*, vol. 2, pp. 591–595.
- Tollefsen, J., Hammer, E.A., 1998. Capacitance sensor design for reducing errors in phase concentration measurements. *Flow Meas. Instrum.*, 9 (1), pp. 25–32
- Triplett, K.A., Ghiaasiaan, S.M., Abdel-Khalik, S.I., Sadowski, D.L., 1999. Gas–liquid two-phase flow in microchannels Part I: two-phase flow patterns. *Int. J. Multiphase Flow*, 25, pp. 377–394
- Valinčius, M., Šeporaitis, Ušpuras, M.,E., Kaliačka, A., 2011. Experimental Investigation and RELAP5 Modeling of Two-Phase Flow in Horizontal Rectangular Channel. *Heat Transfer Engineering*, 32, 11-12, 1126-1130
- Wang, J., Li, F., Gardner, R.P., 2008. On the use of prompt gamma-ray neutron activation analysis for determining phase amounts in multiphase flow *Meas. Sci. Technol.*, 19, p. 6 094005
- Wong, H., Radke, C.J., Morris, S., 1995. The motion of long bubbles in polygonal capillaries. Part 2: Drag, fluid pressure and fluid flow *J. Fluid Mech.*, 292, pp. 95–110.
- Xuan, Y., LiHigdon, Q., 2000. Heat transfer enhancement of nanofluids, *International Journal of Heat and Fluid Flow*, 21, 58-64.
- Zhao, Y., Chen, G., Ye, C., Yuan, Q., 2013. Gas-liquid two-phase flow in microchannel at elevated pressure, *Chemical Engineering Science*, 87, 122-132